AD A157 163 TRANSONIC NOISE GENERATION BY DUCT AND PROFILE FLOW(U) 1/2
MAX-PLANCK-INST FUER STROEMUNGSFORSCHUNG GOETTINGEN
(GERMANY F R) G E MEIER OCT 84 DAJA37-81-C-0251

UNCLASSIFIED F/G 20/1 NL

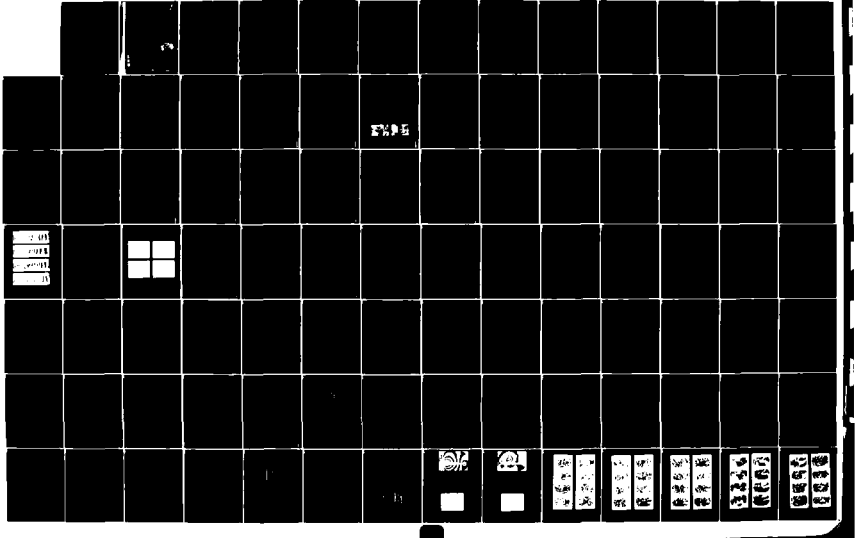

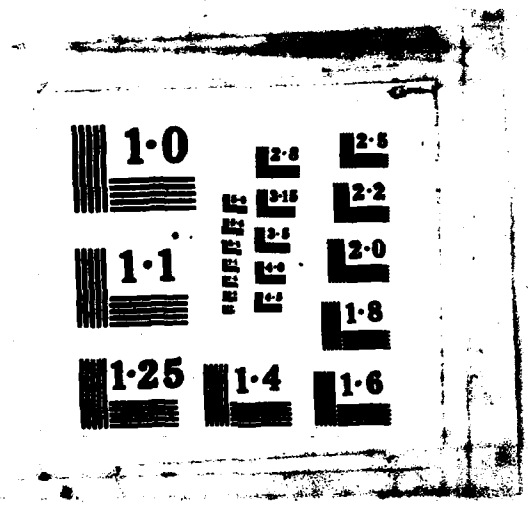
1·0
1·1
1·25
1·4
1·6
2·0
2·2
2·5

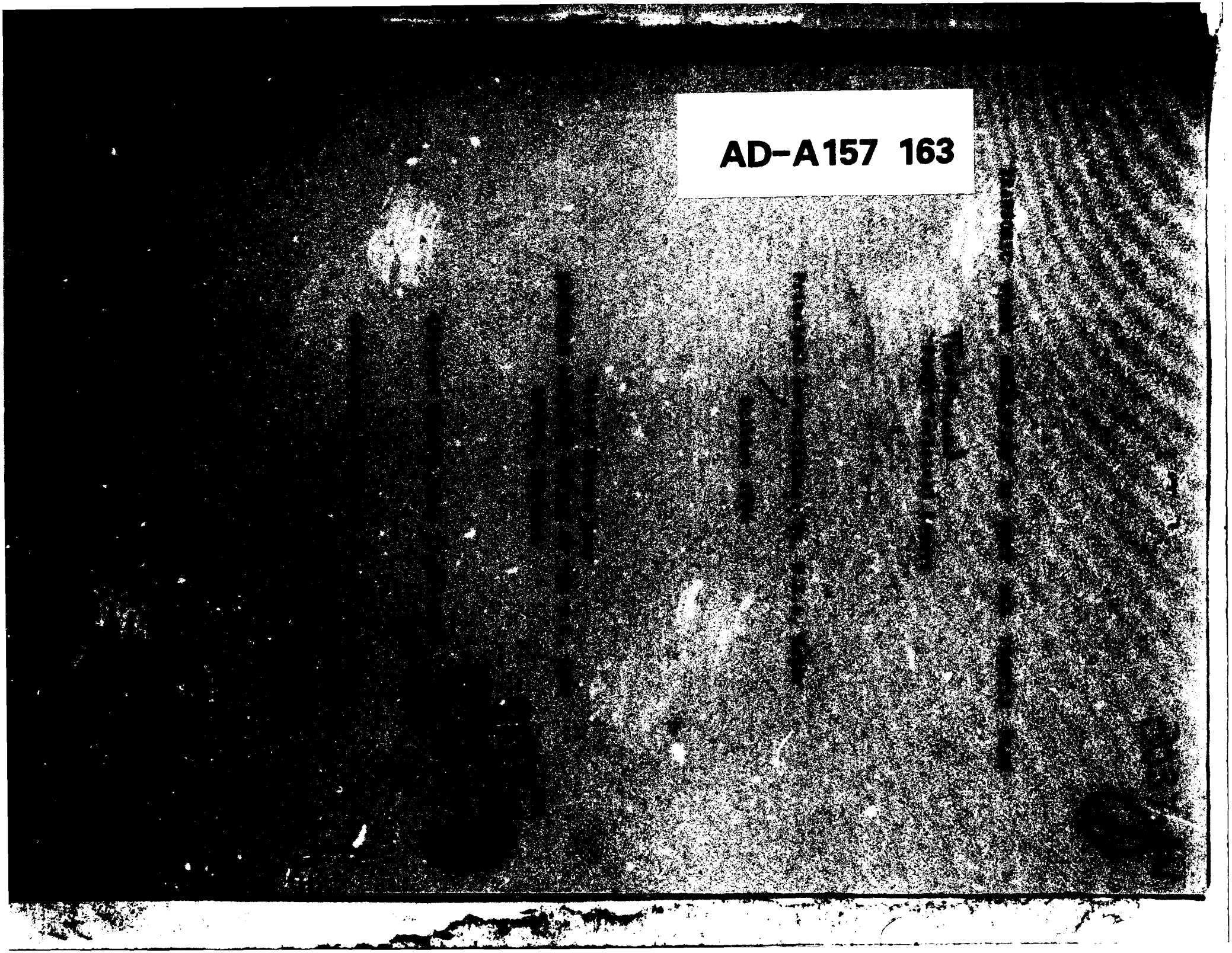
AD-A157 163

UNCLASSIFIED
SECURITY CLASSIFICATION OF THIS PAGE (When Data Entered)

R&D 3037-AN

REPORT DOCUMENTATION PAGE	READ INSTRUCTIONS BEFORE COMPLETING FORM
1. REPORT NUMBER	2. GOVT ACCESSION NO. AD-A157163	3. RECIPIENT'S CATALOG NUMBER
4. TITLE (and Subtitle) Transonic Noise Generation by Duct and Profile Flow	5. TYPE OF REPORT & PERIOD COVERED
	6. PERFORMING ORG. REPORT NUMBER
7. AUTHOR(s) Dr. G.E.A. Meier; Dipl. Phys. R. Timm; Dr. F. Becker	8. CONTRACT OR GRANT NUMBER(s) DAJA 37-81-C-0251
9. PERFORMING ORGANIZATION NAME AND ADDRESS MPI für Strömungsforschung D-3400 Göttingen Böttingerstr. 4-8	10. PROGRAM ELEMENT, PROJECT, TASK AREA & WORK UNIT NUMBERS 6.11.02A 1T16 1102BH57-06
11. CONTROLLING OFFICE NAME AND ADDRESS USARDSG-UK Box 65, FPO New York 09510	12. REPORT DATE
	13. NUMBER OF PAGES
14. MONITORING AGENCY NAME & ADDRESS(if different from Controlling Office)	15. SECURITY CLASS. (of this report) Unclassified
	15a. DECLASSIFICATION/DOWNGRADING SCHEDULE

16. DISTRIBUTION STATEMENT (of this Report)

Approved for public release; distribution unlimited

17. DISTRIBUTION STATEMENT (of the abstract entered in Block 20, if different from Report)

18. SUPPLEMENTARY NOTES

19. KEY WORDS (Continue on reverse side if necessary and identify by block number)

Laval nozzle, transonic noise generation, shockwave instability; flow separation; boundary layer; shear layer; acoustic resonance; profile-vortex interaction; secondary vortex, vortex noise; digital interferogram analysis, (West Germany)

20. ABSTRACT (Continue on reverse side if necessary and identify by block number)

Part A: Acoustic distortions which are generated by a downstream instability of shear layers are travelling upstream in the subsonic part of the laval nozzle flow and are acting on the shock wave at the end of the supersonic part. This interaction causes strong oscillations.

Part B: Different kinds of separation and secondary vortex generation have a governing influence on profile-vortex interaction flow. Keywords: Laval nozzle; Transonic noise generation; Shock wave

DD FORM 1 JAN 73 1473 EDITION OF 1 NOV 65 IS OBSOLETE

UNCLASSIFIED
SECURITY CLASSIFICATION OF THIS PAGE (When Data Entered)

Summary Part A: Unsteady Flow in a Laval Nozzle

The type of instability which was especially investigated in the frame of this work, is strongest, if the flow is not separated in the downstream part of the duct, and acoustic distoritions which are generated by a downstream instability of shear layers, supported by acoustic resonance of cavities, are travelling upstream in the subsonic part of the Laval nozzle flow and are acting on the shock wave at the end of the supersonic part of the flowfield. In special situations, which we have called the transonic case, the interaction of these distortions and the shock waves can be comparatively strong as in the case of the strong oscillations. Then the shock wave can also leave the nozzle flow through the smallest cross section into the subsonic intake flow. For higher supersonic Mach numbers in the nozzle this means smaller pressure ratios, the acoustic distortions result only in small amplitude shock oscillations. For the case of flow separation we have observed a large damping for the upstream travelling distortions and consequently very small amplitudes of oscillations.

List of Keywords

Laval nozzle
Transonic noise generation
Shock wave instability
Flow seperation
Bloundary layer
Shear layer
Acoustic resonance

Summary Part B: Profile - Vortex Interaction

We have now experimental evidence that the interaction of vortices and profiles induces separation and secondary vortices. These effects are not included in the present theoretical models. The theoretical treatment of the problem of sound generation by vortices requires an exact knowledge of the vortex induced flow. Therefore we have performed the following research program.

The investigation of profile-vortex interaction consists of two parts. The first part is a Karman vortex street experiment. A NACA 0012 profile is placed in the wake of a spuare cylinder. This experiment gives an overview on the interaction of vortex an profile. Different types of interaction occur depending on the cord-length and position of the profile relative to the cylinder. Strong vortices cause mainly strong secondary vortices on the profile while smaller vortices cause local separations. In each case the approaching vortex itself looses a lot of its strength or even nearly vanishes in strong interactions.

The second part of the investigation is a shock tube experiment. The uniform velocity downstream of a shock produces a starting vortex past an asymmetric profile. The starting vortex has a very small core because of the thin boundary layer. The low turbulence level and the potential character of the vortex allow quantitative comparisons with theroretical results.

List of Keywords

Profile-vortex interaction
Flow separation
Secondary vortex
Vortex noise
Digital interferogram analysis

Table of Contents

1. Introduction

1.1. General remarks on the contract

In the frame of this contract with the title

TRANSONIC NOISE GENERATION BY DUCT AND PROFILE FLOW

it was originally planned to investigate the unsteady transonic flow in Laval nozzles, in curved ducts and on profile sections. In accordance with the contracting officer and following the advise of some reviewers we have changed the program in the following way: In the first we have performed some research work on the unsteady transonic flow in a Laval nozzle and in the second and third year we have investigated the noise generation by vortex profile flow interaction. This latter program includes as well the interaction of single vortices with the transonic profile flow as the interaction of vortex streets or turbulence with the profile flow. - The planned investigation of the unsteady flow in a curved duct and the unsteady transonic flow around the profile (buffeting) was cancelled from the program.

In this final report we will describe in the part A the results of the investigation of the unsteady behaviour of the Laval nozzle flow. In part B of this report we will describe the results for the vortex profile flow interaction.

1,2 The work of the first year

If a Laval nozzle is used with a pressure ratio p_e/p_o (receiver pressure/ supply pressure) which is smaller than the designed pressure ratio a shock wave moves from downstream in the supersonic part of the nozzle flow and performs the transition from supersonic to subsonic flow velocities. As there are no real flows without small pressure fluctuations the positions of these shock waves are not stable. This was observed already early in this century for steam Laval nozzles (Stodola).

In earlier investigations [1] we have found self-excited oscillations of a Laval nozzle flow with a shock wave very close to the smallest cross section of the nozzle. In these investigations we have observed that the shock wave during one period of oscillation is propagated through the smallest cross section of the nozzle (sonic line) and propagated as a shock or bang wave in the subsonic intake flow. In the phase of reacceleration of the whole nozzle flow a new shock wave is formed under tnese conditions in the downstream expanding part of the nozzle.

For the explanation of this mechanism the existence of an extended dead air downstream of the supersonic part of the flowfield is of great importance. This flow separation can cause a nearly constant pressure flow downstream of the shock wave which in fact makes the exit pressure act on the shock wave and pushes the shock wave upstream if the separation point is connected with the shock root. This situation is leading to a further acceleration of the shock wave if it has passed the position of the highest shock back pressure. So at least the shock wave can be removed completely from the supersonic flow field. In the following acceleration phase of the whole nozzle flow the point of separation is travelling downstream and a new supersonic flow area with a new shock wave is formed. When the shock is sufficiently strong the point of separation is once again displaced to the shock root and the foregoing part of the cycle is repeated [1].

Because of the idea that the above mentioned cycle of oscillation is supported by an acoustic resonance of the downstream part of a duct (receiver) the aim of the present work was to investigate the influence of a changed geometry on the stability of the Laval nozzle flow and to investigate the influence of pressure disturbances generated downstream on the position of the shock wave. It became evident that by the changed geometry of the duct configuration (half profile for the nozzle and larger mixing chamber) also different oscillations occurred. The main frequency was about 500 Hz in the whole Mach number regime ($0.5 \leq Ma \leq 1.5$). Because of the fact that these distortions were coming upstream from the mixing chamber it became obvious that these distortions were generated by the shear layer of the nozzle outflow and amplified by a resonance of the chamber. With the occurance of the flow separation for larger angles of the variable nozzle the strength of the distortions or fluctuations decreased.

Also for two half nozzles with analytic shape (hyperbolic) the strong self-excited oscillations of the former tests with a symmetric nozzle could not be observed. From these additional tests we draw the conclusion that the self-excited oscillations can be prevented if the flow inside the nozzle is not separated in the low transonic Mach numbers and if the natural frequency of the duct system is not very close to the natural frequency of the relaxation oscillations of the transonic flowfield itself.

A large part of the pressure fluctuations in the average Laval nozzle flow is coming from downstream sources of pressure fluctuations and is amplified and concentrated in the transonic nozzle flow. So the first part of this report is concerned with the influence and the propagation of the downstream generated pressure fluctuations. Especially the interaction of the pressure fluctuations with the steady transonic shock waves at the end of the supersonic part of the nozzle flow is observed. In some cases the pressure fluctuations from downstream can be so strong that the shock wave at the

end of the supersonic flow regime is pushed out completely from the expanding part of the nozzle and is leaving the nozzle through the intake becoming at least a bang wave outside of the duct. This behaviour at least is then similar to one period of the self-excited oscillations which we have observed in former experiments for the two-dimensional Laval nozzles.

For the first tests we used as mentioned before a half Laval nozzle with a variable angle of expansion. But this supersonic nozzle flow was in the regime of the smallest cross section too much distorted from wall imperfections due to the mechanism of the flap. So for the important experiments we used mainly two different nozzles with hyperbolic shape which were carefully machined from a single piece of aluminium. The shape of the contour was got from the formula

$$F = F_o \sqrt{1 + x^2/a^2}$$

where a =93mm and F_o = 25 mm. The smallest section has a height F_o = 25 mm. For the narrow nozzle the area ratio between F_o and the height of the end section F_e was $XE = F_e/F_o = 1.3$ and for the wide nozzle we used $XE = 1.38$.

2. Experimental facility and test procedure for the Laval nozzle experiments

2.1 The transonic windtunnel

Figure 1 shows a sketch of the experimental arrangement for the Laval nozzle tests. Atmospheric air is passing through the nozzle into the mixing chamber which is connected to a vacuum reservoir by means of a regulating valve. The mixing chamber has an average constant pressure p_e by means of the sonic outflow from the regulating valve.

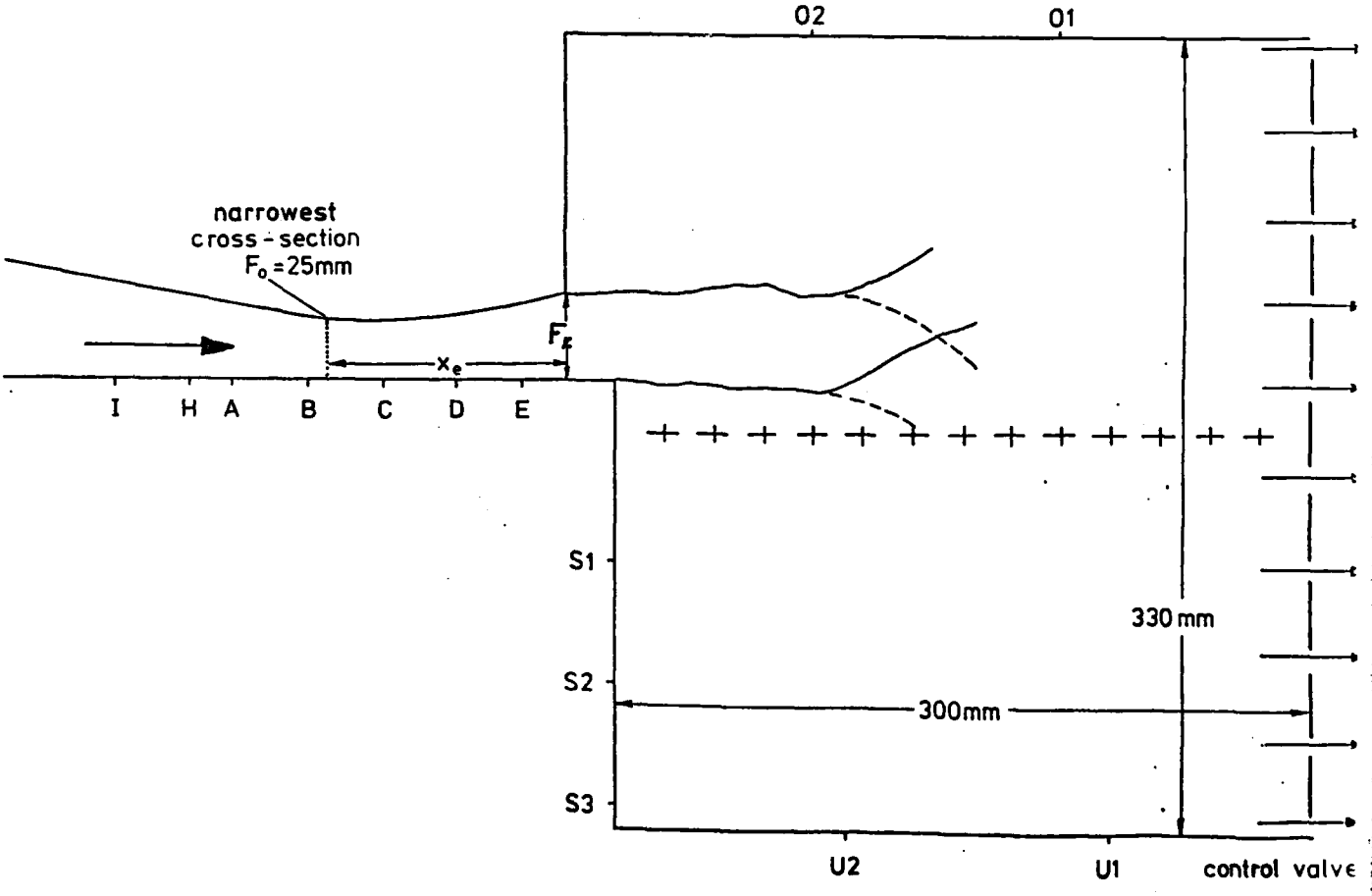

Figure 1: Sketch of the experimental setup for the transonic Laval nozzle experiments. On the left Laval nozzle, right mixing chamber. The position of the pressure transducers is indicated with letters.

Because of the sonic velocity in the regulating valve, pressure fluctuations inside the vacuum system are not changing the average pressure in the mixing chamber. With constant supply pressure p_o and sonic velocity in the smallest cross section of the regulating valve the pressure in the mixing chamber is determined by the area ratio of the Laval nozzle throat area F_o and the regulating valve area F_r

$$p_e = p_o F_r / F_o \tag{1}$$

For the case of subsonic flow in the regulating device the pressure p_e in the mixing chamber depends from the valve cross section F_r and the valve flow rate Q_r

$$Q_r/F_r = (p_e/p_o)^{1/k} \sqrt{p_o \varrho_o (1 - p_e/p_o)^{k-1/k} \; 2k/k - 1} \tag{2}$$

where ϱ_o is the density of the atmospheric air and k is the ratio of specific heat.

2.2 Pressure and density measurement in the nozzle flow

The density measurement and the flow visualization was performed by means of the Mach Zehnder interferometer. For that part of the flowfield which is covered by the two windows on both sides of the Laval nozzle we could take interferograms of the density field. The interference fringes in the photographs are lines of constant density. The density for the fringe with the number m is given by the following equation:

$$\varrho / \varrho_o = 1 - (n_o - 1)^{-1} \, m \cdot \lambda / b \tag{3}$$

where b is the lateral dimension of the duct and n_o is the index of refraction for the atmospheric air. By this equation the difference between the center of a white and a black line of the interferogram turns out to be

$$\Delta \varrho/\varrho_o = 0.02 \qquad \Delta p/p_o = 0.013$$

For the measurement of pressure piezo resistive and piezo electric transducers were used. They were flush mounted in the middle of the plane duct contour.

The pressure signals were conditioned to a voltage/pressure ratio of 10 V/bar. The signals were immediately digitized in an ADC of the PDP - 11 computer. After digitizing they are stored on a disk drive. The maximum digitizing frequency was f = 50 kHz. With the help of some special programs it was possible to show the pressure time signals of all transducers and the Fourier spectra of the signals on a PDP-11 terminal. By the multiplexing of the ADC the maximum recorded frequency depends not only on the sample theorem but also on the number s of the transducers:

$$f_{max} = 50 \text{ kHz}/2s \tag{4}$$

Because of the 1024 points of the screen of the terminal we have a time window for the plots:

$$t_F = 1024 s/50 \text{ kHz} \tag{5}$$

As an example for the mainly used hard copies of the plots on the screen we show the traces of a subsonic and and a supersonic flow in the nozzle (Figure 2 and 3). The amplitude signal traces and the amplitude spectra have the same figures as the transducers in the sketch of the experimental arrangement. The sensitivity for the amplitude signals is equal for all transducers but in the spectra the sensitivity is different. The amplitude

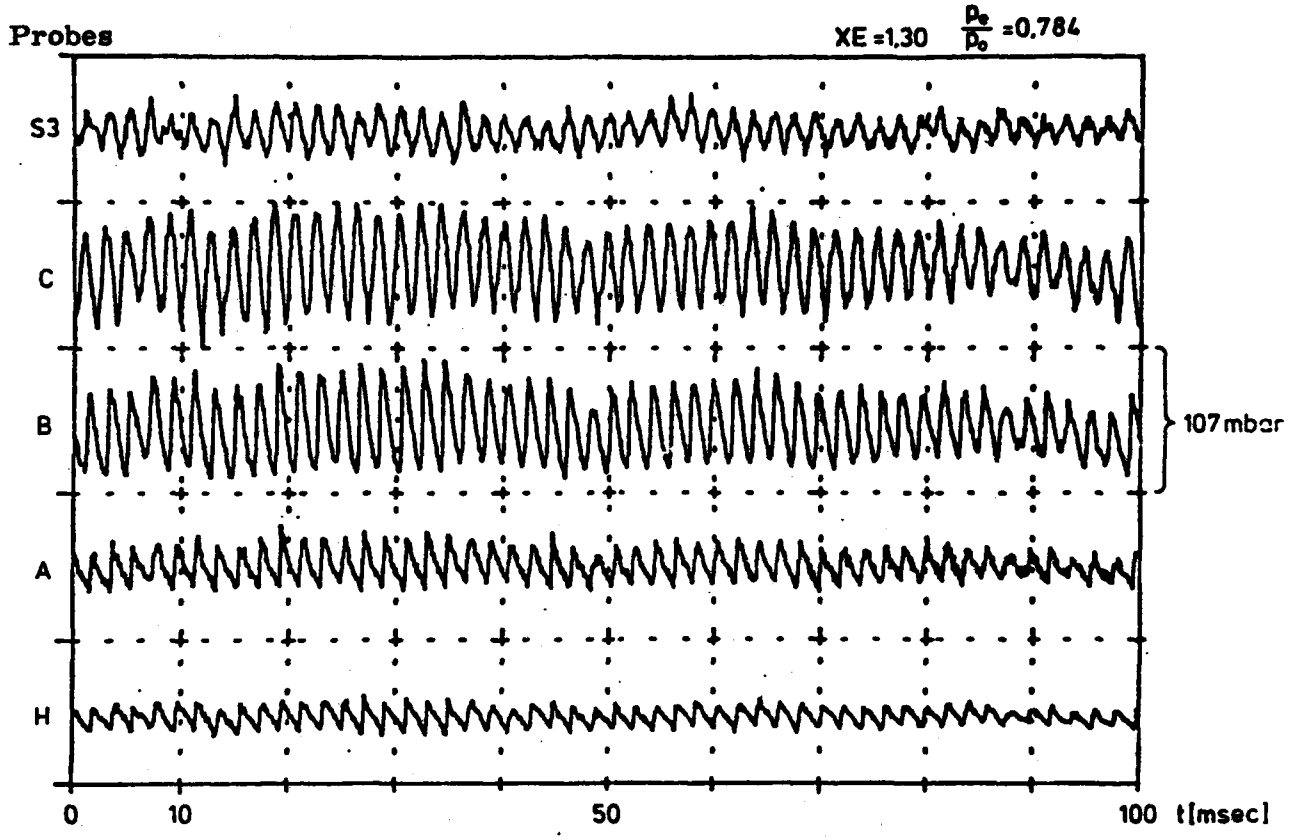

Fig. 2 above: Time signals of the wallpressure in the Laval nozzle at subsonic flow.

Fig. 2 below: Corresponding spectra with data of frequency, pressure amplitude and phase of the maxima.

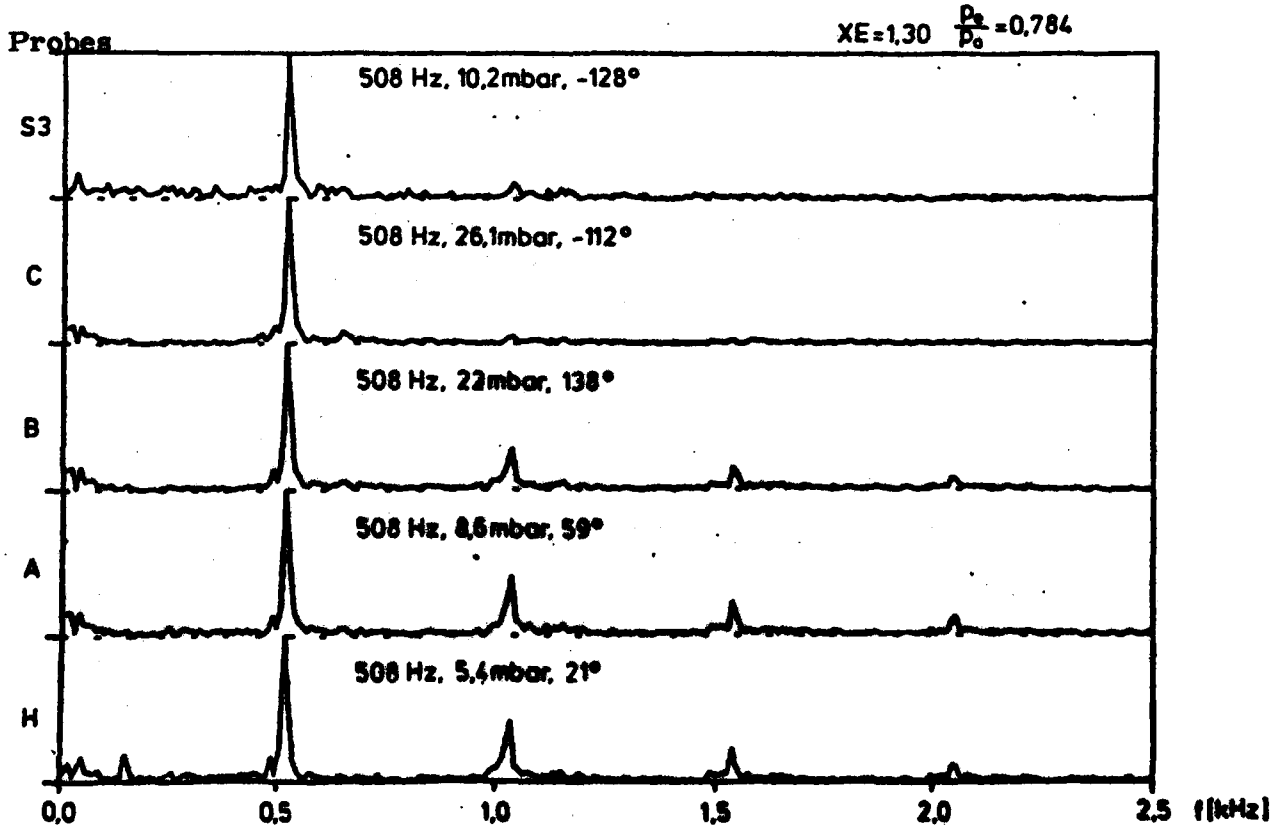

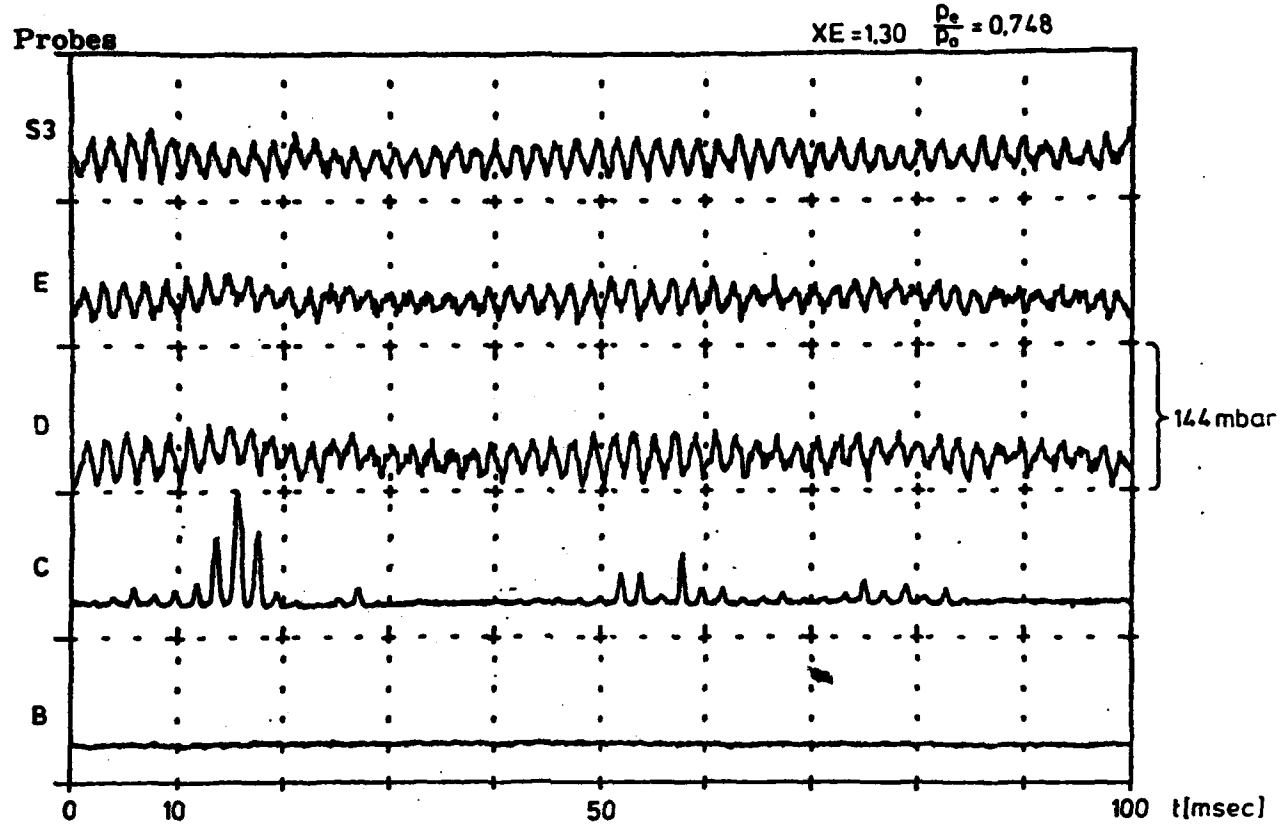

Figure 3 above : Time signals of the wallpressure in the Laval nozzle at ultrasonic flow.

Figure 3 below : Corresponding spectra with data of frequency. pressure amplitude and phase of maxima.

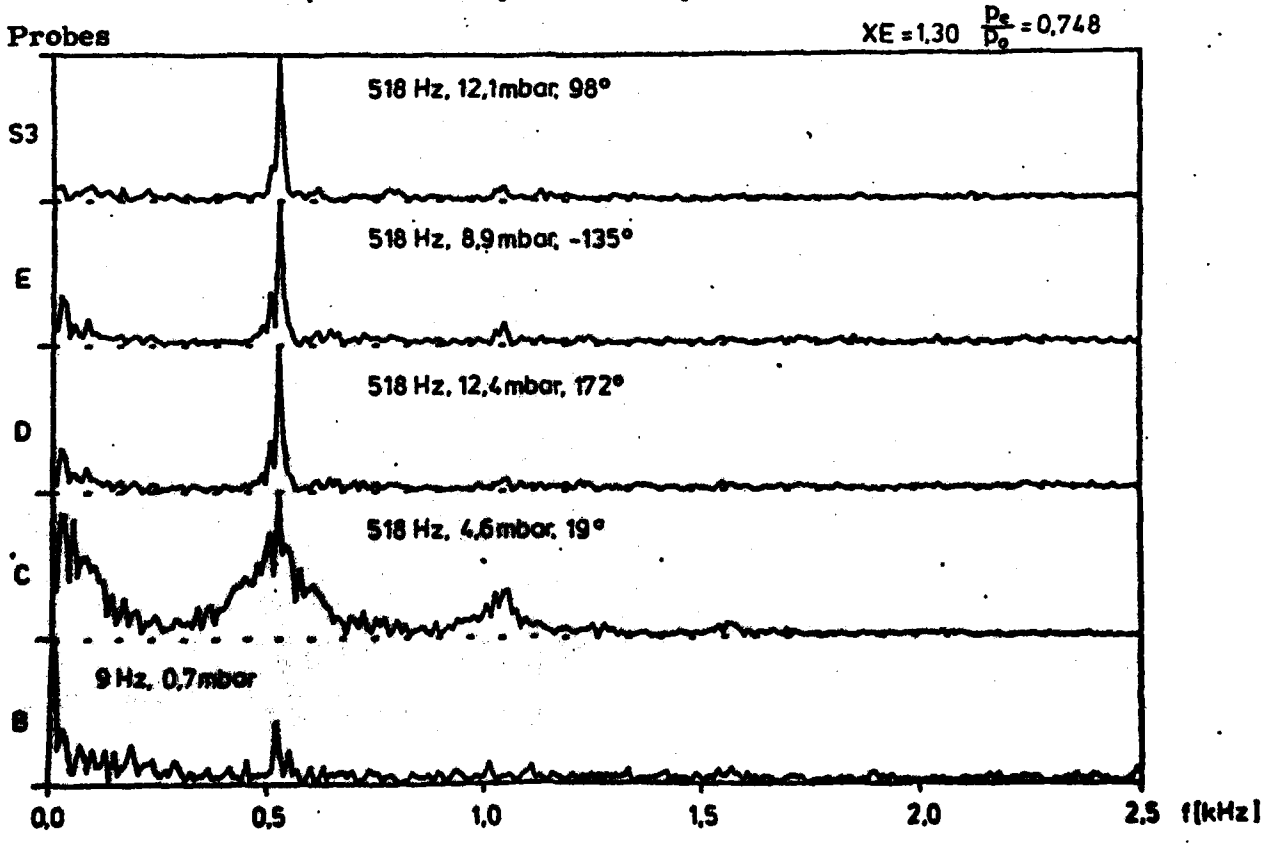

spectra of the signals are calibrated with the peak amplitude of the strongest signal and this amplitude is written in the diagram. For this signal there is also given a phase angle which is related to the same cosine function for all the spectra in one diagram.

For the case of the subsonic flow (see Figure 2) the more or less sinusoidal pressure fluctuations are penetrating upstream into the nozzle coming from the mixing chamber (see phase angles in the spectra). Propagating upstream the amplitude is increased (see signal traces). Upstream of the smallest cross section the distortions become peaky pressure waves (bang waves) and propagate through the intake flow into the supply field (laboratory). Because of the saw tooth shape for these signals we find a lot of higher harmonics in the spectra.

Supersonic conditions in the nozzle (see Figure 3) are indicated by the fact that no pressure fluctuations occur in the vicinity of the smallest cross section. A shock wave at the end of the supersonic flow regime is in the vicinity of the transducer for which the signals seem to be clipped at the lower amplitudes. There is no signal while the shock wave is downstream of the transducer. But if the shock wave is pushed upstream over the transducer by means of the pressure fluctuation there is a signal in the order of the pressure increase in the shock wave itself. It is also obvious from trace C in Figure 3 that the position of the shock wave is also influenced by a very low frequency in the order 20 Hz.

2.3 Generation of pressure fluctuations in the plenum chamber

In this paragraph we are concerned with the generation of the pressure fluctuations in the mixing chamber. On the one hand it is obvious that the fluctuations are generated by the outflowing jet from the nozzle. On the

other hand we have the idea that the frequency of the pressure fluctuations is determined by the geometry of the plenum chamber. In this case the mixing or plenum chamber should act as an acoustic resonator. To verify this idea we put seven piezo resistive pressure transducers in the walls of the mixing chamber and additionally we changed the geometry of the mixing chamber by a volume reduction of 25 %. These investigations led to the following results:

a) The resonance frequencies of the mixing chamber are depending on the pressure conditions for a height of 330 mm between 490 and 540 Hz and for the reduced height of 250 mm between 650 and 690 Hz. As stated, the frequency depends on the pressure conditions during the test and is increased with decreasing pressure p.

With the assumption of a lateral acoustic resonator one can calculate the resonance frequency for a standing wave of the first order (n = 1):

$$f = n \cdot c/2l \qquad (6)$$

For $l = 330$ mm we obtain $f = 515$ Hz and für $l = 250$ mm we obtain $f = 680$ Hz. This corresponds to the measured frequency for the transonic flow configuration in the nozzle.

b) The amplitudes of the pressure fluctuations are decreasing from the pressure transducer (S3) at the lower wall of the plenum chamber to the pressure transducer (S1) in the middle of the chamber. This is in accordance with the assumption of a standing wave pattern of first order, the pressure minimum of which is situated in the middle axis of the plenum chamber and the pressure maxima of which are situated at the upper and lower wall of the plenum chamber.

c) The phase difference between the upper and lower wall of the plenum chamber (transducers O1, O2 at the upper wall and transducers U1, U2 at the lower wall) is 180°. This is in accordance with the lateral standing wave because in this case we expect a phase jump of 180° over the pressure minimum in the middle of the resonator.

These investigations have proven that the plenum chamber acts like a resonator for a lateral standing wave. Now we explain how these oscillations are generated. From the interferograms of the outflow from the nozzle into the plenum chamber (Figure 4) we see that the outcoming jet is unstable. A short distance downstream of the end of the nozzle the jet boundary is oscillating and a little more downstream it is forming vortex-like structures. The direction of the jet is changed to the side of the stronger vortex, so one can understand that in this side of the plenum chamber the pressure is increased by means of the stagnation pressure of the jet. By this pressure increase possibly the whole jet is deflected to the other side of the plenum chamber. In such a way the plenum chamber can be excited to pressure oscillations of comparatively large amplitudes, the frequency of which is given by the acoustic resonance. This is a kind of filtering which amplifies from the frequency spectrum of the outflowing jet (Lit. 2) the resonance frequency of the plenum chamber mostly.

Figure 4: Interferogram of the jet flow into the plenum chamber for two different instances of time (left nozzle)

The influence of the pressure fluctuations inside the plenum chamber on the nozzle flow was achieved by a little unsymmetry in the position of the nozzle with respect to the mixing chamber axis (see Figure 1). By this shift to the upper side only the pressure fluctuations of the upper half of the plenum chamber act on the nozzle flow. If the nozzle is exactly in the center of the plenum chamber the basic mode of sound propagation into the duct would not be excited because of the phase jump in the center line of the plenum chamber.

A strong influence on the upstream propagation of the pressure distortions is observed for the separated flow case. When the acoustic waves have different propagation velocities in the core flow and the separated flow regime of the nozzle, a partial interference to lower amplitudes of the pressure fluctuations is observed. Because of the lower flow velocities in the separated flow regimes the propagation velocity of the acoustic waves is larger in this area. So this part of the wave can interfere with the slower propagating waves in the core flow.

This interference to lower wave amplitudes is also influencing the amplitudes of the jet oscillation in the mixing chamber and the amplitudes of the plenum chamber resonance. So the regime of pressure fluctuations for the whole system is limited to lower pressures without the occurrence of the flow separation in the nozzle.

The influence of the pressure ratio on the stability of a Laval nozzle flow connected with a plenum chamber can be seen from Figure 5. The regime of pressure fluctuations with large amplitudes in the plenum chamber and consequently also in the duct is located in a narrow frequency regime for the fundamental lateral resonance of the plenum chamber. The corresponding pressure ratio regime is $0.7 \approx p_e/p_o \approx 0.9$. The upper pressure limit is caused by the decreasing momentum of the outflowing jet which leads

to decreasing amplitudes of the plenum chamber oscillation. The diagram shows that for the case of the wider nozzle (XE =1.38, see also introduction) for a much wider pressure regime $0.5 = p_e/p_o = 0.9$ a lot of frequencies with smaller amplitudes occur in the signals of the pressure fluctuations of the plenum chamber. These oscillations are mainly due to the mixing noise of the jet and do not strongly affect the Laval nozzle flow.

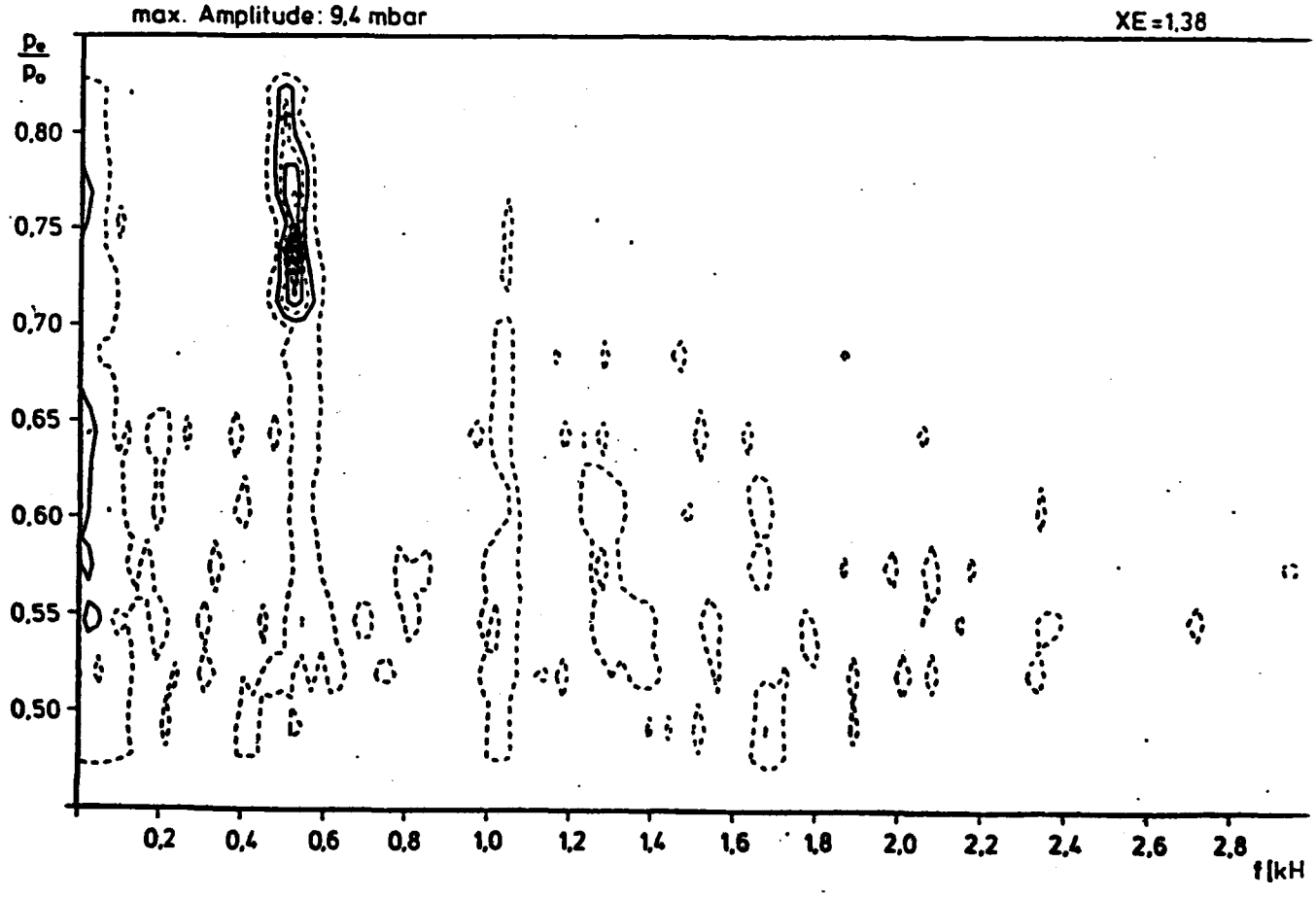

Figure 5: Plot of the peak frequencies of the amplitude spectra of the the pressure fluctuation in the plenum chamber for different pressure ratios of the Laval nozzle flow

3. The transonic flow in the Laval nozzle

3.1 The steady part of the flow

The observed pressure amplitudes in the Laval nozzle do not exceed 10 mbar for the case of the supersonic flow. With atmospheric pressure as a supply condition we have only a 1 % change by means of the unsteady pressure fluctuations. Therefore we can assume that for the purpose of theoretical considerations the problem can be devided into a steady basic flow and a superimposed acoustic wave. Only in the transonic case when the shock wave during a cycle of the acoustic oscillation is propagated through the small cross section of the nozzle into the intake flow and is reestablished during the period of flow acceleration more downstream in the divergent part of the nozzle,then because of the non-linearities and the large peak pressure amplitudes this assumption cannot be made (Lit. 3).

For the purpose of testing the one-dimensional treatment of the nozzle flow we have compared the calculated steady pressure distribution in the two hyperbolic nozzles with the wall pressure data and the density measurements from the interferograms (Figure 6). With respect to the interferograms one has to take into account that these are instantaneous pictures of the flowfield.

The calculated curves (solid lines) are valid for isentropic flow both upstream and downstream from the shock wave. By means of the equation

$$F = Q_e \, (p_o/p)^{1/k} \, (\varrho_o \, p_o \, 2k/(k-1) \, (1 - p/p_o)^{(k-1)/k})^{-1/2} \qquad (7)$$

to each cross section F of the nozzle for a given mass flow Q_e a non-dimensional wall pressure p/p_o can be calculated. The position of the normal shock wave is given by the pressure conditions for the shock wave

(p_u pressure upstream, p_d pressure downstream of the shock wave):

$$p_d/p_u = 4(p_o/p_u)^{(k-1)/k}/(k^2 - 1) - (k + 1)/(k - 1) \qquad (8)$$

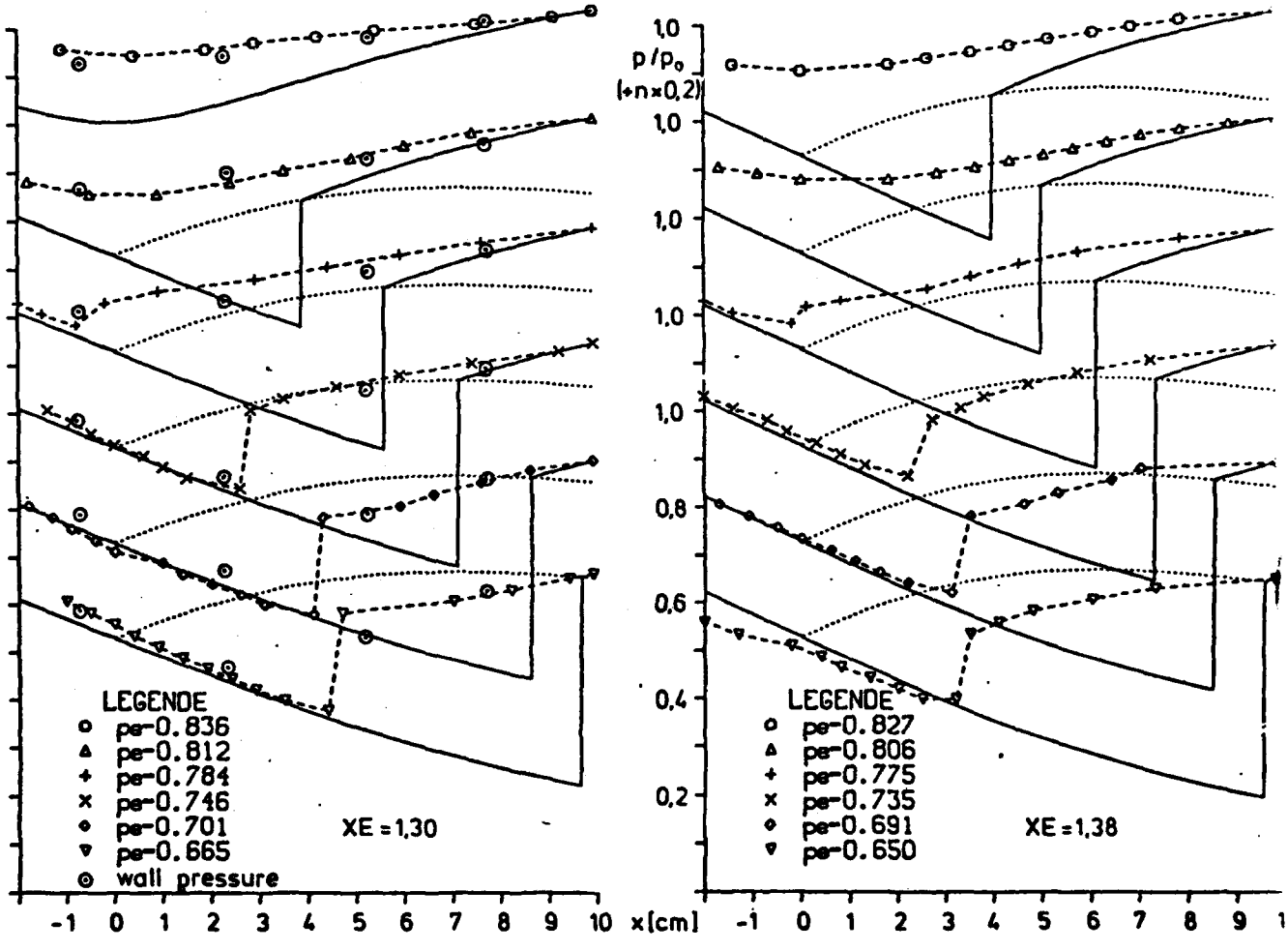

Figure 6: Comparison of the calculated pressure distributions (solid lines) for two Laval nozzles with different shape (see introduction) for different plenum chamber pressures p_e with wall pressure data and pressure values (dashed lines with points) calculated from the density measurements from instantaneous interferograms of the flowfield. The dotted lines are the possible downstream pressures of steady shock waves in the supersonic flow.

The curve for the possible downstream pressures of steady shock waves at the end of the supersonic flow regime is the dotted line in the diagrams. The pressure curves for the subsonic flow downstream of the shock waves are curves of smaller supply pressure due to the entropy increase in the shock waves. The comparison of the calculated and measured values shows that in the transonic case, especially when a shock wave is in the intake part of the nozzle flow, the difference can be fairly large. For the subsonic and also for the supersonic case the agreement is much better because the superimposed unsteady pressure fluctuations cause only small deviations from the average flowfield.

The small deviations from the calculated flowfield for the subsonic case have the origin in the influence of friction which is not included in the theoretical treatment. The dissipation of kinetic energy leads to lower velocities in the real case, so the measured pressures tend to be higher. By the same reason also in the supersonic case the pressure recovery in the subsonic part of the flow downstream of the shock wave is also much lower than calculated. This is due to the very thick boundary layers downstream of the shock waves in the flowfield with large pressure increase. The large part of the kinetic energy is tranferred to turbulent energy of the boundary layer. The boundary layer generally leads by the effective thickness generally to smaller duct cross sections than calculated from the nozzle contour. Especially in the supersonic flow case for a given plenum chamber pressure p_e the downstream pressure of the shock wave p_d is smaller than in the case without boundary layer. Therefore the shock is observed for lower plenum pressure p_e and additionally the position is more upstream than calculated.

For weak shock waves the measured downstream pressure fits the calculated downstream pressure curve (dotted line). In case of stronger shock wave the measured downstream pressure is obviously less than

the calculated one. In this case by means of the boundary layer influence oblique shock waves occur which lead to a lower pressure increase.

The comparison of the results of the two different nozzles shows that the agreement between measured and calculated data is better for the narrow nozzle. This unexpected behaviour is explained by the fact that in the case of the wider nozzle in the expanding downstream part a thicker boundary layer is formed and also separation occurs for lower Mach numbers. Therefore the influence of friction is larger in this case and the one-dimensional theoretical treatment gives less accuracy.

3.2 The propagation of pressure fluctuations

On the propagation of the pressure fluctuations inside the nozzle we can get information by comparison of the phase of the signals from the different pressure transducers. This is possible because for a certain pressure ratio p_e/p_o only pressure fluctuations of a single frequency occurred. A phase difference $\Delta\varphi$ of the signals of two transducers corresponds to a travelling time t_l

$$t_l = \Delta\varphi/2\pi \cdot f \tag{9}$$

If the pressure fluctuations behave like acoustic waves in the basic duct mode they propagate with sonic velocity c upstream in the flow and have a propagation velocity v relative to the flow with the velocity u

$$v = c - u \tag{10}$$

Because the flow velocity u in the divergent part of the nozzle downstream of the shock wave is increasing the travelling time between equally distant

locations of the transducers will increase. This is obvious from the phase diagrams in Figure 7 and 8 if one takes into account that a larger increase of the curve for the plotted phase angle corresponds to a longer travelling time. Especially for the case of the pure subsonic flow in the nozzle (see Figure 7) the increase in phase angle is much smaller than in the transonic case (see Figure 8).

To verify the propagation velocity v of the disturbances we have calculated the local velocity of sound c from the average local pressure values

$$c = k\sqrt{p/\varrho} \tag{11}$$

and also the flow velocity

$$u(p) = c_o \sqrt{(2/(k-1))\,(p_o/p)^{(k-1)/k} - 1} \tag{12}$$

The corresponding travelling times are plotted with crosses (+) into the diagrams of Figure 7 and 8. The comparison shows that the measured disturbances propagate a little faster than the calculated ones. This is due to the total head pressure losses by means of the shock wave and other friction effects. With the assumption of a head pressure loss equivalent to the differences between the measured and calculated pressures for a nozzle flow we achieve a much better agreement with the measurements (+).

The amplitude of the upstream travelling distortions which is indicated by the dashed line in the diagram (- - -) is increasing up to the transducer C. This has two main reasons. First, the distortions travel into a flow regime of lower density and smaller cross section and for constant energy flux the amplitude has to increase. Second reason is that in the vicinity of the steady shock wave also comparatively small distortions can cause large pressure fluctuations by moving the shock wave upstream and downstream in the flowfield.

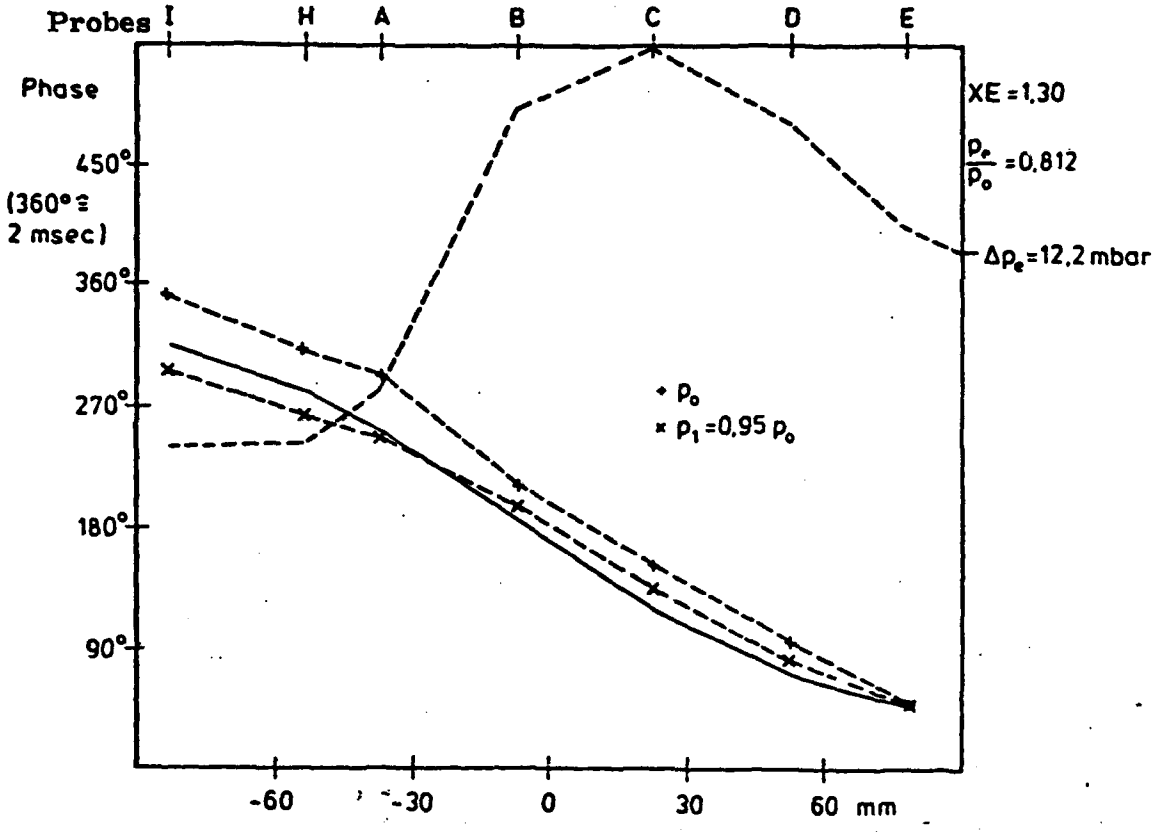

Figures 8 and 9 : Travel time diagrams of the expansion of the upstream pressure disturbances. (to the left)

drawn line : wallpressure measurements
dash dotted line: calculated values
dashed line : continuous run of the amplitudal curve

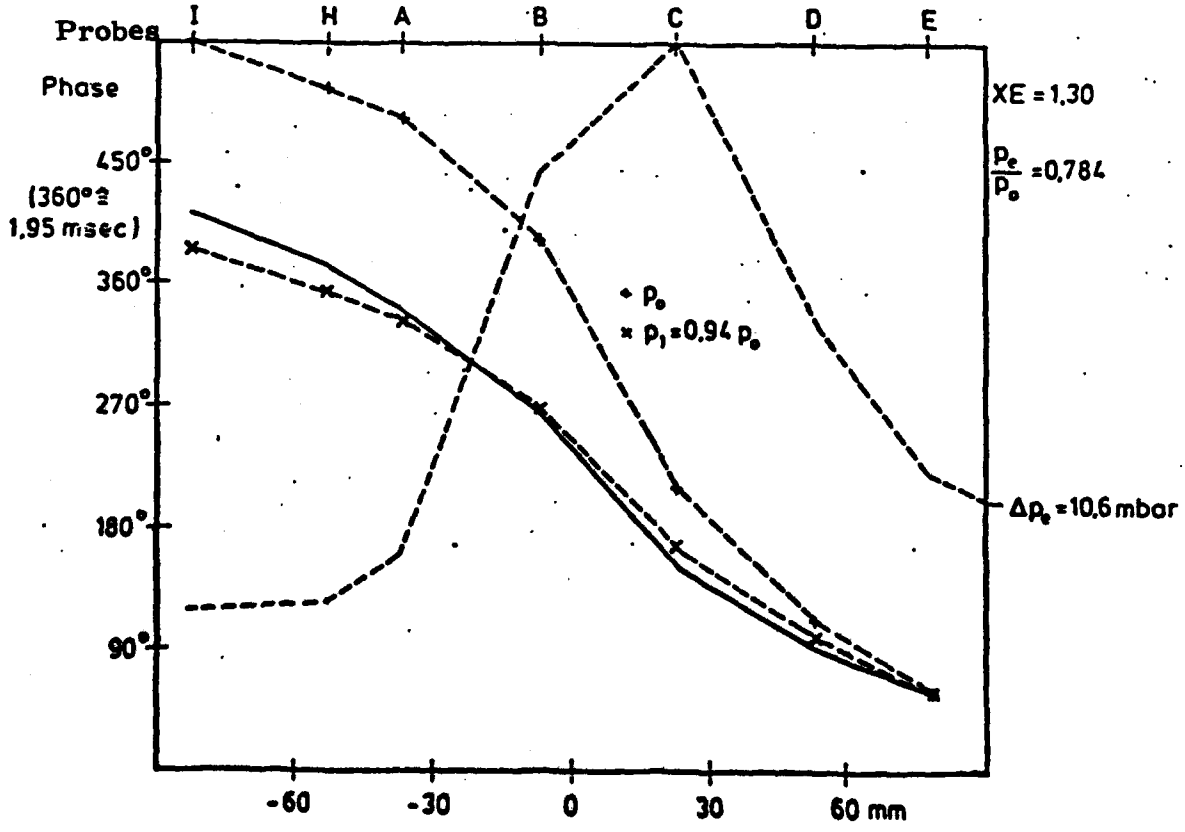

4. Evaluation of the change in shock position

4.1 Quasi steady model calculation

For increasing plenum chamber pressure p_e the steady shock wave in the nozzle flow is positioned more and more upstream (see Figure 9). For lower pressures the shock position is moving downstream. Evidently for periodic pressure fluctuations in the plenum chamber or the downstream part of the nozzle flow, the position of the shock wave will also be periodically moved. This idea leads to a simple quasi-steady model calculation for the shock motion amplitudes. For a given pressure fluctuation amplitude Δp_e at the end of the nozzle we calculate different shock positions which correspond to the pressure $p_e + \Delta p_e$ and the pressure $p_e - \Delta p_e$. These extreme shock positions are indicated by the ends of the arrows in the lower part of Figure 9.

In this quasi-steady model calculation we assume that the distortions are immediately acting on the shock wave without any travelling time for the distance from the plenum chamber to the shock wave inside the nozzle flow. So these quasi-steady considerations are only valid for very low frequencies for which the shock wave has no phase lag to the periodic pressure fluctuations in the plenum chamber and also for very small amplitudes for which the pressure of the distorted flow does not deviate too much of the steady flow in the nozzle (Lit. 4).

4.2 Small parameter distortion model

An equation of motion for the shock wave is achieved by linearization of the gasdynamic equations of a two-dimensional flow. This has been done already by several authors (Lit. 5-7). Following mainly Adamson, Messiter

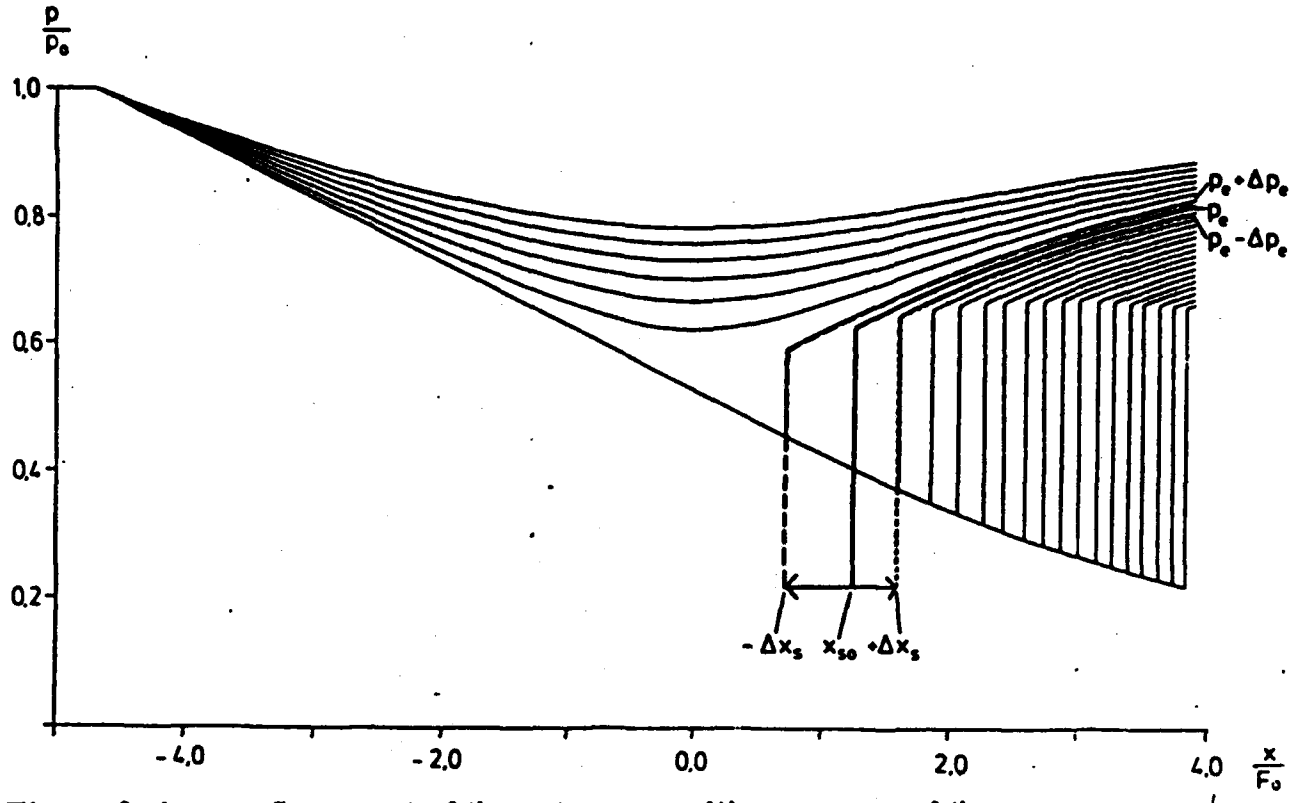

Figure 9 above : Statement of the extreme positions $\pm \Delta x_s$ of the compressional shock at position x_{so} at a given pressure amplitude $\Delta p_e / p_o = 0.01$ by the discharge pressure p_e according to the streamline theory.

below : Change of position of the compressional shock at the stationary position x_{so} (drawn line) with a constant pressure amplitude Δp_e for various mixing chamber pressures p_e / p_o.

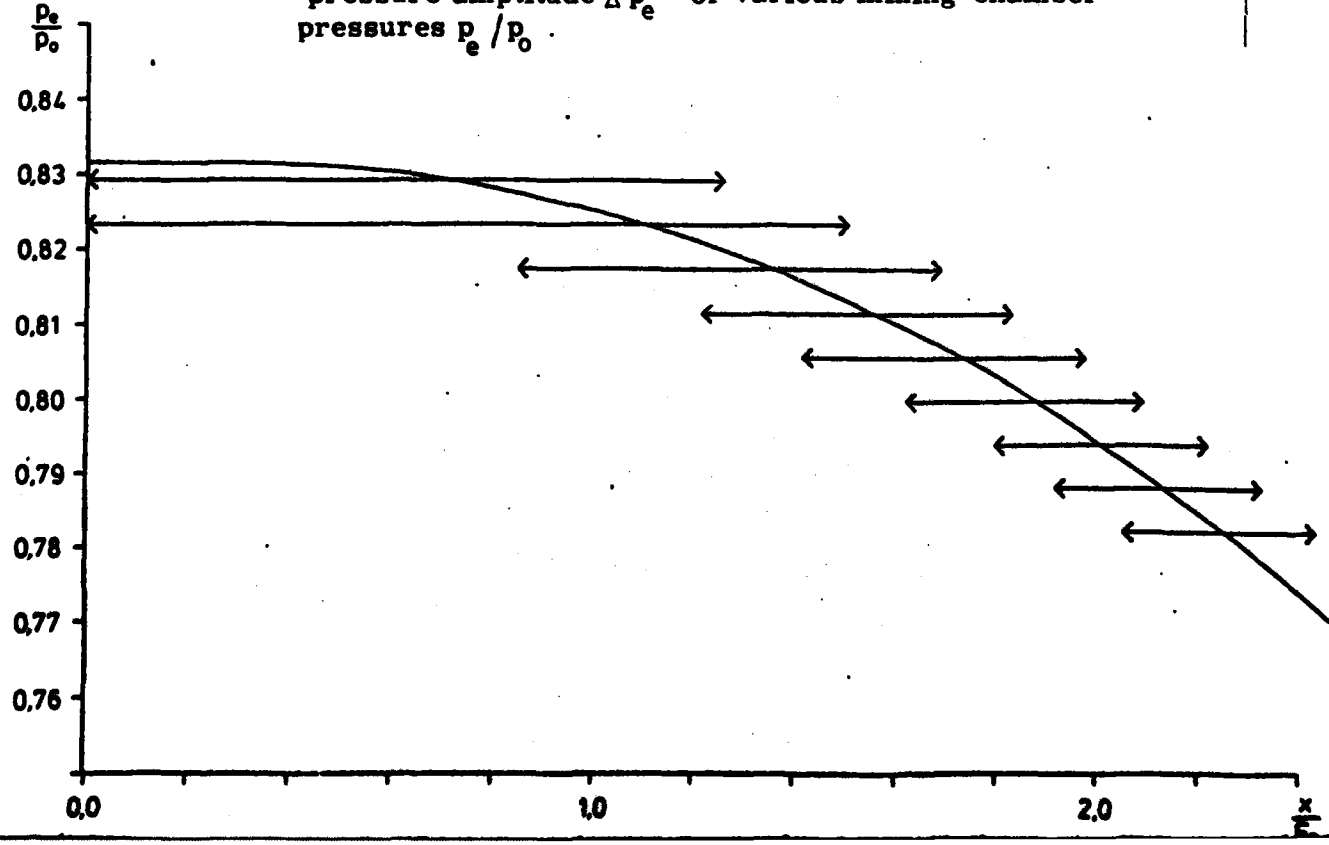

and Liou (Lit. 5) we assume that the flow potential of the two-dimensional flowfield can be described by a potential deviating only a little from the potential of a steady flow in the nozzle with a critical velocity a^* through a duct with a constant cross section F_o. This leads to the following expansions for the components of the flow velocity

x-component $\quad U = 1 + \varepsilon u_1 + \varepsilon^2 u_2 + \ldots$

y-component $\quad V = \varepsilon^2 v_2 + \ldots$

All other flow parameters G also deviate only a little from their values in the steady flow in the smallest cross section of the duct. Normalizing the quantities with the critical quantities we achieve

$$G = 1 + \sum_{i=1}^{n} \varepsilon^1 g_i \qquad (14)$$

The small parameter is in the i-th power factor of the distortion of the i-th order. The restriction on quantities of second order is justified because only transonic flow with $U - 1 = 0(\varepsilon)$ is described by the equations and by the fact that the contour has a maximum curvature of the order of ε^2 in the smallest cross section (y = L)

$$y_w = 1 + \varepsilon^2 f(x) \qquad \text{(normalized by L)} \qquad (15)$$

For the interpretation of the unsteady behaviour of the flow a ratio of the period T of the pressure fluctuations to the travelling time t_l of the distortions up to the shock wave is the most important parameter. To get this ratio we first of all estimate the travelling time in the duct. If the velocity of the flow downstream of the shock wave is given by

$$v_d = a^*(1 - \varepsilon) \qquad (16)$$

and the propagation velocity of the distortion

$$v_s = a^* \tag{17}$$

the travelling time of the distortion for the distance L is

$$t_l = L/(v_s - v_d) \tag{18}$$

if all time parameters are normalized with the time

$$t_n = L/a^* \tag{19}$$

one gets the ratios

$$T/t_l = \varepsilon\tau \qquad \tau = T/t_n \tag{20}$$

For the case $\tau = (k\varepsilon)^{-1}$ with $k = 1$, the period of the pressure fluctuation is nearly as large as the travelling time t_l and we achieve a phase difference of 2π between the pressure fluctuations in the plenum chamber and in the vicinity of the shock wave.

For the case $\tau = (k\varepsilon^2)^{-1}$ the frequency of the pressure fluctuations is for the same travelling time one order of ε smaller, so T is correspondingly larger and this means that the distortions at the shock wave have nearly no phase lag to the pressure fluctuations in the plenum chamber.

While the time in the timedependent terms of the gasdynamic equations was normalized with t_n, the times in the small parameter terms will be normalized by the period T. With this normalization the solution for the first case with the large phase lag is completely different from the steady flow solution (Lit. 6). For the second case with no phase lag we achieve solutions which

agree with the quasi-steady description of the flowfield which was formerly discussed (Lit. 7). For this latter case we can achieve the following equation for the change of the shock position in the vicinity of the steady position x_{so}

$$4K\,\dot{x}_s/(k+1) = -\,(C_{2d} + 2k\,C_u^{\,3}/3 + G(t))/C_u \qquad (21)$$

The time function G(t) is proportional to the amplitude of the pressure fluctuation in the plenum chamber. The quantity C_u is the velocity of the first order in front of the shock wave and depends on the position of the shock. The quantity C_{2d} is defined by the steady position of the shock wave and can be calculated from the equation (21) for the case ($x = x_{so}$, $G(t) = 0$, $\dot{x}_s = 0$).

$$C_{2d} = -\,2k\,C_u^{\,3}(x_{so})/3 \qquad (22)$$

4.3 Numerical solutions for the narrow nozzle

For the case of the narrow nozzle (XE = 1.3, see introduction) we now calculate some data from the theoretical considerations with the help of the geometrical and experimental parameters of this nozzle. From the frequency f = 500 Hz of the distortions coming from the plenum chamber we achieve with L = 25 mm, $c^* = 315$ m/s, T = 2 ms:

$$\tau = 25$$

For the case $\tau = (K\varepsilon^2)^{-1}$ which is the closest one to the experiments and for K = 1 we achieve

$$\varepsilon = 0.2$$

Now for this ε we have to write the contour of the nozzle in the form

$$y_w = 1 + \varepsilon^2 f(x) \tag{15}$$

This can be done by approximation of the hyperbolic shape of the contour by a parabolic one for small x

$$y = \sqrt{1 + x^2} \approx 1 + x^2/2 \quad (x \ll 1) \tag{23}$$

For the nozzle shape with $f(x) = a\,x^2$ we get for a at this nozzle exit

$$a = (XE - 1)/(\varepsilon^2 x_e^2) \tag{24}$$

For the first order of velocities in the nozzle we have the equation

$$u_1 = \pm \sqrt{2 f(x)/(k + 1)} \tag{25}$$

So we get for the velocity in front of the shock

$$Cu\,(x_{so}) = \sqrt{2a/k+1}\; x_{so} \tag{26}$$

For the pressure fluctuation we assume a simusoidal time dependence

$$G(t) = G_o \sin(t) \tag{27}$$

The amplitude G_o is related to the pressure fluctuation p_e at the duct exit by the equation for the pressure P_b at the end of the nozzle

$$P_b = 1 - \varepsilon\, k\, u_1(x_e) + \varepsilon^2 k \left(\frac{2k - 3}{6}\, u_1^2(x_e) - \frac{C_{2d} + G(t)}{u_1(x_e)}\right) \tag{28}$$

For a given C_{2d} we achieve:

$$\Delta P_b = \varepsilon^2 k G_o / u_1(x_e) \tag{29}$$

P_b is normalized with the critical pressure p^* and we achieve

$$\Delta P_e = p^* \Delta P_b = p^* \varepsilon^2 k G_o / u_1(x_e) \tag{30}$$

For the measured value of p_e of 10 mb we get G = 0.83. For this case we have calculated the motion of the shock wave for different x_{so} (Fig. 10). We can see from this diagram that for a certain upstream position the shock wave can no longer stay inside the nozzle flow during one cycle of the oscillation.

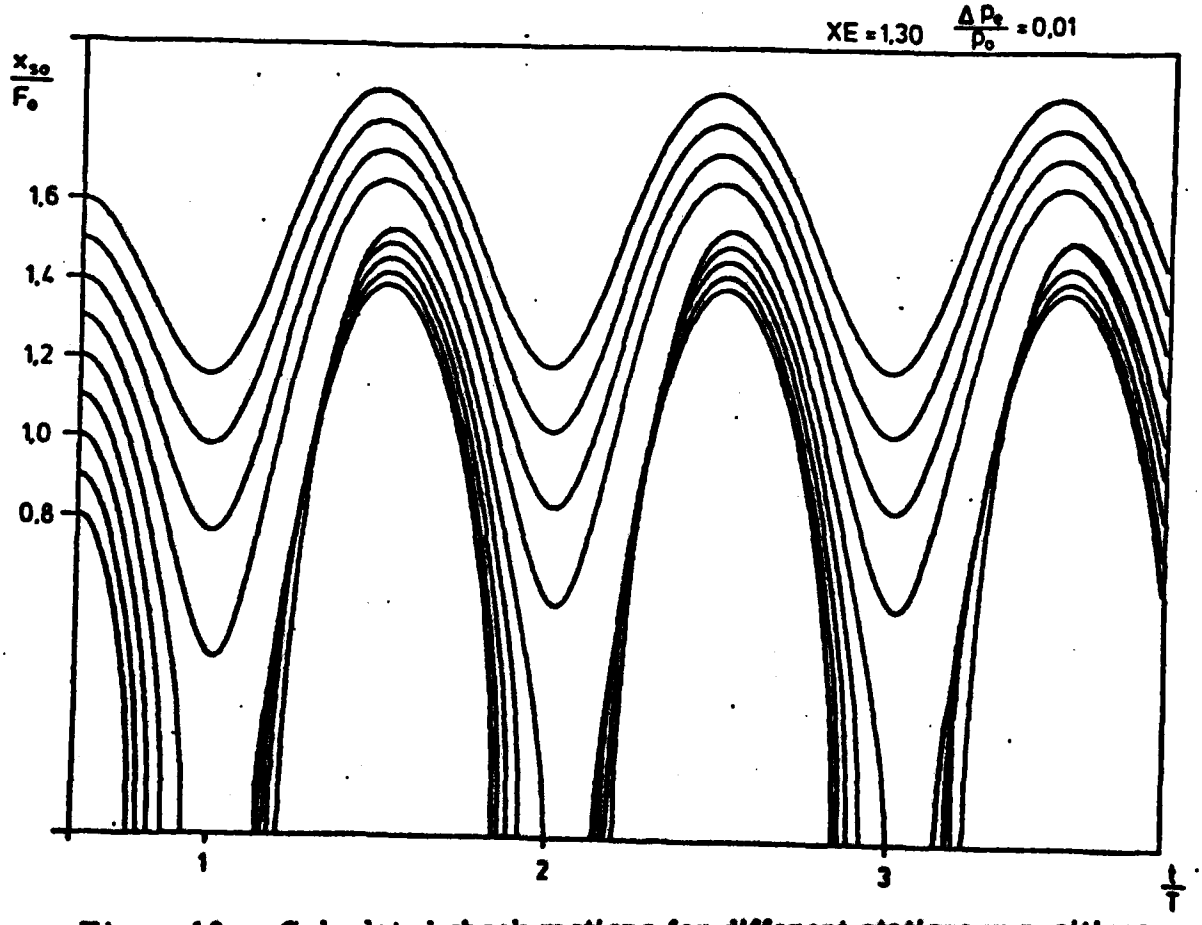

Figure 10: Calculated shock motions for different stationary positions x_{so} for a pressure fluctuation with the period T

4.4 Comparison of the calculations with the experimental results

In the diagram of Figure 11 the calculated changes of shock position are plotted against the stationary position of the shock wave. The upper curve gives the extreme change in position of the shock wave upstream the lower curve the motion downstream. The results are fairly similar for both the small parameter and the quasi-steady theory. For a far downstream position the changes in shock position are fairly symmetrical in both directions and for both theories. But in the vicinity of the smallest cross section the amplitude of the upstream motion becomes much larger than the amplitude of the downstream motion. It is also obvious that the quasi-steady theory predicts too small amplitudes for the upstream motion of the shock wave.

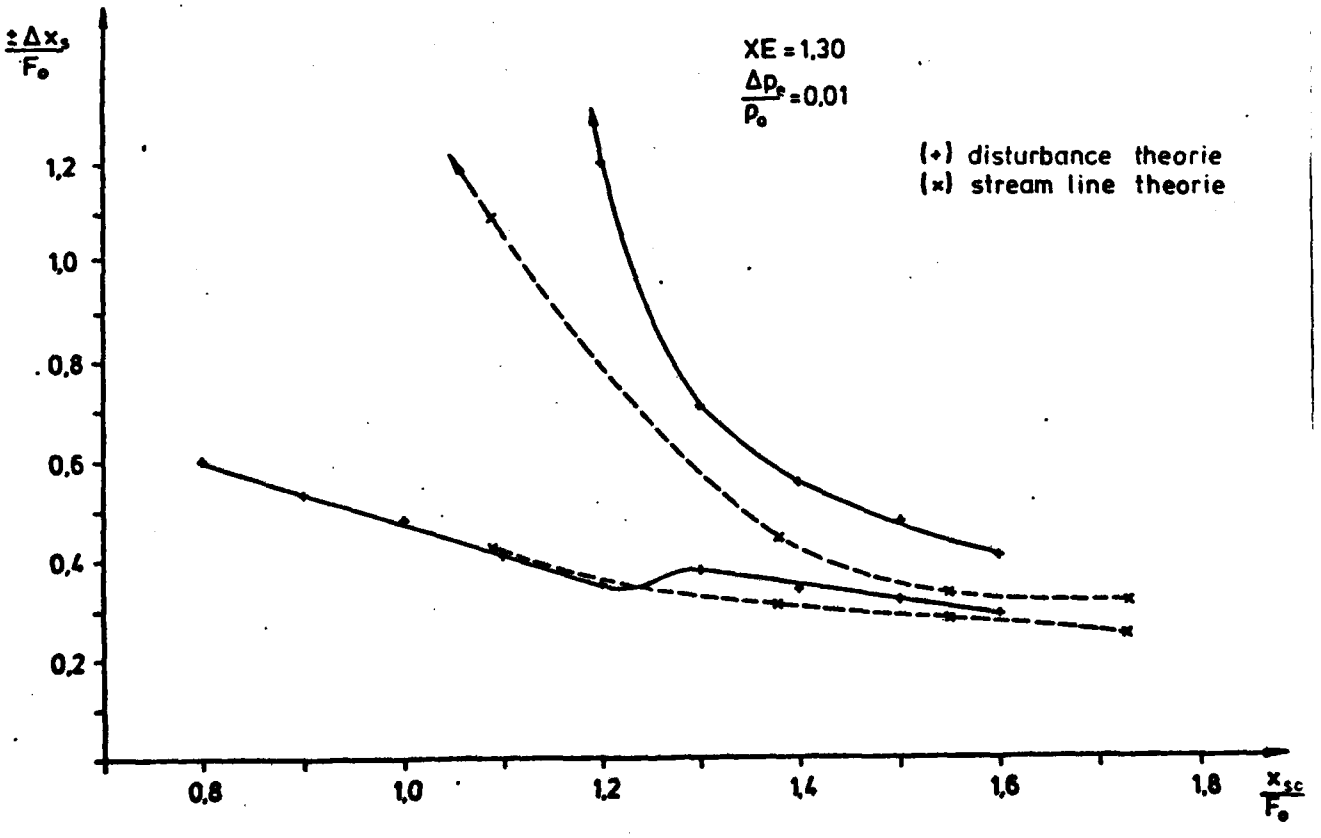

Figure 11: Comparison of the extrema changes in shock position $\pm$ x_s for different stationary shock positions x_{so} (the two upper curves give the amplitude of upstream motion, the two lower curves the amplitude of downstream motion for the given disturbance of chapter 4.3)

For comparison of these theoretical results with the experiments we have estimated the extreme positions of the shock waves from the recorded pressure traces (see Figure 3). The influence of the shock on the pressure signals (steap or clipped traces) allows an estimate of the changes of the shock position between the positions of the transducers. By these considerations we obtain the following estimates from the time pressure signals:

For a stationary shock position in the vicinity of the smallest cross section ($x = 0$) the extreme downstream position during a cycle of motion is smaller than $x = 0.8$. For a stationary shock position $x = 0.8$ the extreme shock motion upstream is not moving the shock waves through the smallest cross section into the intake. This is in accordance with the theoretical findings plotted in Figure 10. As a general result we can state that the measured changes of shock positions in the nozzle flow are not larger than the theoretically predicted changes in shock position.

For stationary positions more downstream in the nozzle ($x = 1.4$) we could not obtain experimental results because of the occurrence of the flow separation. The upstream propagation of the pressure fluctuations from the plenum chamber to the shock was damped very much. In this case the changes in shock position are very small.

In the small parameter perturbation theory for the transonic case one assumes an occurrence of a new shock wave in the smallest cross section of the nozzle at the time t^*

$$G(t^*) = -C_{2d} \tag{31}$$

This occurs at a certain time after the shock wave of the foregoing cycle of oscillation has passed through the smallest cross section into the intake flow. This result is in accordance with the condition of the quasi-steady

theory that a shock wave is formed in the smallest cross section when the critical pressure p^* is reached during the acceleration of the flowfield in the nozzle. Experimental observations with the Mach Zehnder interferometer show a similar result (see Figure 13). The only difference is that by means of steepened pressure distortions in the phase of acceleration, several weak shock waves are formed in the vicinity of the smallest cross section. These small shock waves form later moving downstream a stronger shock by merging together.

4.5 Some special results for the transonic case

For the transonic case, when the shock wave during one cycle of oscillation is moving upstream into the intake, it is interesting to plot the pressure signals of all pressure transducers in the duct over the duct length and some cycles of oscillation. For this purpose we have plotted iso lines of the wall pressure into x/t diagram (Figure 12).

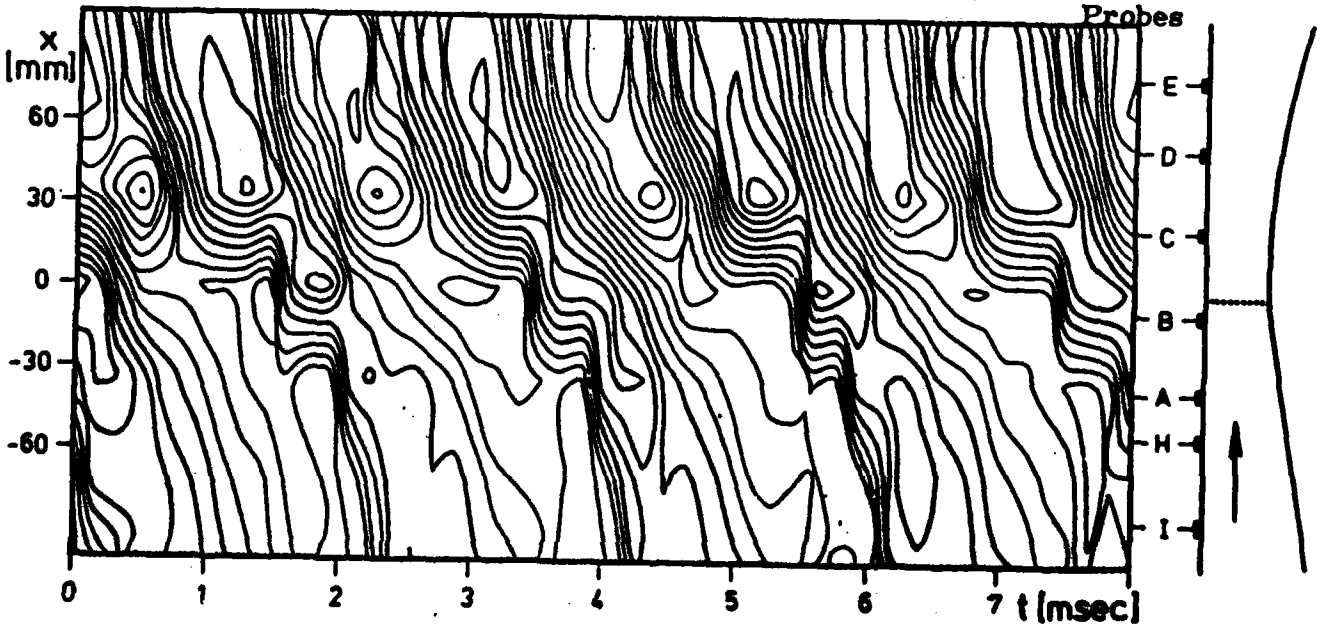

Figure 12: Pressure changes in length and time in the narrow Laval nozzle (the iso lines are lines of constant pressure)

From the inclination of the lines in flow direction one can immediately estimate the propagation velocities of the distortions. From the small inclination of the pressure lines in the vicinity of the smallest cross section one can deduce, that the distortions are slowing down very much in this part of the nozzle flow before moving upstream into the intake nozzle. This can also be seen from another type of plots we have used for the visualization of the motion of pressure disturbances in the nozzle flow. In Figure 13 we have plotted a sequence of instantaneous wall pressure distributions in one diagram. Pressures which are higher than the average pressure are indicated by dashed lines and pressures which are lower than the average pressure are indicated by dotted lines. Also from this diagram one can see how the dotted low pressure regime or the dashed high pressure regime is moving upstream. Especially the sudden changes between 1.4 ms and 1.6 ms in this diagram are due to the sudden motion of the shock wave into the intake flow of the nozzle. A certain time before this event (t = 0.8 ms) the flowfield has been accelerated. In the accelerated flowfield a distortion downstream of the smallest cross section is forming a weak shock wave. This shock wave is amplified by the acceleration of the supersonic flow and kept in its position by an increase of the downstream pressure by means of the upstream moving pressure distortions. The shock position is suddenly changed when the pressure in the intake flow is decreasing because the foregoing shock wave has left the intake point. While the shock wave is passing through the intake flow the low pressure field is moving upstream into the area of the smallest cross section and is accelerating the flow to supersonic velocities.

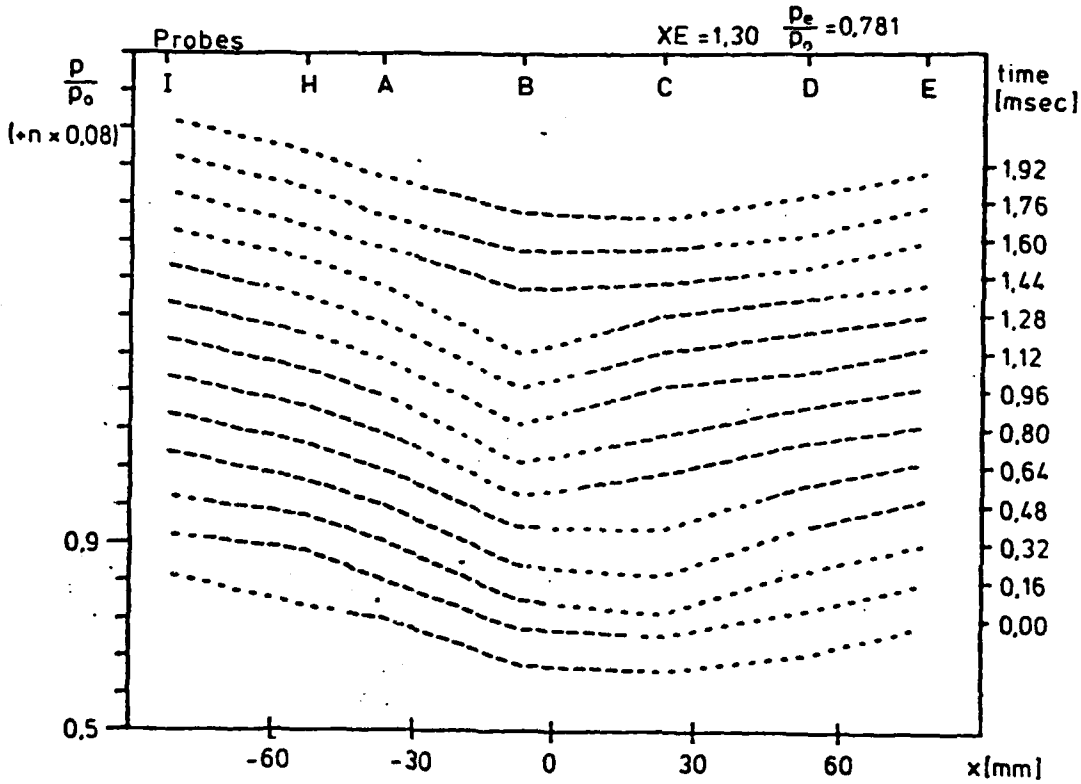

Figure 13: Sequence of instantaneous wall pressure distributions during one cycle of pressure fluctuations (dashed sections of the curves: pressure larger than the average pressure; dotted parts of the curves: pressure lower than the average pressure).

5. Automatic evaluation of the interferograms

Figure 14 shows a sequence of four interferograms which are shown to give a typical sequence of flow situations for the transonic case. In the first frame one can see several shock waves coming from downstream (plenum chamber), merging together in the shock wave at the end of the supersonic flow regime. In the second frame this shock wave has become stronger and has also moved upstream a little bit closer to the smallest cross section. In the third frame the shock wave has already passed the smallest cross section and is now propagating into the subsonic flow of the intake. This can be seen also in the fourth frame, where the shock wave is just leaving the intake flow on the left side of the frame while a new shock wave is already formed by acceleration of the flowfield and distortions from downstream in the center part of the flowfield.

These interferograms now have been evaluated with the help of a computer program which was developped in the last years in our department and is still under investigation. Figure 15 shows the digitized interference fringes of the four frames.

The number of lines in Figure 15 is just twice the number of fringes in Figure 14. This is due to the fact that the automatic fringe detection program gives one line for the right and another one for the left contour of a fringe.
After a complicated procedure of automatic fringe improvement and fringe numbering one can calculate density profiles from these fringe pictures. The density profiles for a height $y = 12.5$ mm are given in Figure 16.

The density profiles of Figure 16 show a close relation to the instantaneous pressure distributions of Figure 13. Especially the motion of shock waves and the change in density distribution along the duct center during one cycle of distortion can be clearly seen from these diagrams.

Bild 1

Bild 2

Bild 3

Bild 4

Figure 14 : Time sequence of interferograms of the nozzle flow in the transonic case (XE=1.30 p_e / p_o = 0.77)

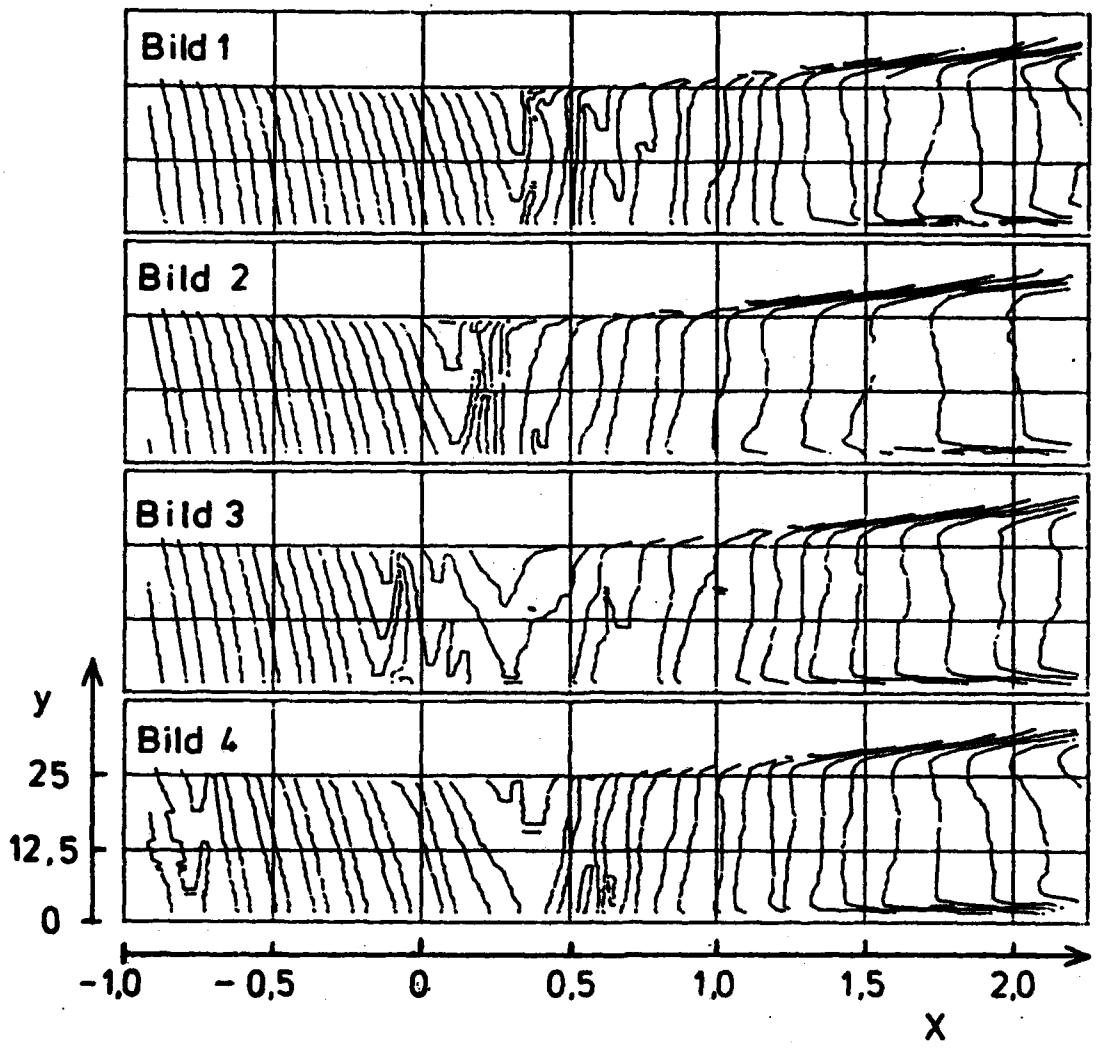

Figure 15: Digitized interference fringes of the frames of Figure 14

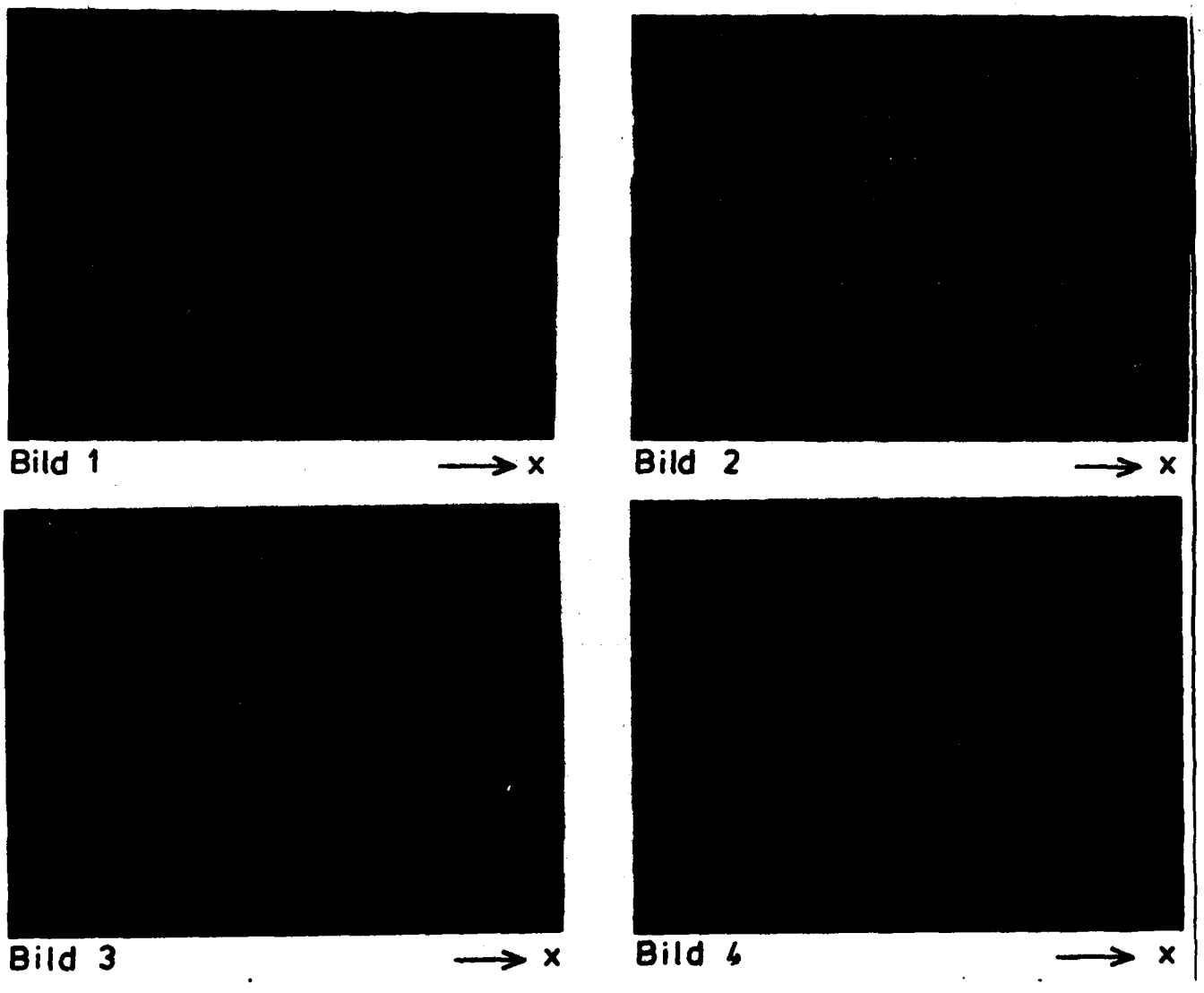

Figure 16: Density profiles in the center of the Laval nozzle flow (F = 12.5 mm). The density is given in relative units (fringe numbers).

6. Some concluding remarks for the nozzle experiments

The result of the Laval nozzle investigation is, as already stated in the introduction, that we can divide the unsteady behaviour of the flow in two main cases. The first one treated already in earlier investigations is the case of strong and forced oscillations of the whole Laval nozzle flow for a certain regime of pressure ratios (for air flow $0.85 \approx p_1/p_o \approx 0.66$ [1]). These forced oscillations occur mainly for symmetrical two-dimensional nozzles where a large area of separated flow can connect the plenum chamber pressure to the flow regime, where the shock wave is situated. For this forced oscillation it is also important that there is a certain agreement between the natural frequency of the transonic instability and the acoustic resonance of the downstream duct system.

The other type of instability which was especially investigated in the frame of this work, is strongest, if the flow is not separated in the downstream part of the duct, and acoustic distortions which are generated by a downstream instability of shear layers, supported by acoustic resonance of cavities, are travelling upstream in the subsonic part of the Laval nozzle flow and are acting on the shock wave at the end of the supersonic part of the flowfield. In special situations, which we have called the transonic case, the interaction of these distortions and the shock waves can be comparatively strong as in the case of the strong oscillations. Then the shock wave can also leave the nozzle flow through the smallest cross section into the subsonic intake flow. For higher supersonic Mach numbers in the nozzle this means smaller pressure ratios, the acoustic distortions result only in small amplitude shock oscillations. For the case of flow separation we have observed a large damping for the upstream travelling distortions and consequently very small amplitudes of oscillations.

Literature

[1] Meier, G.E.A.: Ein instationäres Verhalten transsonischer Strömungen. Mitteilungen aus dem MPI für Strömungsforschung und der AVA, 1974, Nr. 59.

[2] Yu, J.C. and Dixon, N.R.: Experimental Study of Sound Radiation from a Subsonic Jet in Simulated Motion. AIAA J., April. 1980, Vol. 18, No. 4, pp. 427.

[3] Chin, Wilson, C.: *Nonlinear Formulation for Low-Frequency* Transonic Flow. AIAA J., 1978, Vol. 16, No. 6, pp. 616.

[4] Nixon, David: On Unsteady Transonic Shock Motions. AIAA J., 1979, Vol. 17, No. 10, pp. 1143.

[5] Adamson Jr., T.C., Messiter, A.F., and Liou, M.S.: Large Amplitude Shock-Wave Motion in Two-Dimensional, Transonic Channel Flow. AIAA J., Dec. 1978, Vol. 16, No. 12, pp. 1240.

[6] Richey, G.K. and Adamson, Jr., T.C.: Analysis of Unsteady Transonic Channel Flow with Shock Waves. AIAA J., Aug. 1976, Vol. 14, No. 8, pp. 1054.

[7] Chen, J.S.K. and Adamson Jr., T.C.: Unsteady Transonic Flows with Shock Waves in an Asymmetric Channel. AIAA J., Apr. 1978, Vol. 16, No. 14, pp. 347.

1. Introduction

The aim of this project is to investigate vortex-profile interaction. Vortex interaction with solid walls generates sound. Vortex noise occurs nearly everywhere in aerodynamics and especially it is one of the helicopter noise sources.

There is lack of knowledge about the near field flow at the profile, thus experiments must be carried out. The first step to the problem is an experiment that gives an overview on the occurring phenomena. In the transonic duct a profile is placed in the wake of a cylinder. The interaction of a Karman vortex street and a profile can be measured by pressure transducers and high speed interferograms.

Additionally a shock tube experiment was performed. Single starting vortices are generated. The boundary layer in this case is very thin. The vortices are similar to potential vortices. These ideal conditions allow quantitative comparisons to theoretical results.

2. Experimental Facilities

2.1. Duct, Vortex Generators and Profiles

The transsonic duct (Fig. 1) is a vacuum type wind tunnel with two vacuum tanks of 132 m^3 and 24 m^3 volume [1]. The maximum measuring time for the profile investigation arrangement is 10 s at Mach 1 and 25 s at Mach 0.3. A new experiment can be performed every 4 minutes (This is the time, the pump needs to evacuate the tanks).

The air is sucked in from the labaratory or an air drying unit. The velocity in the measuring chamber is controlled by an adjustable diffusor. In the smallest cross section of the diffusor the air reaches Mach 1; so there is constant velocity throughout the measuring time. The velocity of the air can be chosen from v=0 to v=600 m/s if a Laval nozzle is used.

The test section of the duct (Fig. 5) is 800 mm long, 330 mm high and 100 mm wide. The upper and the lower side of the chamber have slots to provide good acoustical damping. The vortex generators are installed in the 200 mm front section (5a,c,e) or at locations nearer to the window (5b,d). The profile can be mounted between the windows downstream of the generators. The windows have a diameter of 230 mm and have interferometric quality. Instead of the windows a pressure measuring plate with an array of holes at 15 mm distance can be used. Up to 16 Kulite transducers can be digitized simultaneously. Thus accurate pressure field recordings can be made.

Two profiles are used for the investigations. They have a NACA 0012 shape and 120 mm respectively 60 mm cordlength. For the investigations they are placed between the windows at different angles of attack.

Different kinds of bluff bodies are used as vortex generators. Their wake is a Karman vortex street consisting of strong vortices of opposite sense of direction. The frequency of the vortices depends on the size and shape of the bluff body (a circular cylinder has a nearly constant Strouhal number of 0.2; i.e. the distance between vortices of equal sense of direction is 5 diameters). Several bluff body shapes were investigated, it turned out that a square cylinder has the highest amplitudes and best constance of Strouhal frequencies over the Reynolds number range from 0.1 up to 0.5 millions.

2.2. Shock Tube

Like other authors [2] we have used a shock tube to generate starting vortices. The shock tube consists of a high pressure section of 2100 mm length and a low pressure section of 3700 mm (fig. 6). The width of the tube is 100 mm and the height is 330 mm (fig. 7). The distance from the membrane to the measuring chamber divided by width and height of the tube give length to width and length to height ratios of 27 and 8.

The bottom and the top of the low pressure section are rounded with a diameter of 100 mm to prevent shock disturbances (fig. 7). The measuring chamber is the same as in the wind tunnel experiment (fig. 8). The same measuring devices can be used. The low pressure section is evacuated by the wind tun-

nel vacuum tank to a vacuum up to 100 mbar. The high pressure section is pressurized up to 1500 mbar. Pressure ratios from 1 up to 15 can be obtained.

Figure 8 shows the measuring chamber. A GOE 508 profile of 120 mm cordlength is mounted before the window area. The GOE 508 profile is a high lift profile with flat under side. It is mounted at an angle of 7.5 degree. Its stationary lift coefficient is 1.25. 5 mm of the trailing edge of the profile are visible in the viewing field. The 60 mm NACA 0012 profile is mounted 38 mm apart at the same height as the trailing edge of the asymmetric profile.

2.3. Computer Installation

The computer is a PDP 11/34. It has connections to the image processing computer, also a PDP 11/34, to the institute computer, a VAX, and to the central computer of Goettingen University and Max Planck Institute, a Univac 1108. Figure 3 shows the configuration of the PDP and the periphery [3].

On the right there are the data aquisition components. A Camac crate controller (CA11-FP, Digital Equipment) is the interface to 16 transient recorders (Le Croy) ,a real time clock and a digital I/O port. The transient recorders have 8 K storage capacity of 10 bit data at data aquisition rates up to 1 MHz. They are used to record the pressure data.

An IEC-bus interface is used to record the static pressure with the help of a digital voltmeter.

The third I/O component is the controller (LPA11-K, Digital Equipment) of a 12 bit analog/digital converter. Data rates up to 50 KHz can be stored directly on the disc.

The storage of measured data is performed with a 160 Megabyte disc (System Industries). Long term storage is done with a magtape.

Fast data processing is done with the array processor (Floating Point Systems). It is well suited for fast Fourier transforms, a FFT of 1024 points is done in 3 ms .

For visualisation of data there are graphic terminals (VT100 and Tektronix) and a hard copy unit, connected to the computer by a terminal multiplexer.

The interface to the fast data line to the image processing computer is a a DRU-11C (Digital Equipment). A DMC-11 is the interface to the data line to the VAX and Univac. The VAX is used for program development and other computing purposes. The Univac is needed for DISSPLA plots.

2.4. Optical Facility

A Zeiss Mach-Zehnder interferometer can be used for optical investigations (Fig. 2). The channel width is 100 mm . Vacuum in the measuring chamber corresponds to 48 whole fringes in interferograms. The light source is a high frequency spark light source. Movies can be made with a rotating drum camera at 10 Khz or with a Fastax camera at speeds up to 8 Khz .

3. Testing of the Experimental Arrangement

3.1. Vortex Street Generators

Vortex streets should be two-dimensional, should have a constant Strouhal number and must consist of strong potential vortices of the right spacing to be of use in our experiment. The interaction of vortices among themselves should be less than the interaction of profile and vortex. This means, that the quotient length/(2*Strouhal number), the spacing of the vortices, should be at least of the same magnitude as the profile length. The 40 mm cylinder has a Strouhalnumber of 0.2 and shows a vortex spacing of 40/(2*0.2)=100 mm . Although the aspect ratio of this cylinder is very small, the vortex street is quite stable and has only a single main frequency. Figure 9a shows the frequency at different pressure ratios. The Strouhal number is nearly constant but there is some influence of resonance of the duct geometry.

The 40 mm cylinder and the 120 mm profile were taken for the first vortex-profile interaction tests. Figure 9b shows the arrangement working with an even higher amplitude than the pure cylinder.

For tests with the 60 mm profile several bluff body shapes were investigated (Fig. 4). It turned out that a square cylinder has the highest amplitudes and best consistancy of Strouhal frequencies over the Reynolds number range. The 20 mm cylinder does not work as good as the bigger one, maybe because of a different aspect ratio.

3.2. Shock Tube

The shock tube setup uses the same measurement equipment as the duct. Especially the measuring chamber is the same. The length of the tube is 5800mm. It is sufficient to provide measuring times of 5 ms minimum for the Machnumber range from 0.2 to 0.8. The undisturbed trajectory length of the vortex is at least 400mm.

Because of the height of the chamber there are restrictions in the attainable length to height ratio of the tube. The length from the membrane to the windows is 2600 mm. Thus the length/height ratio is only 8. As interferograms proove this small ratio is enough to develop the shock. A problem is the rectangle geometry of the tube. The bursting of the rectangular membrane generates a circular wave. The reflections from the walls are oblique waves. These waves steepen up and form oblique shocks. To prevent theese disturbances it was tried to change the bursting process of the membrane by taking other materials and destroying the membrane by high voltage. But this did not work very well and it was found out, that round shapes of the top and the bottom of the tube prevent uniform reflections of the oblique disturbances.

4. Computer-Based Interferogram Evaluation

4.1. Digitizing and Preprocessing

The interferograms are photographically recorded on film by taking single frames or taking series of interferograms on 16mm film using high speed pickup-techniques as described previously. The digitizing of these interferograms is done by a TV-digitizer, connected to a mini-computer. The resolution is selectable by choice of the scan frequency and the line spacing. Usually a resolution of 512 by 256 points (256 intensity levels) is used, but also 512 by 512 points or even 1024 by 512 points could be achieved. The system further is equipped with a digitizing tablet and a graphic terminal to enable hand input of graphic data. Also, a computer-controlled film projector is used to digitize consecutive frames of a series of interferograms. A detailed description of the system is given in [3,4]. The digitized TV-lines are fed to the computer and are processed sequentially or stored on disk for subsequent processing. Depending on the quality of the interferograms different enhancement procedures can be used to increase the signal-to-noise ratio, correct an uneven illumination or increase the contrast of the fringes.

4.2. Fringe segmentation

The fringe segmentation is performed in two steps. First the gray level fringes are converted to binary levels by using a fixed or floating threshold. In the next step the left- and right-edge points of the fringes are collected and stored in a polygonal data structure using a sequential tracking algorithm. To reduce the amount of data to store, a redundancy re-

duction process approximates the actual polygon by a subset of the vertices of the original polygon within a given range of tolerance.

If fringes leave the field of view, or if a background object resides inside the fringe field (e.g., an airfoil), the visible area of the fringes can be handled by using the points on the boundary as edge points of the fringes. The corresponding polygons of course may not be along the boundary of the background object, since they may have different fringe orders. In order to establish the boundary test in a quick, easy and robust manner, it is not desirable to derive the boundary information from the fringe field itself. Instead, the geometry of the test section is used to generate a binary-valued mask, which is compared pixel by pixel with the actual interferogram, while performing the fringe extraction process.

At some locations in the fringe fields the fringe spacing may be very small, as is the case for instance inside the boundary layer, inside a shock wave or near separation lines. If the resolution of the digital system is exceeded at these locations, disconnected or falsely connected fringes may occur. This results in the fact that some of the polygon segments, representing different fringe orders, may be linked together. In order to improve the numbering process, most of the disconnections could be removed by an analysis of some geometrical parameters of the polygons. These geometrical parameters are the shape feature (the circularity defined by the enclosed area divided by the perimeter squared), the ratio of the distance of the polygon endpoints to the length of the polygon line, and the angles between the polygon segments.

Those lines which are suspected to have disconnections are cut by this process at locations where the polygon is folded or where it has sharp edges. The remaining polygons having dis-

connections not detected by this cutting process have to be handled by the numbering process.

Some consideration and programming work has been done on the problem of getting numbers for the fringe lines of an interference fringe field by using the known numbers of a similar fringe field. The matter is somewhat more complicated, as some of the lines of the actual fringe field may have disconnetions, and therefore it may be impossible to get a unique fringe number for that line.

The idea of a numbering scheme applicable to series of interferograms is to get additional information from the previously numbered fringe field. This may only be possible if the fringe locations vary only a small fraction of the fringe spacing at almost any locations of the test section. If the interframe time between consecutive interferograms is choosen appropriately, this condition is satisfied in the case of the profile flow investigation. The numbering of a series of interferograms starts with the setting of the numbers of the first fringe field by hand. The fringe lines are superimposed by a set of so called test-lines at which a set of order number functions is defined by a rational spline approximation. This set of spline functions is fitted to the fringe lines of the next following interferogram. The numbers of those fringes overlapping uniquely at the test-lines are accepted directly, the other numbers are derived from the spline functions. An older version of the program uses a set of straight lines running in the x- and y-direction, while a newer version, currently under development, uses a set of polygons as test-lines. The advantage of the polygonal test-lines is that they are more suitably adaptable to the global course of the fringe lines.

In the case where some disconnected lines remained from the

preprocessing step these lines may not receive a unique number by the numbering scheme. To decide where these lines have to be divided into two or more segments - an older version of the program uses the angles between subsequent polygon segments - the deviations from a local approximation of the fringe order function is used. Another advantage of comparing fringe fields by using local polynomial approximations is the fact that fringe polygons, having no intersections with the test-lines, could be processed with the same algorithm, leading to a more stable behaviour of this numbering process.

4.3. Polynomial Approximation

The fringe order function is defined at a set of contour lines, but most of the mathematical transformations to follow require the interpolation of fractional fringe order numbers. Some methods to interpolate between randomly scattered points on a surface are discussed in the literature [6]. We used a local distance weighted polynomial least squares approximation, best suited in regard to computation time and numerical representation. This process computes the coefficients of two-dimensional polynomials of second order at the meshpoints of a rectangular grid. To calculate the interference order inside the meshes, the four polynomials at adjacent corners of the mesh are evaluated and weighted proportional to their distance to the point of interest.

Another method is to compute a two-dimensional spline approximation, using some of the previously computed polynomial coefficients, to get a smooth surface having continuous first and second derivatives. The density function may easily be computed by a linear transformation of the fringe order values, because in the actual experimental set-up the fringes are lines of constant density (infinite fringe case). In the case of finite fringe fields a subtraction of the overlayed fringe

pattern could be achieved by a modification of some of the polynomial coefficients.

4.4. Localization of The Vortex Core

In the current study of the vortex-profile interaction process a point of interest is the knowledge of the vortex traces under different positions of the profile, to see if a theoretical description of these traces is in accordance with experimantal results. Some program development has been done to localize the typical fringe pattern resulting from the appearance of the vortex. The vortex core is computed using the centroid of the enclosed area of the innermost of these fringe lines.

5. Experimental Results of Vortex Street-Profile Interaction

5.1. Pressure Fields

Measurements were performed with the 40 mm cylinder with and without the 120 mm profile. The pressure ratio range was from 0.999 to 0.6, that is from 13 m/s to 290 m/s .

As expected, the pressure field is antisymmetric, when vortex generator and profile are aligned in the cordplane. The difference from antisymmetry is less than 5 degrees phase angle in Fourier spectra. Therefore it is sufficient to have pressure transducers only in the upper half of the measuring chamber.

Figure 5a shows the pressure transducer positions used in the measurements which are described in this report. Figure 9 is done with pressure transducer 5. Figure 10a and b are typical examples of pressure recordings. At a pressure ratio of 0.83 transducer 2 measures an underpressure of more than 200 mbar . The vortices differ in strength and do not have the same path, so the extreme underpressure peaks only happen from time to time. There is a diffusion of vortex strength and the peaks at transducers 8,10 and 12 do not have such high amplitudes anymore. Signals at transducers 5,6,7 and 9 (above profile) do not have single peaks anymore but a more sinoidal shape.

Depending on resonance the peaks of frequency recordings are more or less sharp. But there is always a Strouhal frequency

far above the wall turbulence level at nearly all measuring points. Figures 11 to 14 are typical examples of spectra. The spectra are done with 0.8 s long pressure recordings at 10 Khz sample frequency.

At the same pressure ratios vortex street and profile vortex interaction have the same Strouhal frequency. The vortex generation process seems to be not influenced by the profile. The profile measurements show only a slightly better consistancy of Strouhal frequency. The amplitudes in the vicinity of the cylinder are of the same order of magnitude. The amplitudes measured above the profile (transducers 3,5,6,7,9) are greater in the profile case. At any pressure ratio the phase differences between the measuring points are entirely different. The hydrodynamic field as well as the sound field are influenced strongly by the profile.

The first pair of spectra (Fig. 11) is done at the high pressure ratio of 0.998. The velocity is about 19 m/s . The sound generation is inefficient at low velocities. The pressure field is a relatively undisturbed hydrodynamic field. The Strouhal frequency is of the same magnitude, but the vortex street signals are more noisy. Very obvious is the difference at transducer 1. Only transducer 8 of the profile case shows a noisy character, because it is influenced by the profile wake. It is interesting that the phase differences between the same transducer pairs are entirely different even in the pure hydrodynamic case.

The second pair (Fig. 12) has a sharp dominant frequency with the profile and several frequencies with the vortex street, due to beats and frequency jumps. Figure 13 is an opposite example. The vortex street shows the more narrow frequency band, whereas the profile has got a large number of different Strouhal frequencies. Surprisingly there is the same dominant

frequency at all measuring points.

Figure 14 is a resonance case with extremly high amplitudes. There is the same frequency at all measuring points and nearly the same frequency in both plots (The first harmonic has a higher amplitude at transducer 1 and 8, but the fundamental is the same). In both cases highest amplitudes are at transducers 2 and 3. The transducers above the profile 3,5,6,7,9 have higher amplitudes with the profile. The greatest difference is in the first harmonic (Fig. 15). There is a harmonic at transducers 1,2,3 in both cases, but the profile shows higher amplitudes and higher quality factor. Entirely different are the transducers above the profile (5,6,7,9) where the vortex street shows noise and the profile shows the first harmonic with high amplitudes and high quality factor. This might be a hint that a new phenomenon is ocurring with strong vortices at high Reynolds numbers.

5.2 Evaluation of interferograms

5.2.1 Automatic Evaluation

As an example of the digital interferogram analysis two processed fringe fields of a profile flow with and without a vortex present are shown in Figures 16a and 17a. The flow velocities are 280 m/s respectively 100 m/s at an angle of attack at 0 degrees. The interferograms where digitized with a resolution of 512 by 256 pixels. The fringe extraction process described in chapter 2.4 was used to obtain the polygonal

fringe fields shown in Figures 16b and 17b. The boundaries of the test-section as well as the airfoil are input by hand, using the digitizing tablet. These lines are used to prepare a mask file, needed by the fringe extraction program to avoid connections of fringe lines along the boundaries of background objects. Due to the restricted resolution of the digital system there appeared some falsely connected lines around the leading edge of the airfoil, where the fringe spacing is very small. These locations could be detected and the falsely connected lines could be cut by application of the aforementioned algorithm, using the geometrical parameters of the lines.

The lines are numbered corresponding to the interference order, which in this case is done by hand, because the automatic numbering algorithm, applicable to these types of fringe fields, needs a numbered field to start the numbering process of consecutive frames. The density function was derived from the fringe field by approximation of polynomials of second order at the mesh points of a rectangular grid (shown in Figs. 16b and 17b) as decribed in chapter 4. To achieve a smooth surface, the interference order function was calculated from these polynoms by use of a bicubic spline interpolation procedure. Two density profiles in x-direction at y = 0.2 are plotted in Figs. 16c and 17c. The realtive density as a function of the fringe order is given in this case as

$$\varrho/\varrho_0 = 1 - \frac{1}{n_0(T_E, p_E) - 1} \frac{p_E}{T_E} \frac{T_0}{p_0} \frac{\lambda}{h} \frac{N(x,y)}{2}$$

where o/o is the relative density, n (T ,p) is the refractive index of air at temperature T and pressure p , T and p are the temperature and pressure at rest, is the wavelength of light, h the depth of the test chamber and N(x,y) the fringe number function. Note, that the number function is di-

vided by two, because each fringe is represented by two lines (a "left" and a "right" one). The above equation, evaluated with the actual dimensions valid in the tests, yields

$$\rho/\rho_0 = 1 - 0.01058 * N(x,y).$$

As can be obtained from Fig. 17, the lowest density appears inside the vortex core with a value of 0.92 relative to the density at the stagnation point, where the fringe number was set equal to zero.

5.2.2 Four Kinds of Phenomena

Figures 18 - 24 are high speed movies of vortex streets without (18) or with a profile (19 - 24). The frame rates are 6.25, 6.3, 6.35, 6.35, 6.15, 6.4 and 6.3 khz. The high speed camera is a Fastax movie camera. A collection of instructive and typical sequences out of the longer movies is shown in the figures.

When a vortex of counter clockwise circulation approaches a profile the direction of the velocity at the profile is upwards. The profile generates lift. The lift is increasing as long as the vortex is approaching. It is decreasing after the vortex has passed the center of the profile. Then the velocity is directed downwards. When the vortex has a high dimensionless circulation

$$\Gamma_{dl} = \frac{\Gamma_{vortex}}{\pi * v_{\infty} * cordlength}$$

this sudden change of velocity direction is connected with the generation of a secondary vortex at the leading edge of the

profile. We call this effect the generation of the 'suction peak vortex', because in the interferograms the secondary vortex is the detached suction peak.

The changes of lift of the profile are connected with a starting vortex. But not every vortex of the vortex street generates a starting vortex at the trailing edge of the profile and the starting vortices differ very much in their circulation.

When a weak vortex gets close to the boundary of the profile there is a local separation at the vortex. Depending on the sense of direction the separation is in front or behind the vortex.

The vortex looses a lot or even most of its circulation when the interaction with the profile is connected with strong separations.

So there are four kinds of interaction phenomena:
1. : Suction peak vortex
2. : Starting vortex
3. : Local separation
4. : Loss of circulation

5.2.3 Strong Vortices

Figures 19 - 22 show the profile interaction of vortices of high dimensionless circulation. The trajectorial velocities of the vortices in the wake of the cylinder are slower than the flow velocity far away. The measured trajectorial velocities and circulations are averaged out of hundred pictures.

The circulation is calculated with the density of the three outer fringes of the vortices. The standard deviation is 10 per cent for the velocity and 15 per cent for the circulation. The value for the circulation is measured only for circular vortices and not for turbulent spots. The dimensionless circulation is calculated with the trajectorial velocity.

The undisturbed vortex street is to be seen in figure 18. Not every vortex is circular, but the majority of the vortices has a shape comparable to the vortex in figure 18a. The vortices of the undisturbed street are close to the center line with individual deviations. A classical Karman spacing cannot be found.

There are three different kinds of suction peak separation. In any case the incoming strong vortex induces a big suction peak at the leading edge of the profile which is the source for a secondary vortex. Depending on the position of the profile to the vortex street centerline a vortex can pass on the lower or upper side of the profile, i.e. it can pass on the suction or on the pressure side of the profile. In each case the suction peak detaches and forms a vortex on the suction side of the profile. So there are two vortices on one side in the first case and two vortices divided by the profile in the second case. When the vortex core gets very close to the leading edge an interesting third case is happening. When the core reaches the suction side it combines with the detaching suction peak. There is only one very stable vortex left then.

In figure 19 the profile is aligned with the center of the square cylinder. The profile is mounted in the rear end of the measuring area. The trajectory of the approaching vortices is to be seen. The vortex cores stay very close to the center line and get very close to the leading edge of the profile. Figure 19b shows an approaching counter clockwise vor-

tex that is kind of cut by the profile. The core gets to the lower side of the profile. When the core passes the leading edge the suction peak grows, detaches and gets a secondary vortex. This secondary vortex is not very stable (19c). The next vortex rotates clockwise and induces negative lift. Its position is in line with the profile. By the mirror vortex force it is driven under the profile. It combines with the detaching suction peak. A new very stable vortex is formed (19d).

Figure 20 is an interferogram of a similar configuration as figure 19, but the profile is mounted in the center of the measuring area and the velocity is lower. Figure 20 shows two vortices passing the profile on the pressure side as it is expected in a regular Karman street. On the suction side of the profile there is again a suction peak vortex.

In Figure 21 the profile is aligned with the upper edge of the square cylinder. Most of the vortices are passing under the profile. Again there is the detaching suction peak on the upper side which itself induces a secondary vortex in front of it.

Figure 22 is an interferogram of a configuration where the profile is mounted 35mm above the center of the square cylinder. In figure 22a a clockwise vortex is approaching the profile. In the second picture of figure 22b there is the core of the vortex below the suction peak. Together they form a turbulent spot (22d). In figure 22b a strong starting vortex is produced. We do not know exactly the conditions for a generation of a starting vortex. The strenghts of the starting vortices differ very much and it is not easy to find a law. But it seems to be, that the generation of a starting vortex is not only depending from the circulation fluctuation of the global flow but also on the local conditions at the

trailing edge, i.e. the vicinity of a vortex to the trailing edge.

5.2.4 Weak Vortices

Vortices of high dimensionless circulation induce global effects on the profile flow, i.e. separation on the opposite side, starting vortices e.t.c., whereas weak vortices induce local effects , i.e. separations near the vortex.

Figure 23 is a view on the whole configuration of vortex generator and profile. They are more close together than in the other figures to have a view on the whole mechanism. The dimensionless circulation is in between the strong vortex case and the weak vortex case of figure 24. Although the square cylinder is only half as big the circulation of the vortices is quite high because of the short distance of the profile from the vortex generator. The interferograms show the generation of the vortices at the square cylinder and flow phenomena that are very close to the strong vortex case, i.e. suction peak vortex and starting vortex.

Figure 24 is a weak vortex case. In this case there are separations only only in the neighbourhood of the vortex. The sense of direction of the vortices is clockwise on the upper side and counter clockwise on the lower side of the profile. Behind the vortex, on its left side , there is a separation from the profile boundary which can become a vortex itself as in the last pictures of figure 24d. With the opposite sense of direction the vortex induces a secondary vortex on its frontside (figure 27c 1).

The local separation at the profile boundary is always at that side of the vortex where the flow direction is away from the profile.

6. Single Vortex Trajectories

6.1 Free Vortices

Experiments at three different pressure ratios were performed in the shock tube. Pressure ratios of 1.8, 3.4 and 7.0 give uniform velocities of Machnumber 0.2, 0.4, and 0.6 behind the shock. The shock Machnumber is 1.13, 1.29 and 1.50. Figures 25 and 26 show free vortices at Machnumbers 0.2 and 0.6. On the left side in the pictures there is a little tip, the trailing edge of the vortex generating profile. In Figure 25 there is a vortex travelling from the left (fig. 25a) to the right hand side (fig. 25b) at Machnumber 0.2. It is loosing about 30 per cent of its circulation on its way through the measuring area. In figure 26 there is a vortex at Machnumber 0.6 in the middle of the measuring area. Its circulation remains fairly constant throughout the measuring area.

Figure 28 is a drawing of measured vortex trajectories. There is no difference in vortex trajectories for different Machnumbers within the measuring uncertainty of 1 mm. The free vortex trajectory for the Machnumbers 0.2,0.4 and 0.6 is the black line in figure 28. The first 5 mm of vortex life is the generating period. The growing of the vortex is self similar. The trajectory starts at the trailing edge at an angle 35 de-

grees to the direction of the shock normal and seems to be straight. 5 mm apart from the edge the trajectory becomes curved and 35 mm away it is a straight horizontal line with uniform velocity.

6.2 Vortex-Profile Interaction

Figure 27 , taken at a frame rate of 6 khz with the rotating drum camera, shows a vortex passing a 0012 profile. In the under left side there is the trailing edge of the vortex generating profile. In the middle of the picture , 38 mm apart from the trailing edge, there is the 60 mm NACA 0012 profile. The gray spots are holes in the window for mounting other profiles.

The first picture is just before the shock arrives(fig. 27a). In the second picture there is the main shock and reflected circular waves. The main shock is divided in two parts by the vortex generating profile. The upper part is slower than the lower part. The difference gives rise to the generation of the vortex. The oblique shock in picture 3 is a disturbance of the main shock. The generated vortex has a dimensionless circulation

$$\Gamma_{dl} \approx \frac{\Gamma_{vortex}}{\pi \times v_{\infty} \times \text{cordlength}} = 0.12$$

The dimensionless height of the free vortex trajectory above the cordline is

$$h_{dl} \approx \frac{2 \times \text{height}}{\text{cordlength}} = 0.23$$

The vortex has a strong influence on the stagnation point and the boundary layer of the profile. While the vortex is appro-

aching the profile, the flow at the leading edge gets faster and the stagnation point is going more to the lower side. When the vortex has passed the leading edge the stagnation point moves upwards to its stationary point which is caused by the circulation of the asymmetric profile.

35mm away from the trailing edge of the vortex generating profile the vortex trajectories without another profile are straight. With a profile the vortex tends to go more upwards. This is caused by the thickness of the profile and the mirror vortex force. At the center of the profile the vortex trajectory is more parallel to the cordline of the profile. When the vortex passes the trailing edge of the profile it goes upwards again.

To evaluate vortex traces and sound generation a simple model of profile-vortex interaction is used. It consists of potential theory and is evaluated by conformal mapping. A potential vortex passes a Joukowsky profile of a 0012 like shape. Compressibility, boundary layer effects and the Kutta condition are not included. The sound generation can be evaluated by matched asymptotic expansions [9,10,11,12,13]. The result of the first order is a dipol-like field.

The model is compared to the experiment. Figure 28 shows a comparison of measured and calculated vortex trajectories. When the experimental vortex has finished its trailing edge caused upward movement it has nearly the same trajectory as the theoretical vortex of the same dimensionless circulation until it reaches the center of the profile. The experimental trajectory at the trailing edge is entirely different from the calculated one. This seems to be due to the neglection of the Kutta condition. Calculations with Kutta condition [14] give results that are closer to the experiment.

Figure 29 shows the experiment in comparison to the calculations of Parthasarathy [14]. He has calculated vortex-profile interaction with a flat plate and 13 per cent thick Joukowsky profile (trailing edge angle 0 degree). The parameter range of the calculation is different from the experiment, the dimensionless circulation is 0.5 and the dimensionless height is 1, but the quotient of circulation and height - which is a criterion for the interaction strength - is the same as in the experiment. Thus there should be a qualitative similarity of calculation and experiment.

The calculated vortex trajectory for the flat plate case and the measured vortex trajectory for the NACA 0012 profile are nearly parallel lines (fig. 29), whereas the trajectory for the Joukowsky profile looks entirely different. The strong S-shape trajectory of the vortex in the Joukowsky profile case can not be found in the experiment. Even the flat plate calculation shows a stronger S-shape trajectory than the experiment.

The similarity of flat plate calculation and experiment is obvious and a comparison of the calculation with an experiment of the same parameters will be interesting.

7. Some Concluding Remarks for The Profile Experiments

Vortices have a strong influence on profile flow and vice versa. Depending on the circulation of the vortex different separation effects occur. Vortices of high dimensionless circulation induce global changes of profile flow. Every dimensionless circulation that is investigated induces at least local seperations. The vortex looses a lot or even most of its circulation. It is doughtful if the assumption of an interaction of a profile and a vortex of constant circulation can describe the reality.

Improved models of profile-vortex interaction can be compared quantitatively with the shock tube experiment, which will show interesting results.

6. References

[1] Meier, G.E.A.: Ein instationaeres Verhalten transsonischer Stroemungen. Mitteilungen aus dem MPI fuer Stroemungsforschung und der AVA, 1974, Nr. 59.

[2] Dosanjh, D. S., Weeks, T. M.: Interaction of a Starting Vortex as well as vortex street with a Travelling Shock Wave. AIAA Journ. 3 (1965) p. 216

[3] Rehberg, I.: Eine stroemungsakustische Spitzenkatastrophe. Mitteilungen aus dem MPI fuer Stroemungsforschung und der AVA, 1983, Nr. 75.

[4] Ziada, S. and Rockwell, D.: Vortex-leading-edge interaction. J.Fluid.Mech.(1982),vol. 118, pp. 79-107.

[5] Tang, Y.-P. and Rockwell, D.: Instantaneous pressure fields at a corner associated with vortex impingment. J.Fluid.Mech.(1983), vol. 126, pp. 187-204.

[6] Obermeier, F.: On a New Representation of Aeroacoustic Source Distribution. I General Theory. Acustica 1979/42, pp. 56-61.

[7] Obermeier, F.: On a New Representation of Aeroacoustic Source Distribution. II Two-dimensional flows. Acustica 1979/42, pp. 62-71.

[8] Moehring, W.: On Sound Waves in Shear Flow. Max-Planck-Institut fuer Stroemungsforschung, Bericht 111/1976.

[9] Obermeier, F.: The application of Singular Perturbation Methods to Aerodynamic Sound Generation. Lecture Notes in Mathematics. Vol. 594, Springer Verlag (1977), pp. 400-421

[10] Obermeier, F.: Zur aerodynamischen Schallerzeugung wirbelbehafteter Stroemungen in der Umgebung starrer Koerper. Max-Planck-Institut fuer Stroemungsforschung, Bericht 106/1978.

[11] Parthasarathy, R.: Aerodynamic Sound Generation Due To Vortex-Aerofoil Interaction. Dissertation Stanford University September 1972

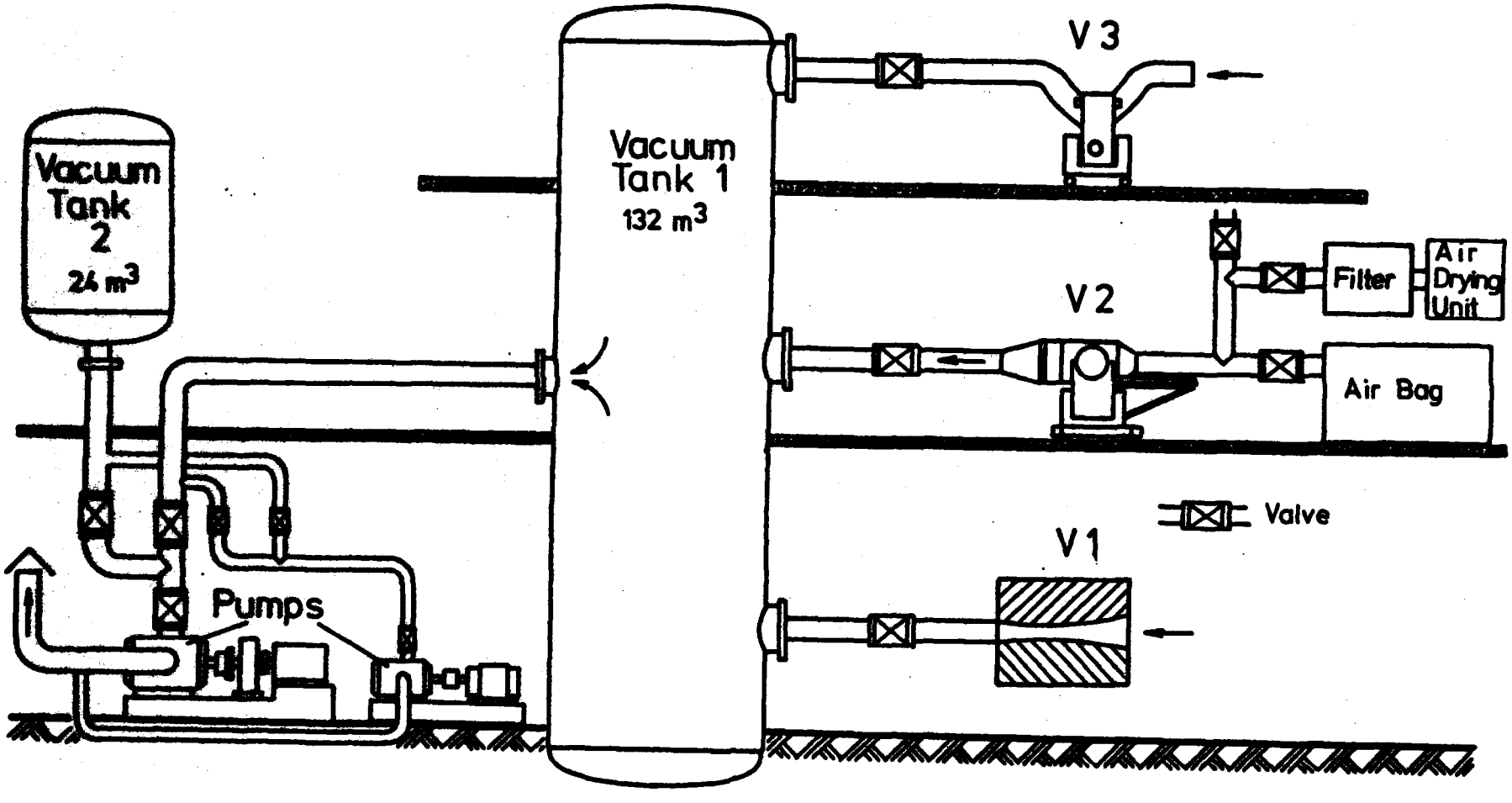

Figure 1: The transonic duct. Experiments are carried out at facility V2.

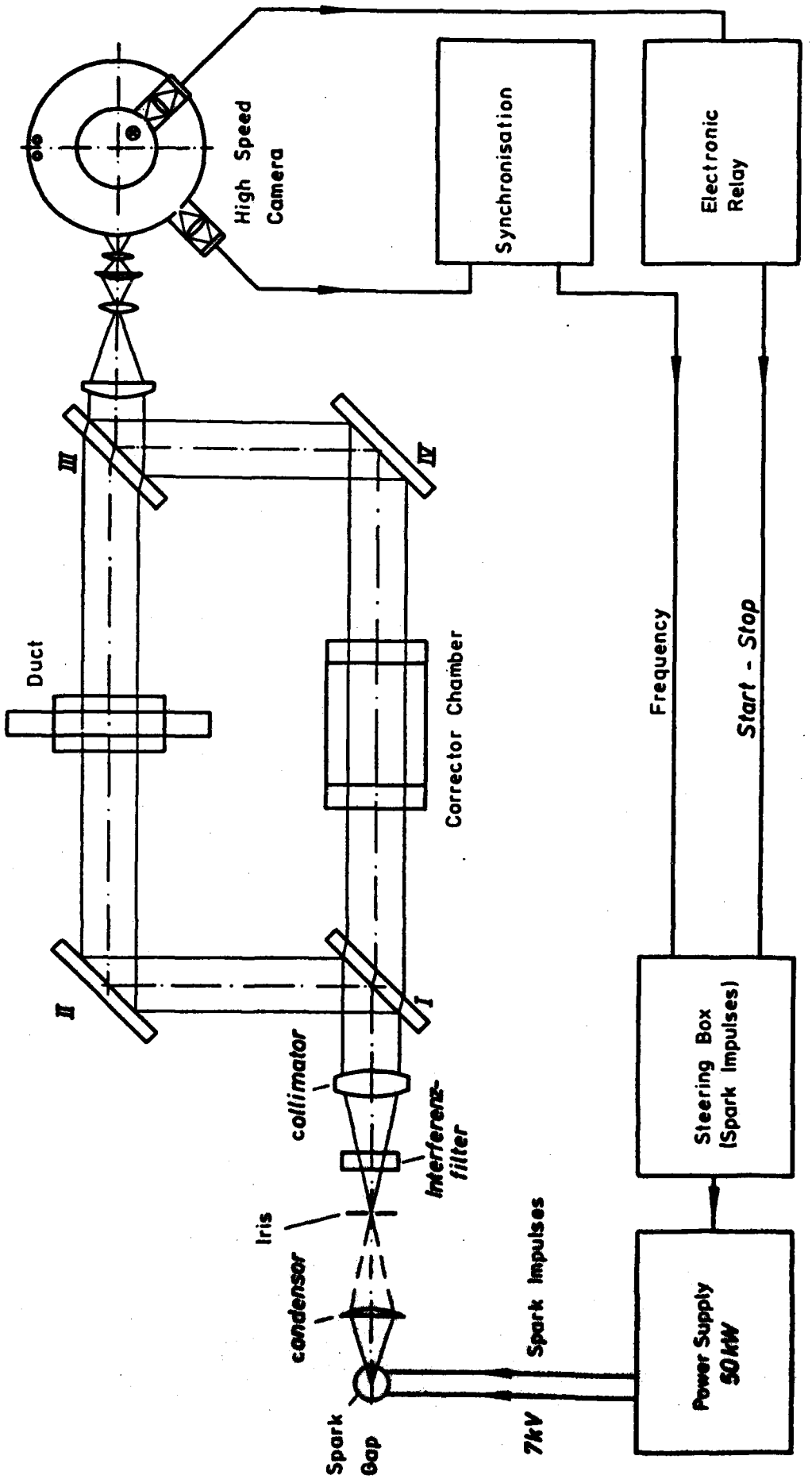

Figure 2: Optical facility for high speed interferogram movies.

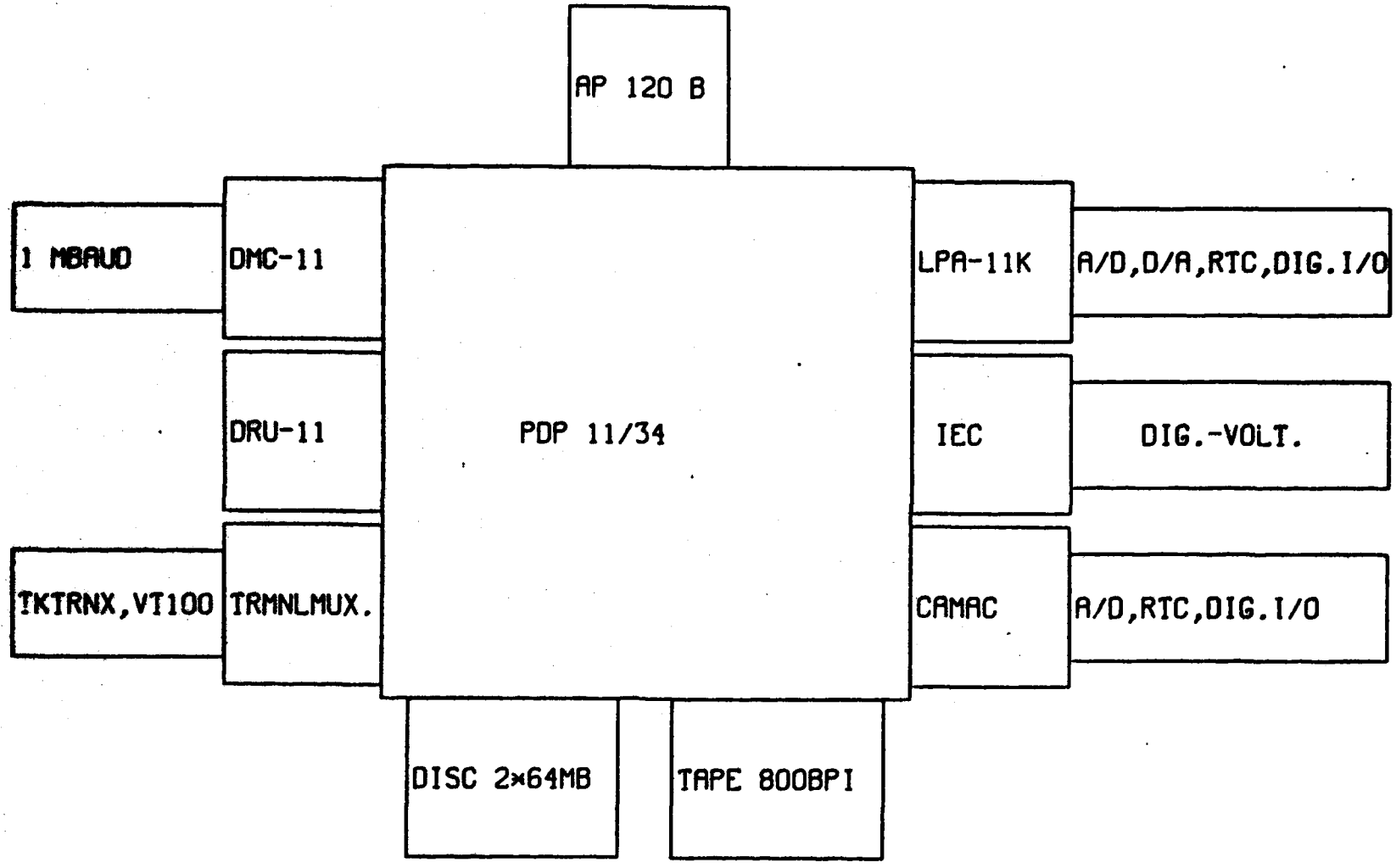

Figure 3: Computer installation.

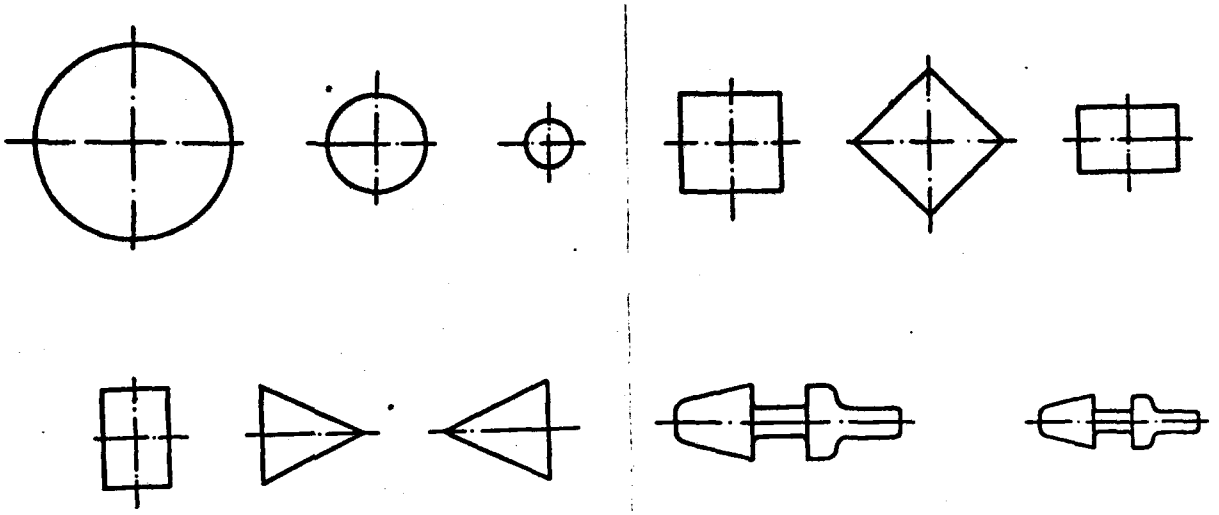

Figure 4: Bluff body vortex generators:
Circular cylinders of 40, 20 and 10 mm diameter, square, rectangle and triangle cylinders of 20 mm width and a special shape, that is used in vortex flow meters.

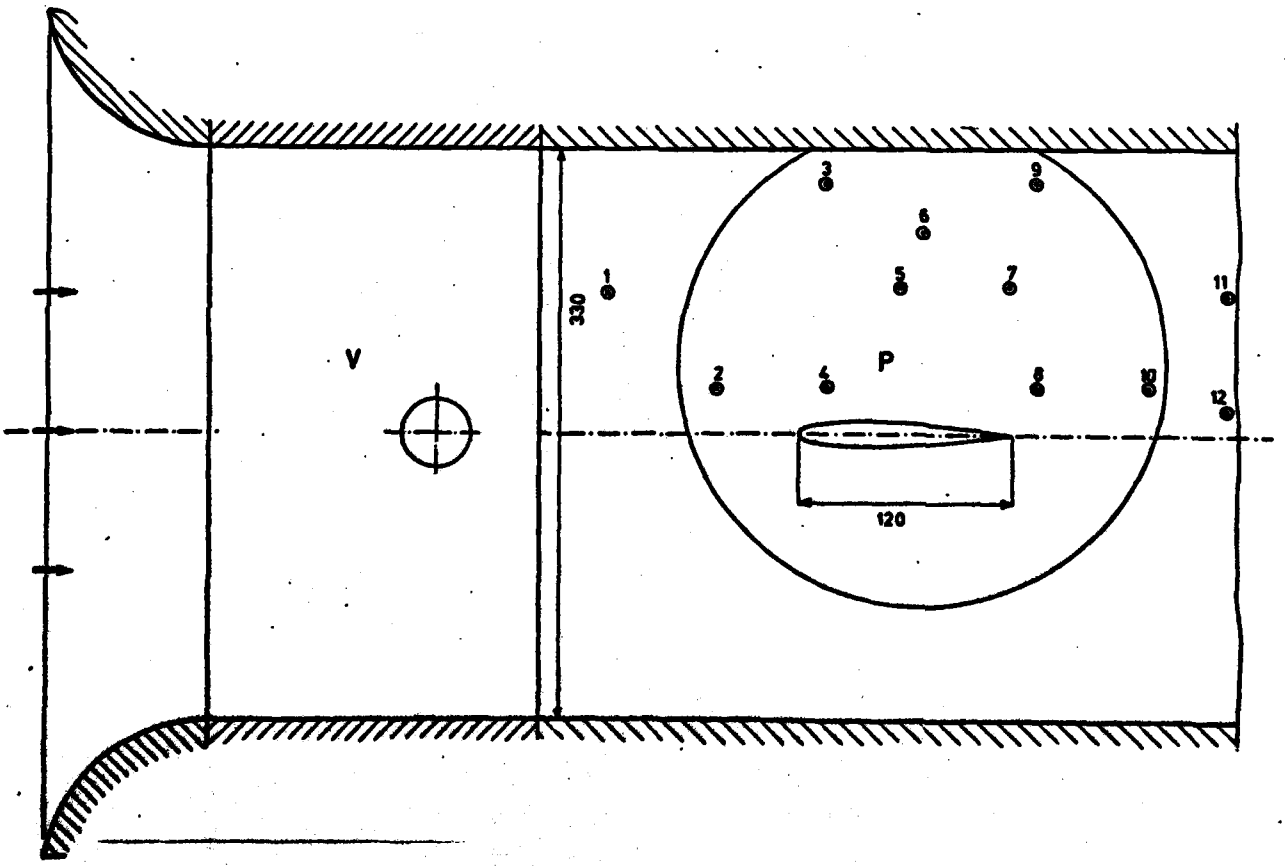

Figure 5a: Measuring chamber for vortex street - profile experiments. Points 1 - 12 are transducer positions.

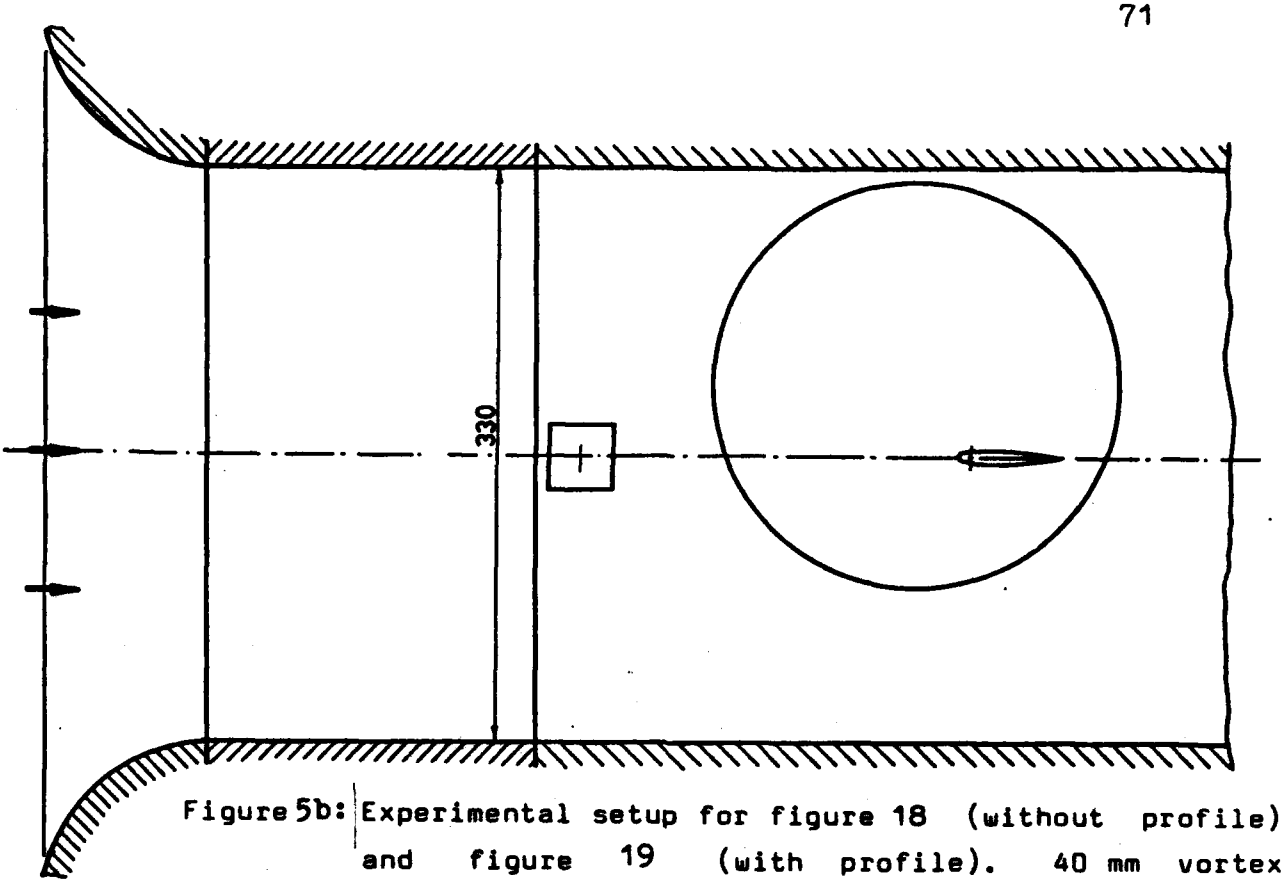

Figure 5b: Experimental setup for figure 18 (without profile) and figure 19 (with profile). 40 mm vortex generator and 60 mm profile.

Figure 5c: Experimental setup for figure 20,21 and 22. 40 mm vortex generator and 60 mm profile. The vortex generator is mounted in line with the profile (20), 20 mm and 35 mm under the profile (21,22) .

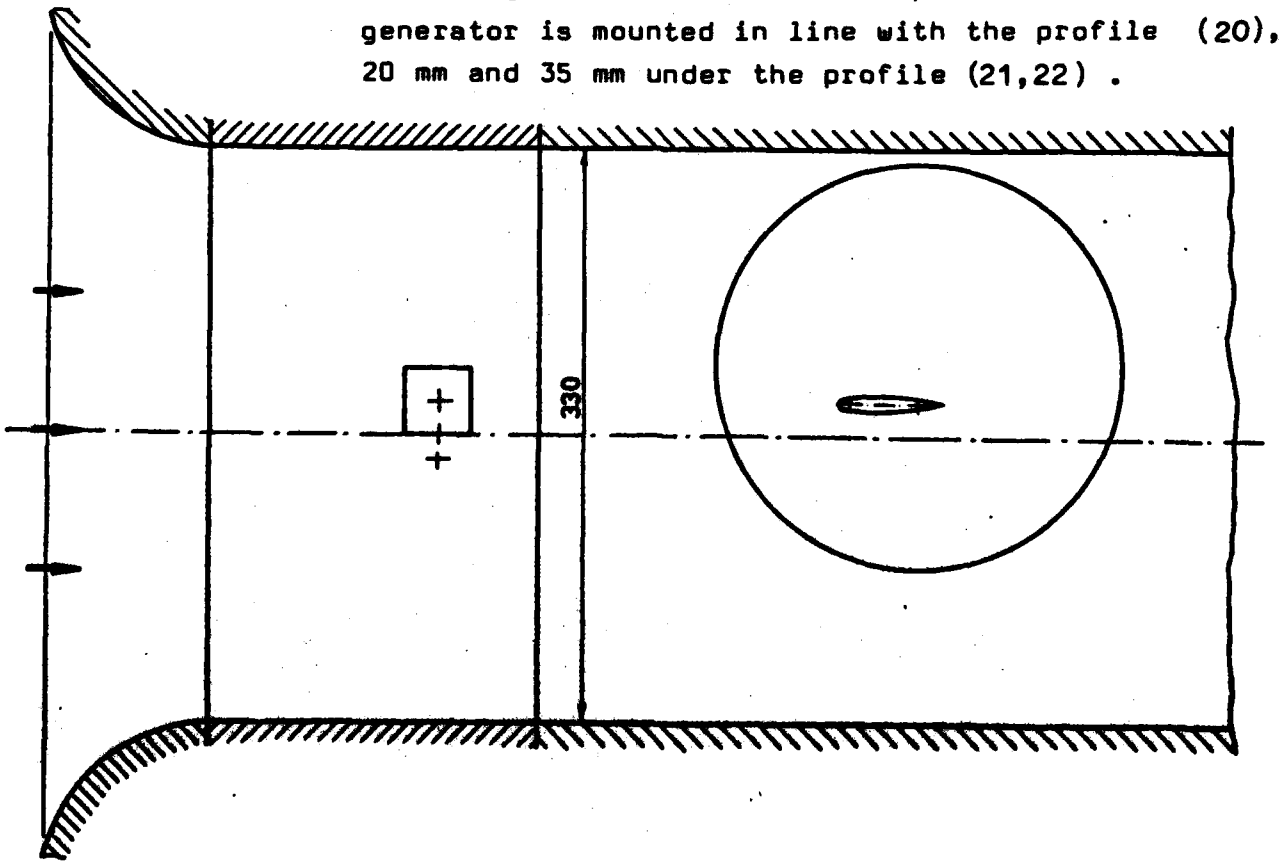

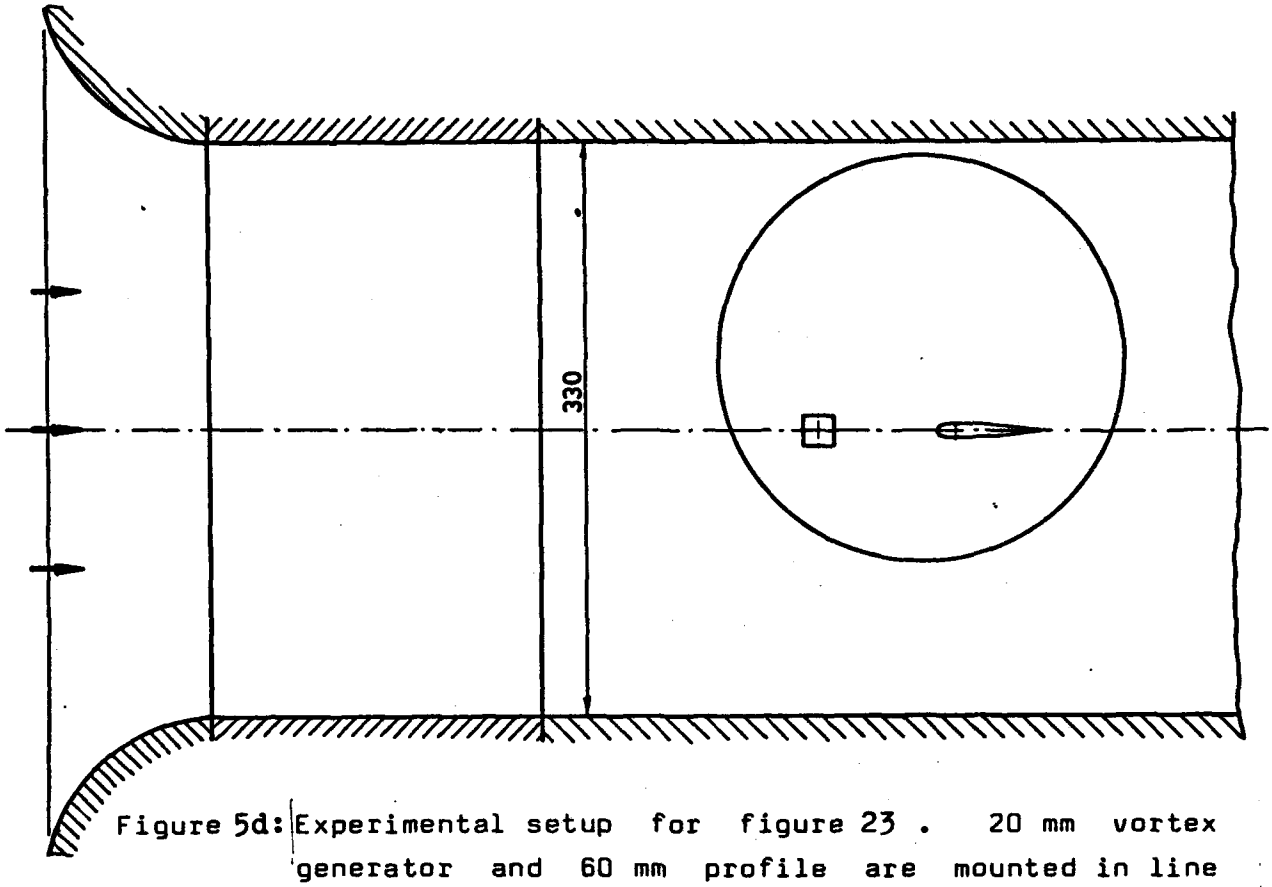

Figure 5d: Experimental setup for figure 23 . 20 mm vortex generator and 60 mm profile are mounted in line in the window area.

Figure 5e: Experimental setup for figure 24 . 20 mm vortex generator and 120 mm profile.

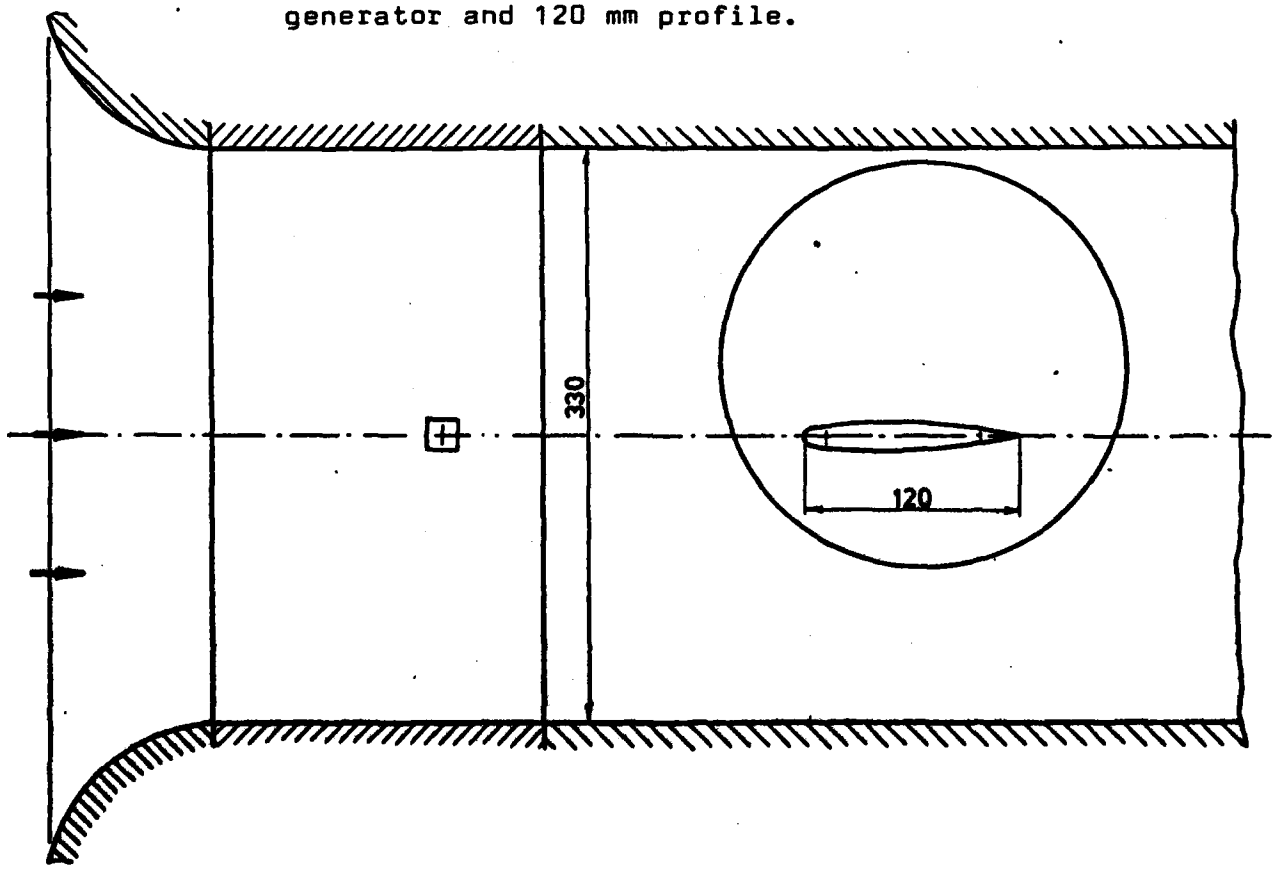

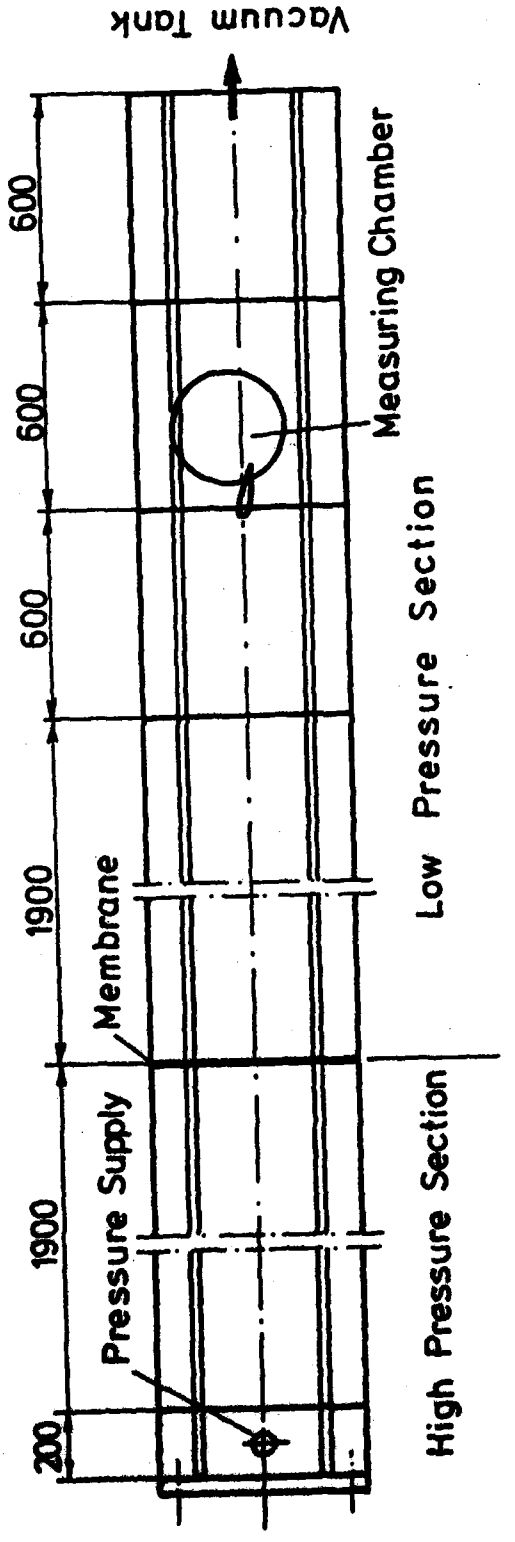

Figure 6: Side view of the shock tube.

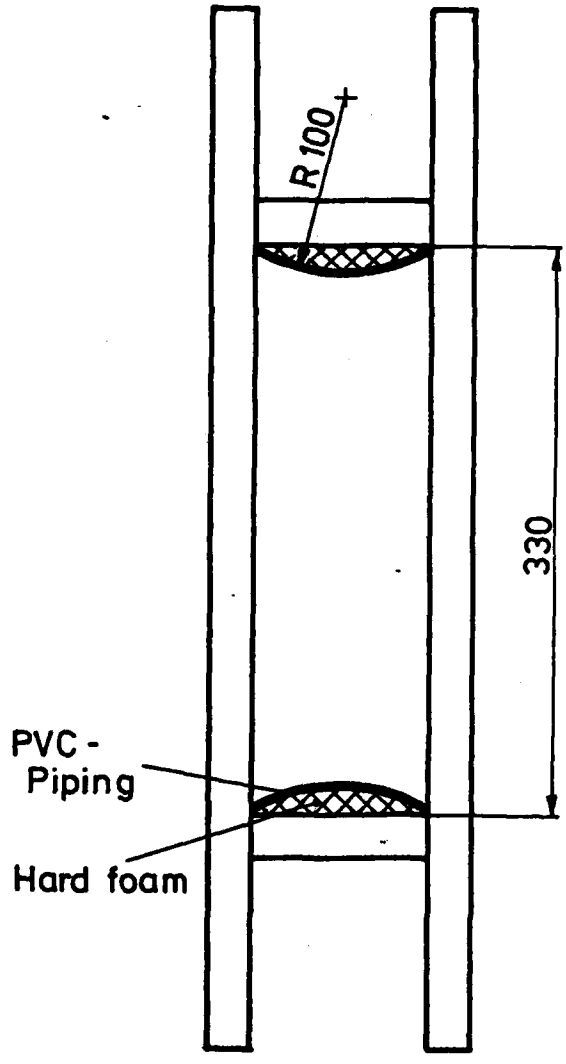

Figure 7: Front view of the shock tube. The bottom and the top of the tube are round to prevent shock disturbances.

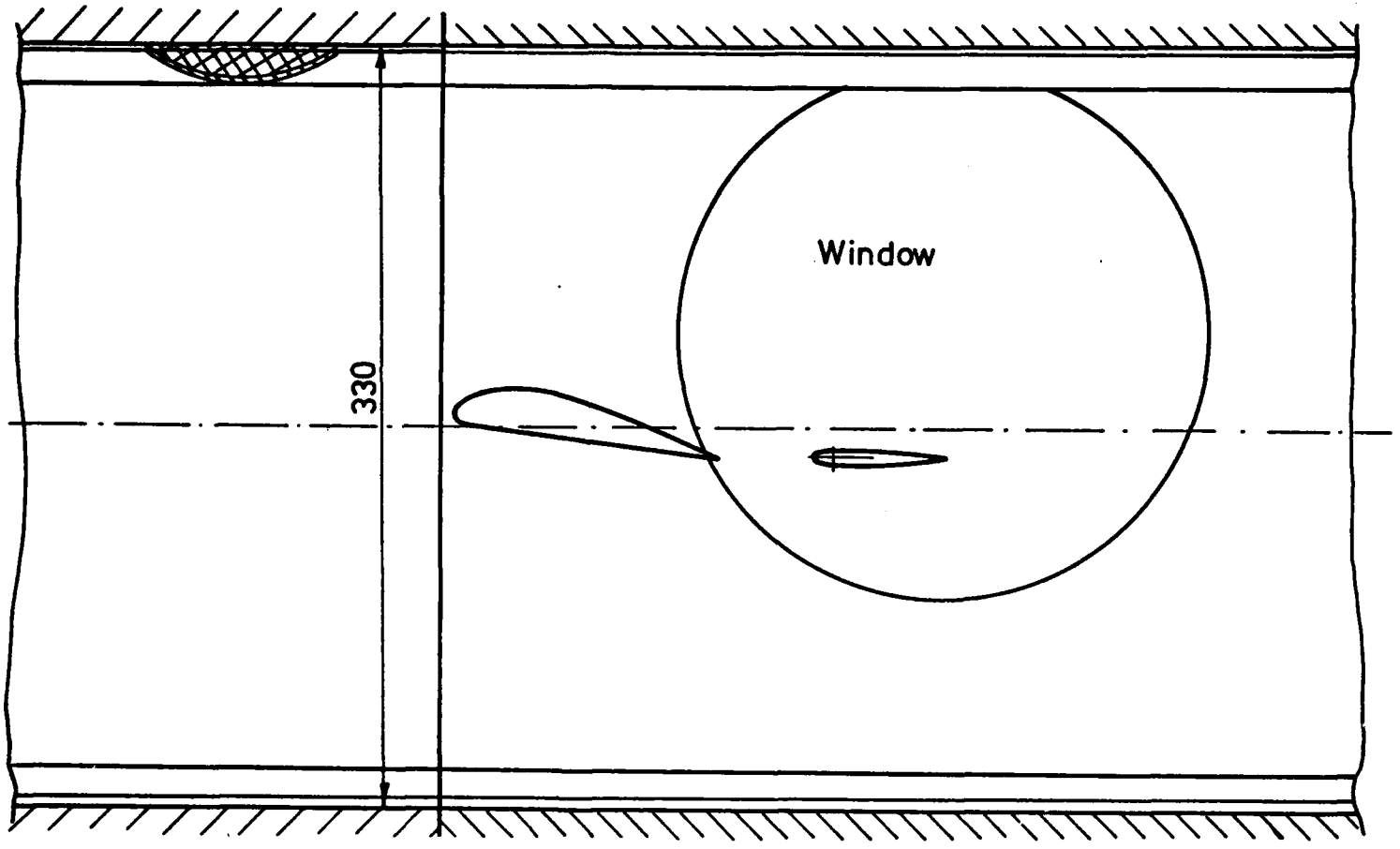

Figure 8: Measuring chamber of the shock tube. A 120 mm GOE 508 profile is mounted at an angle of 7.5 degree. A 60 mm NACA 0012 is mounted in line with the trailing edge.

Figure 9: Fourier spectra at different pressure ratios.

9a: Vortex street
Transducer 5 Maximal Amplitude: 14.17 [mbar]

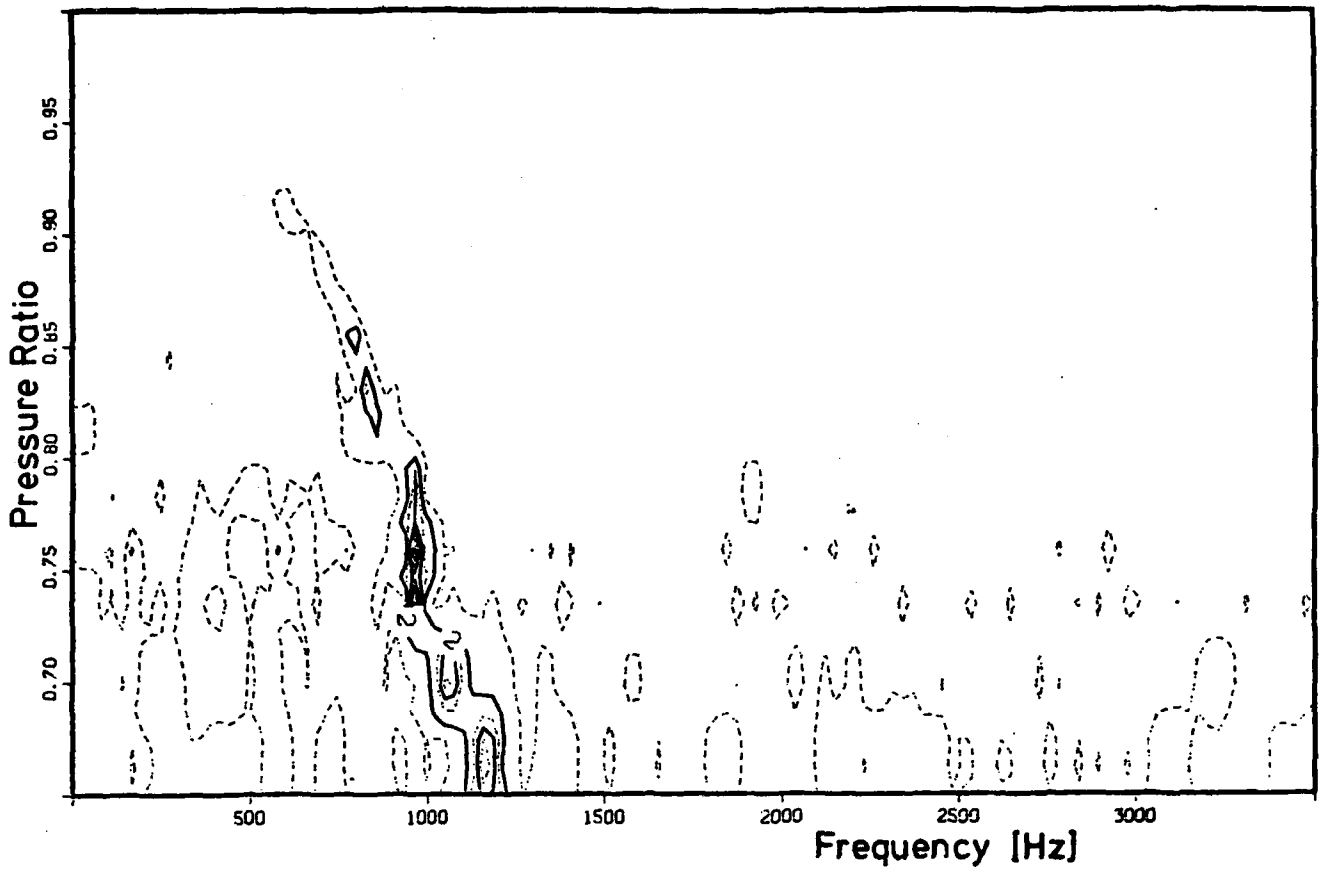

9b: Profile - Vortex Street Interaction
Transducer 5 Maximal Amplitude: 49.92 [mbar]

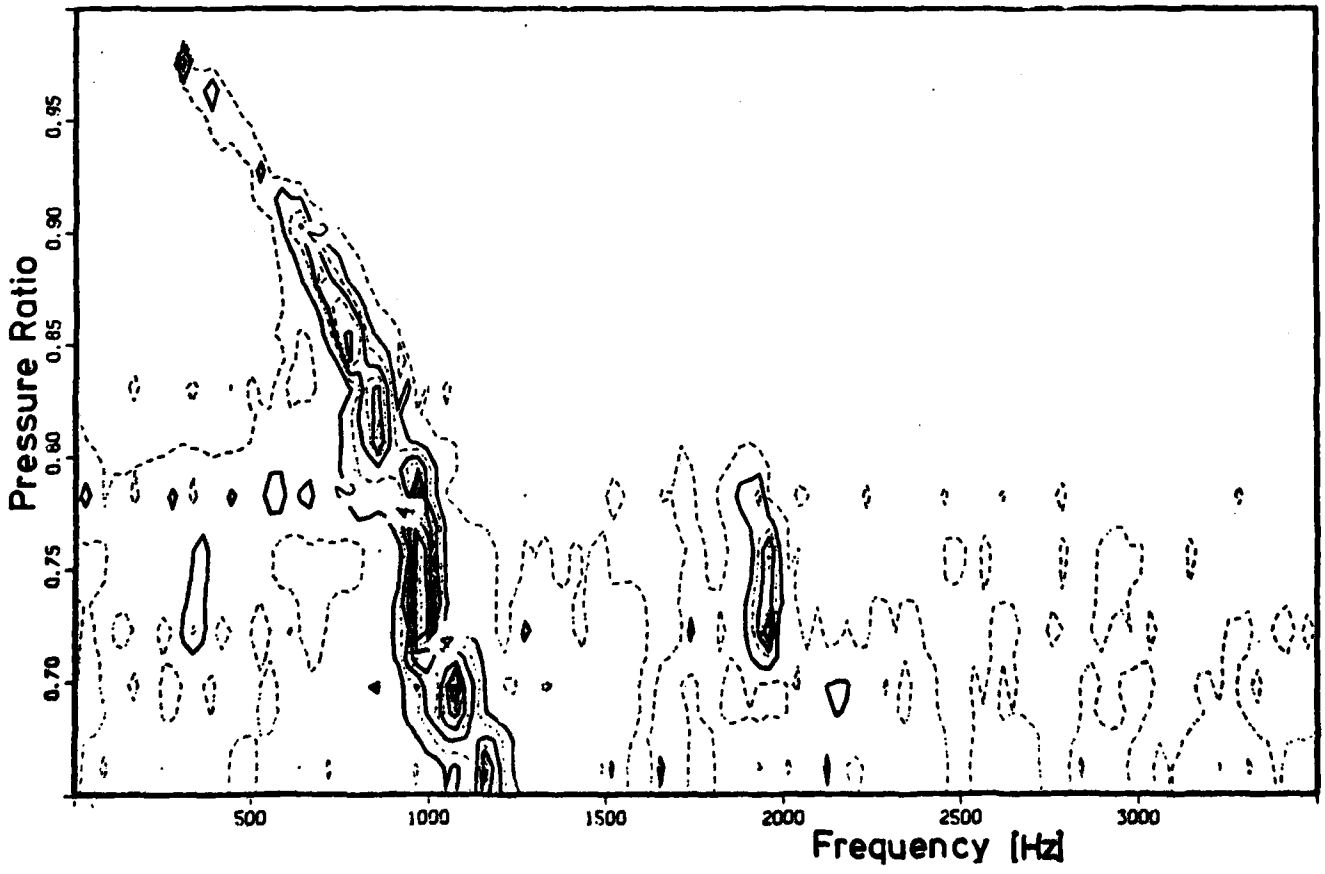

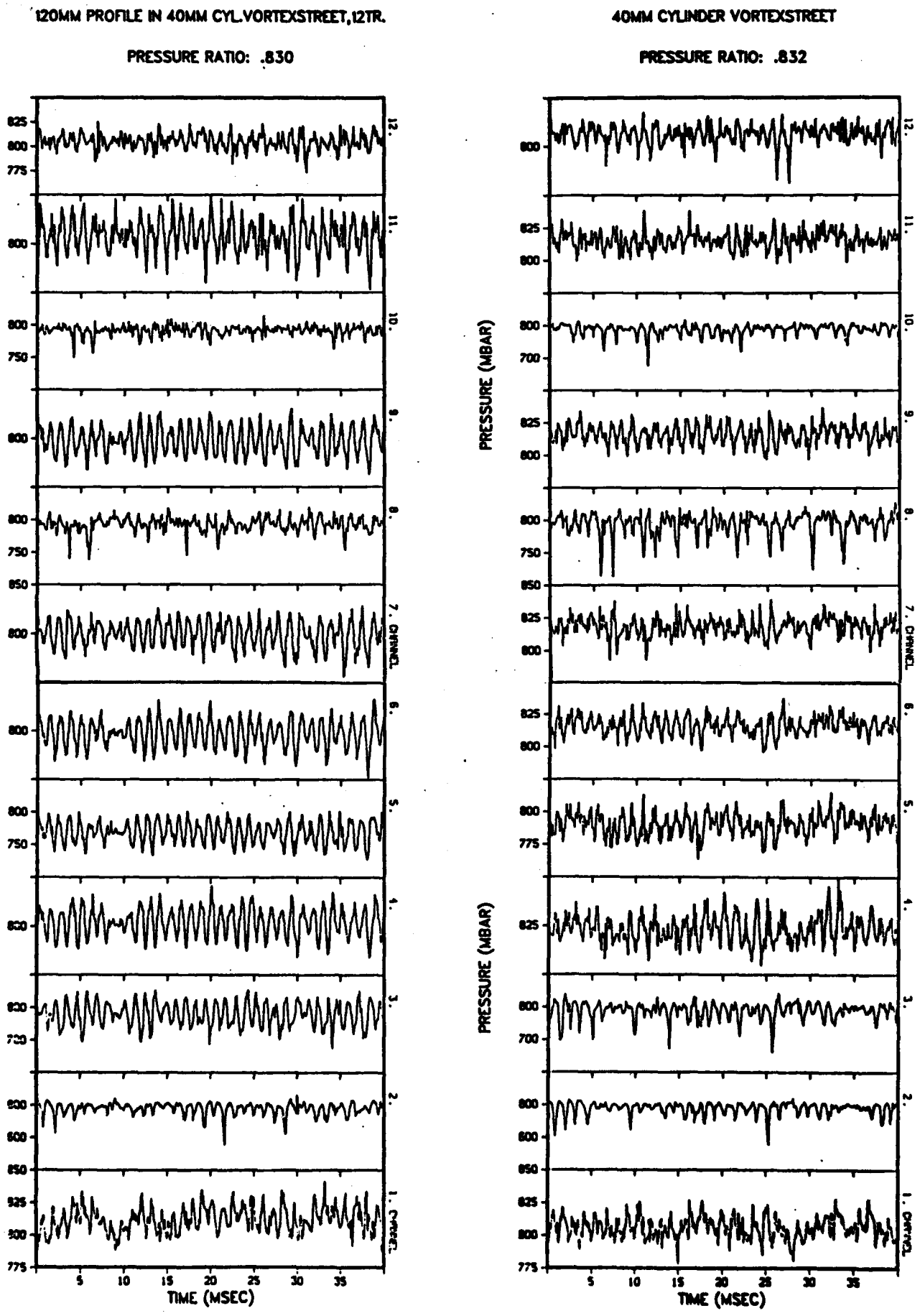

Figure 10a and 10b

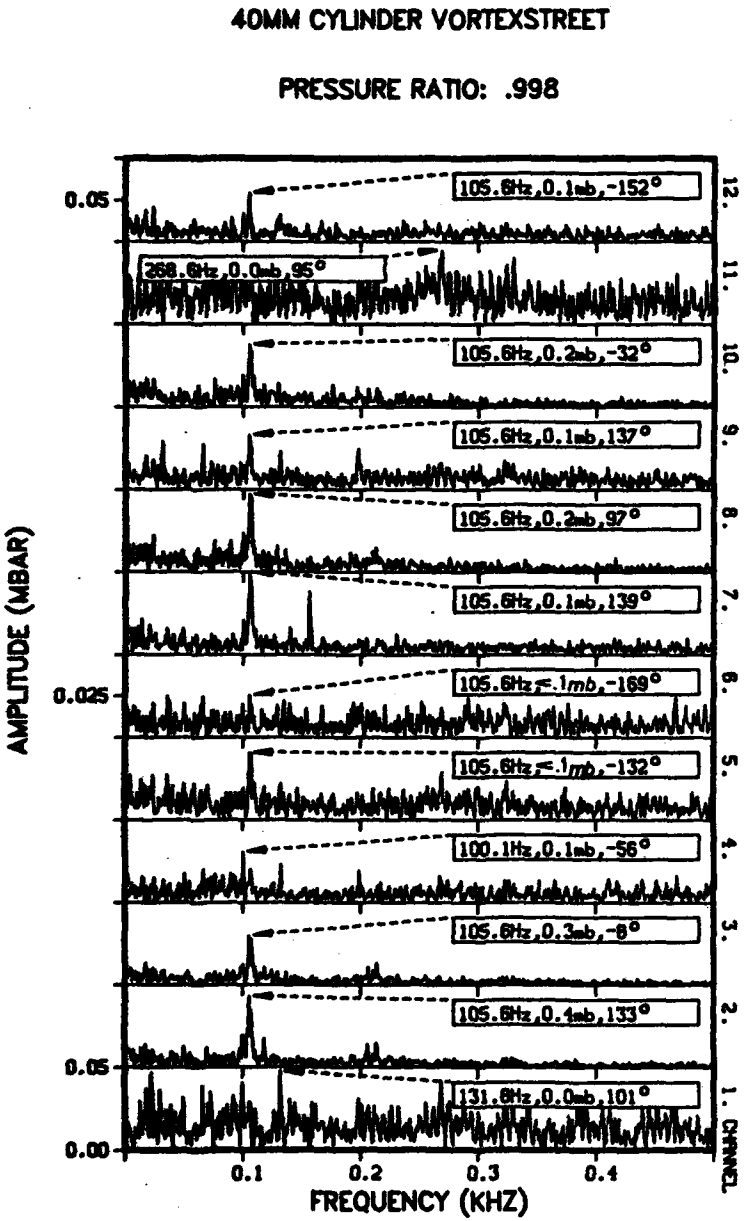

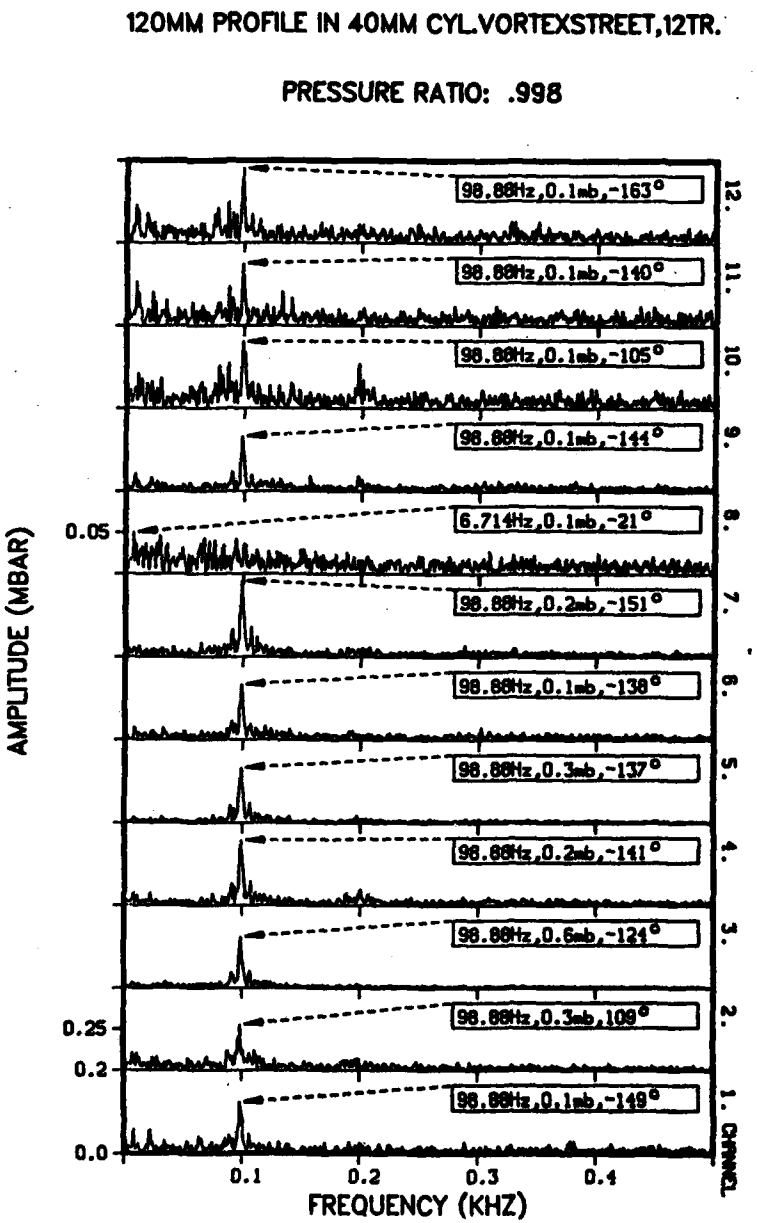

Figure 11a and 11b

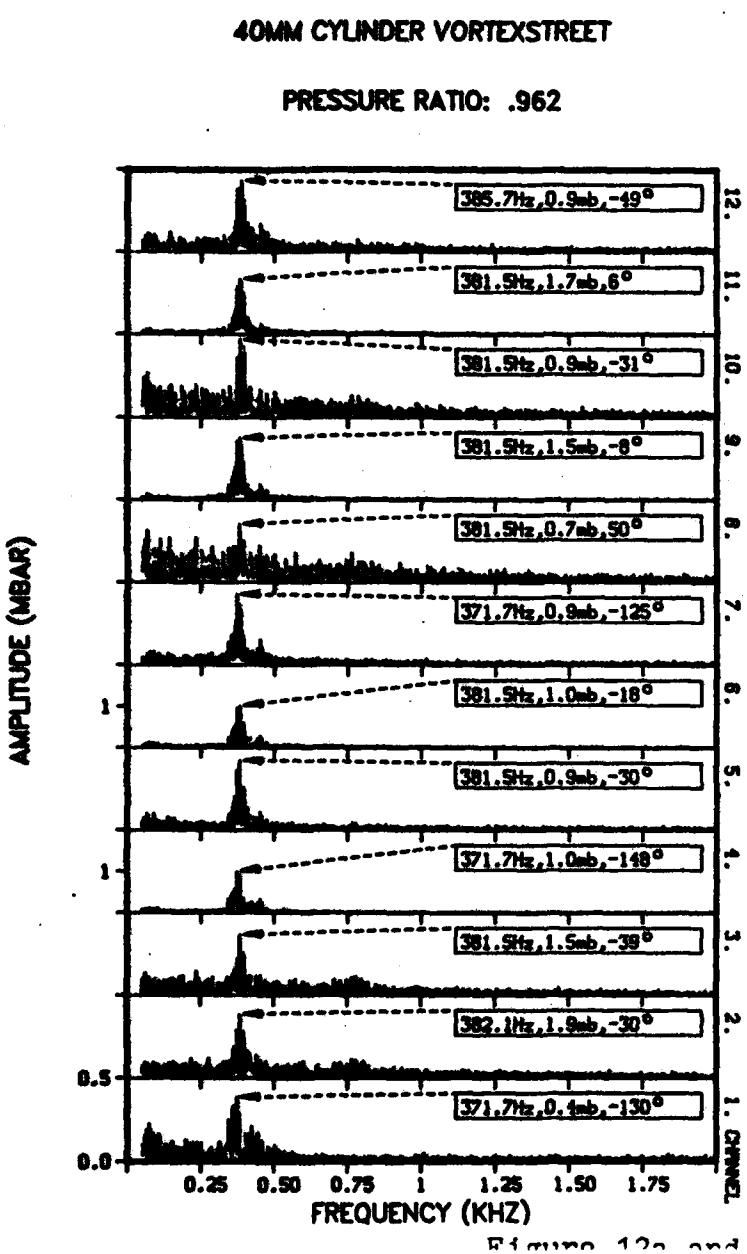

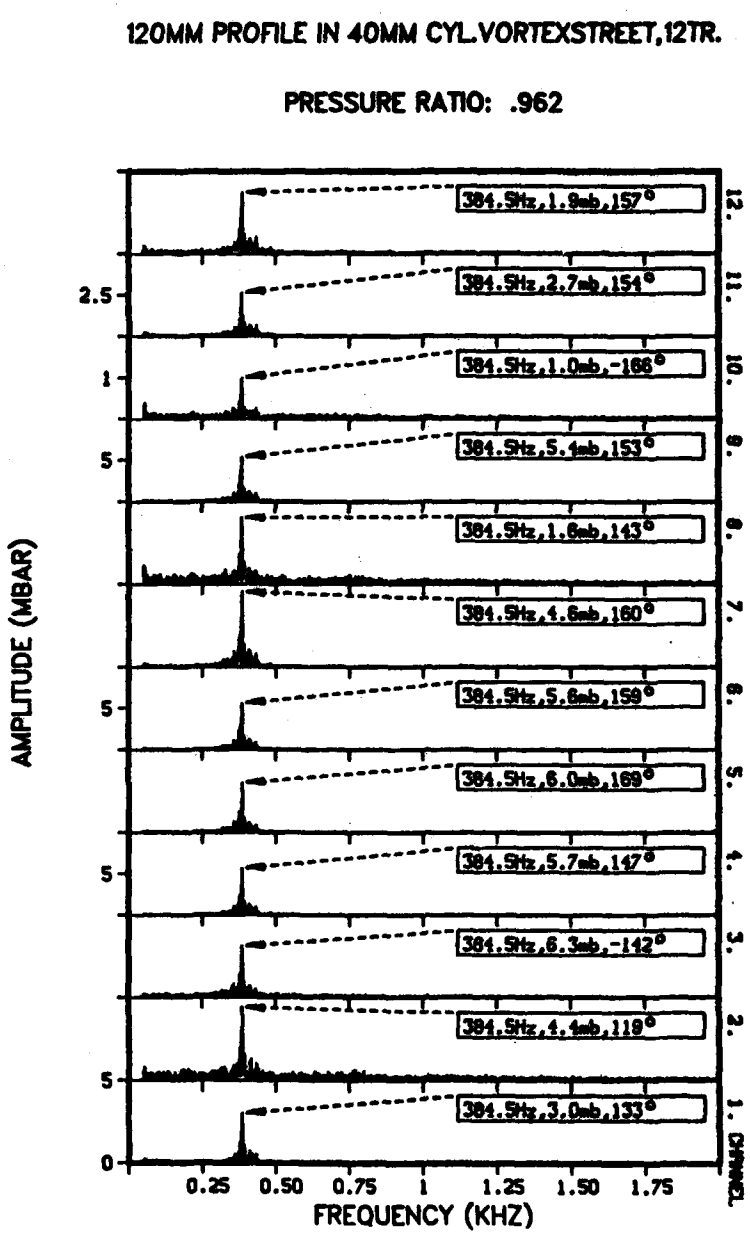

Figure 12a and 12b

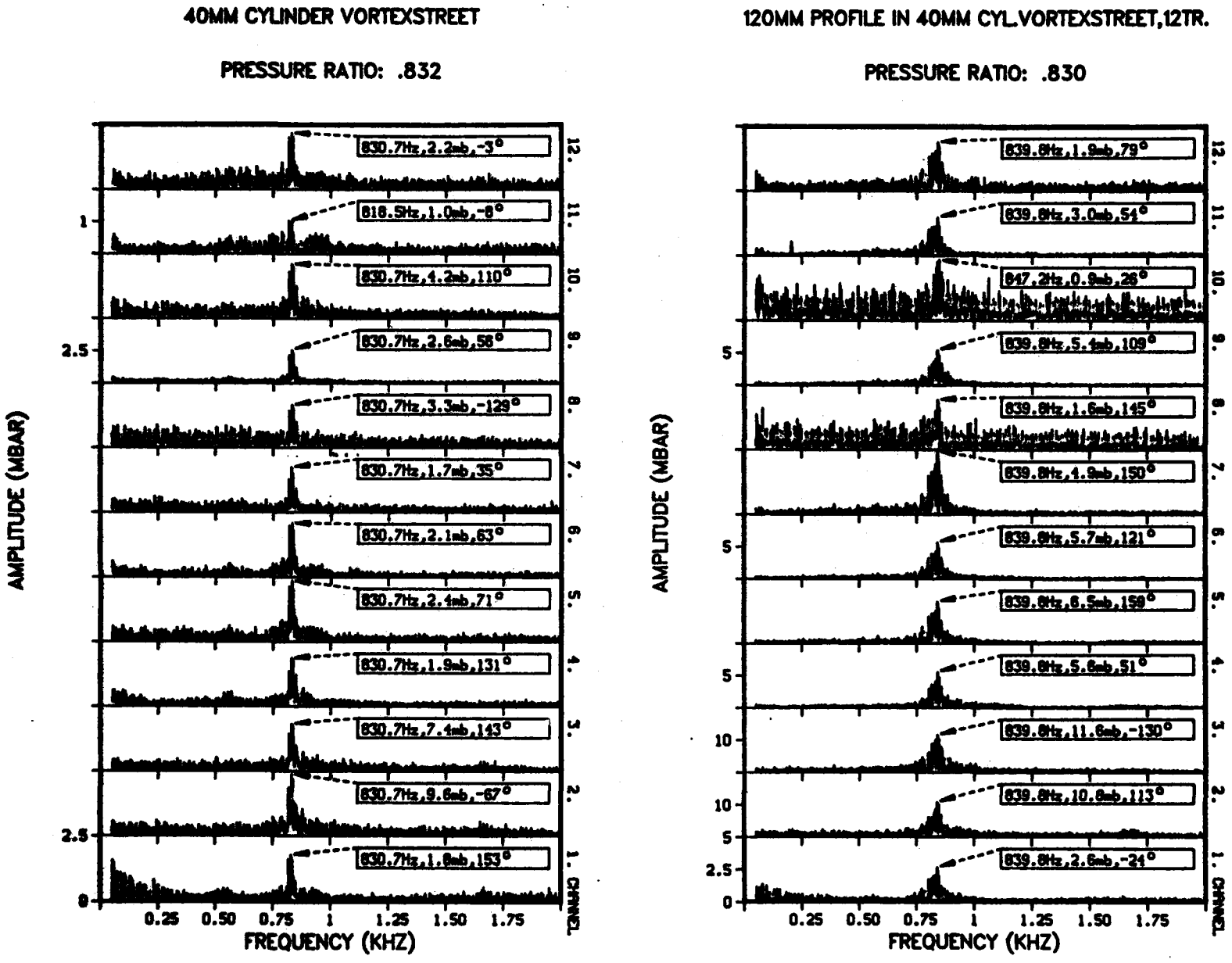

Figure 13a and 13b

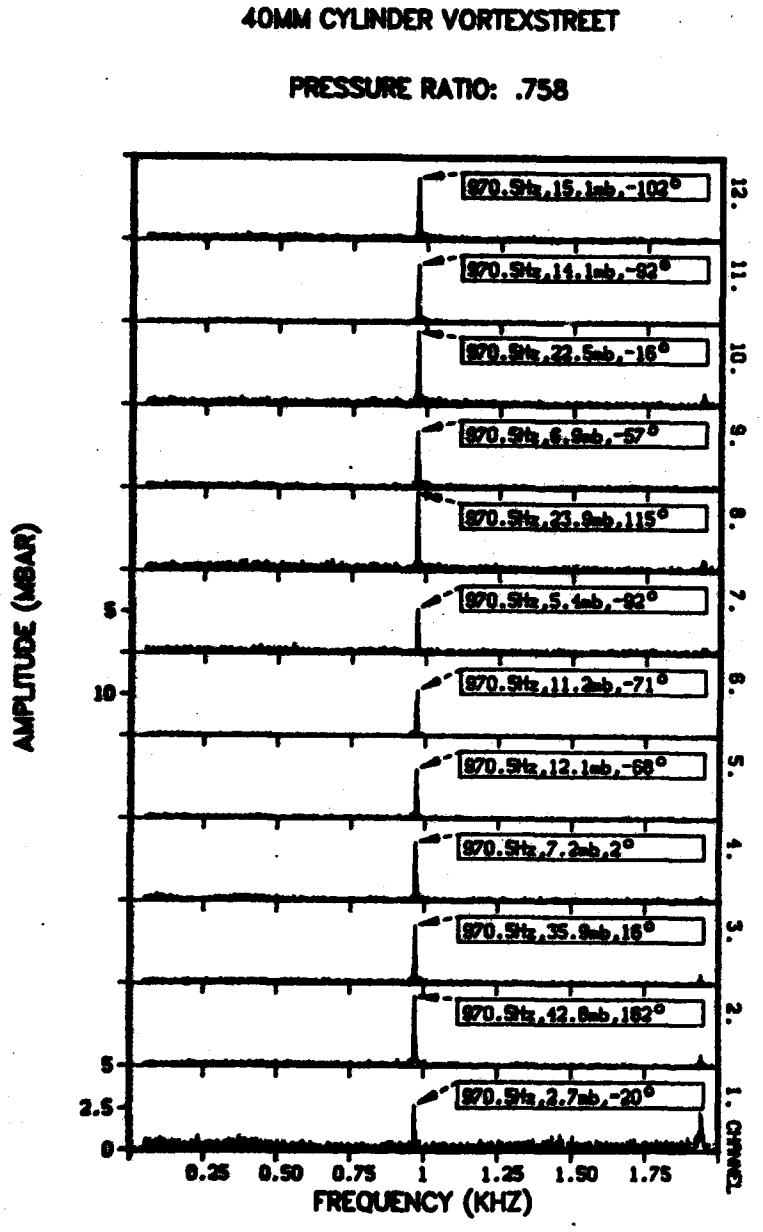

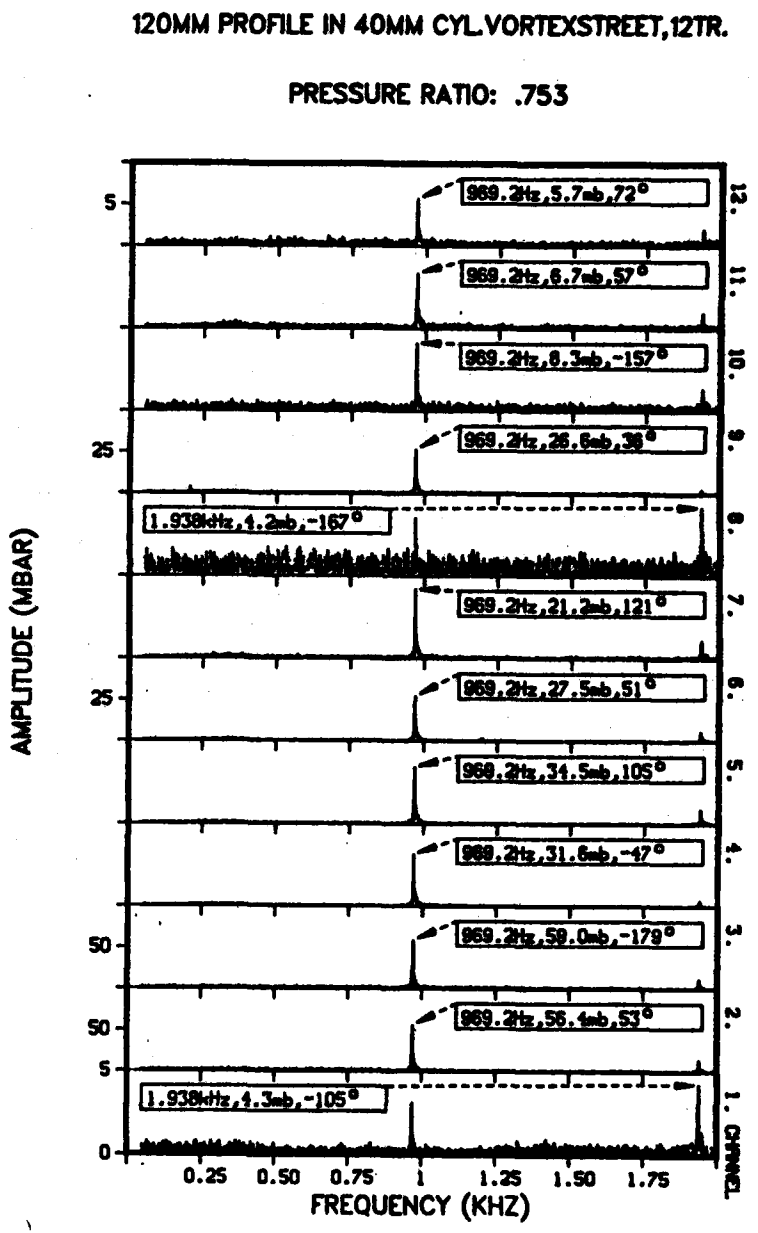

Figure 14a and 14b

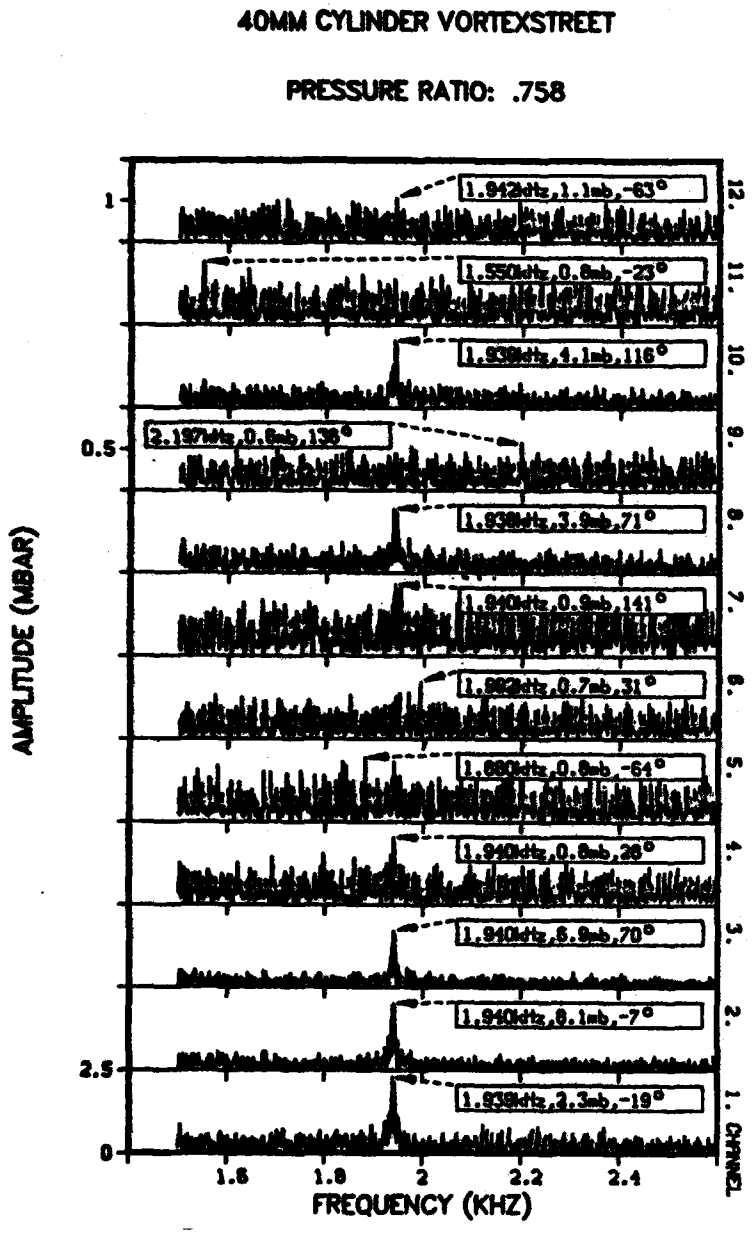

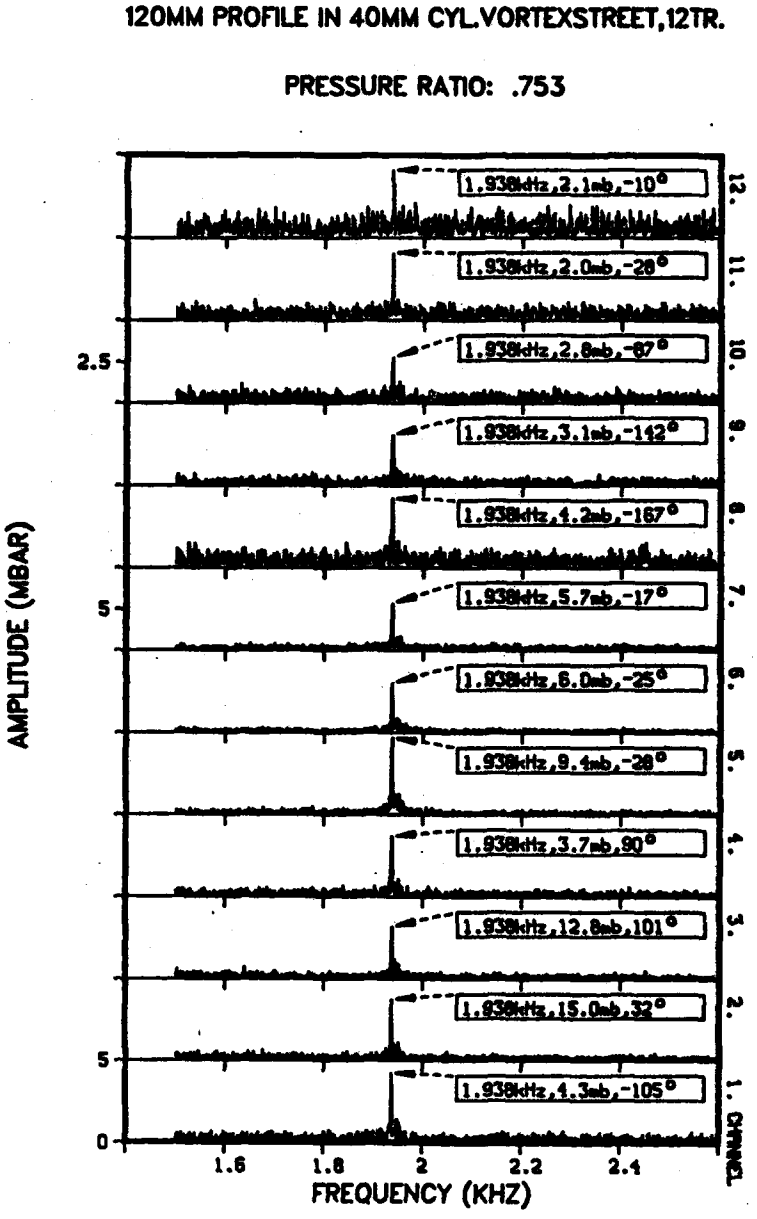

Figure 15a and 15b

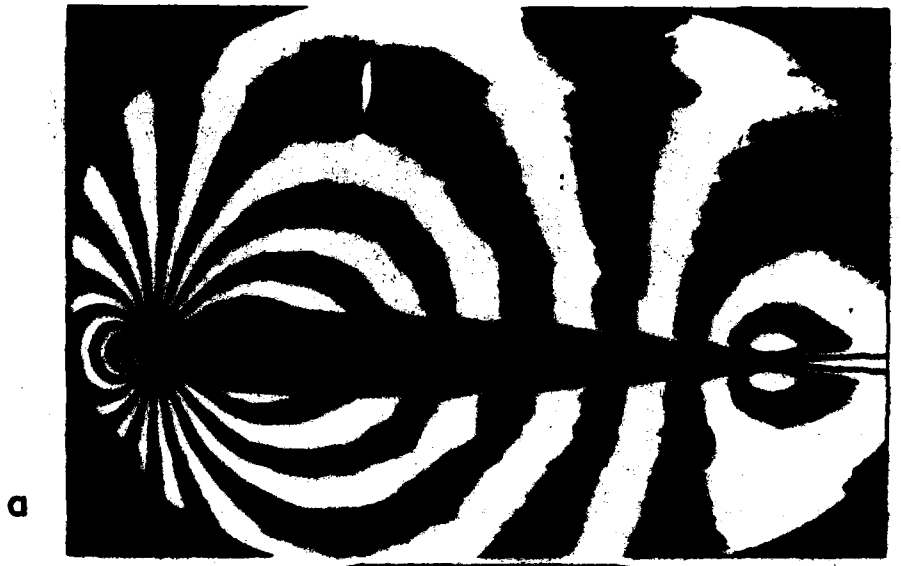

a

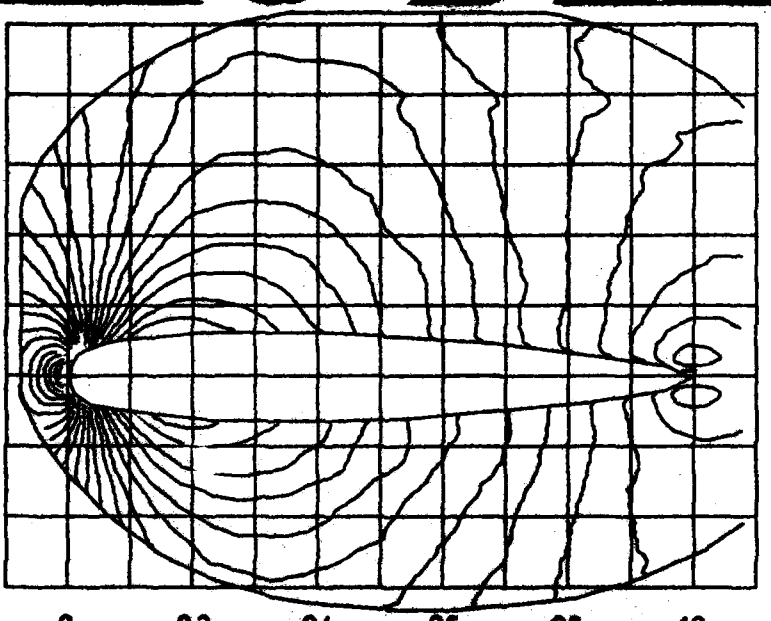

Figure 16: Example of evaluated interferograms
a) Photo of a profile flow interferogram
b) Plot of the segmented fringes of Fig. 17a after removal of the line disconnections. The mesh lines used for computing of the polynomial coefficients as well as the boundary lines of the testsection are included for illustration.
c) Density profiles plotted from the spline surface of the order number function of Fig. 17b along the x-direction at y=-0.2 The density is given in relative units (fringe numbers); high values represent low densities.

a

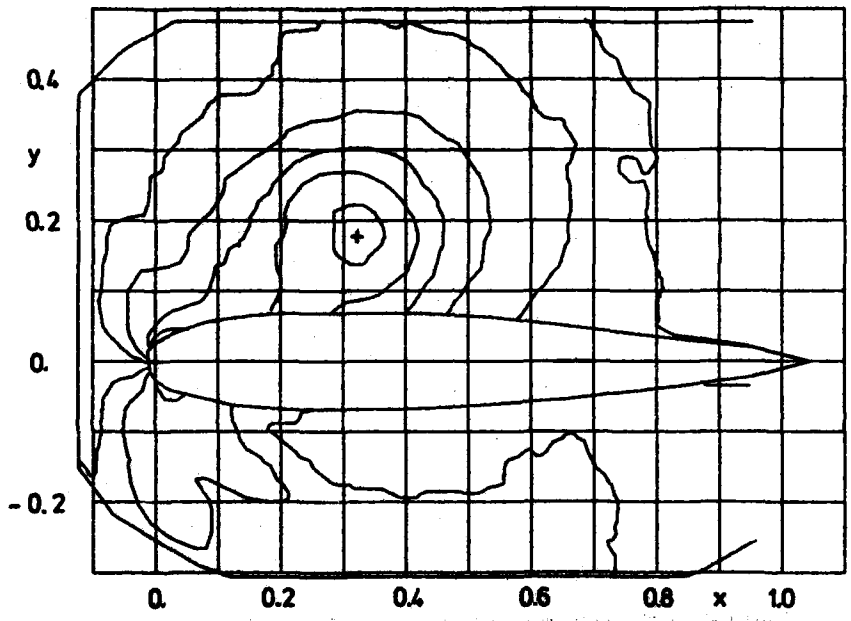

b

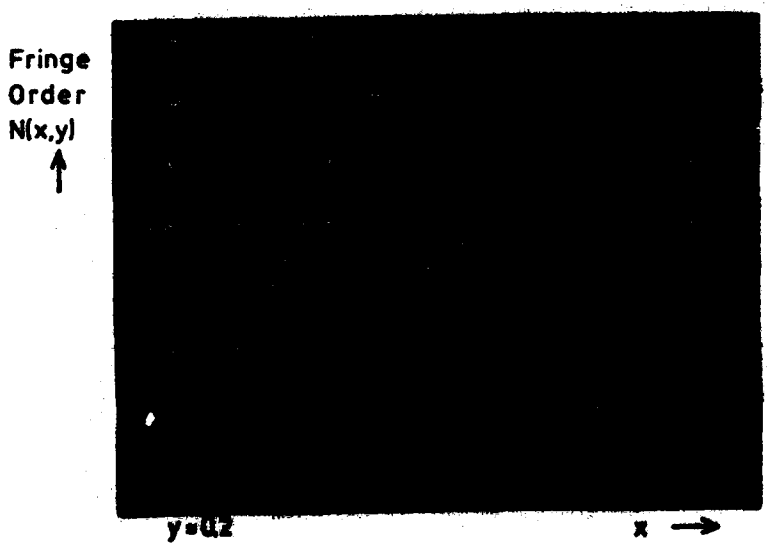

c

Figure 17: Example of evaluated interferograms
a) Photo of a profile flow interferogram with vortex
b) Plot of the segmented fringes of Fig. 18a after removal of the line disconnections. The position of the vortex core is at (x,y)=(0.32,0.18).
c) Density profiles plotted from the spline surface of the order number function of Fig. 18b along the x-direction at y=-0.2 The density is given in relative units (fringe numbers); high values represent low densities.

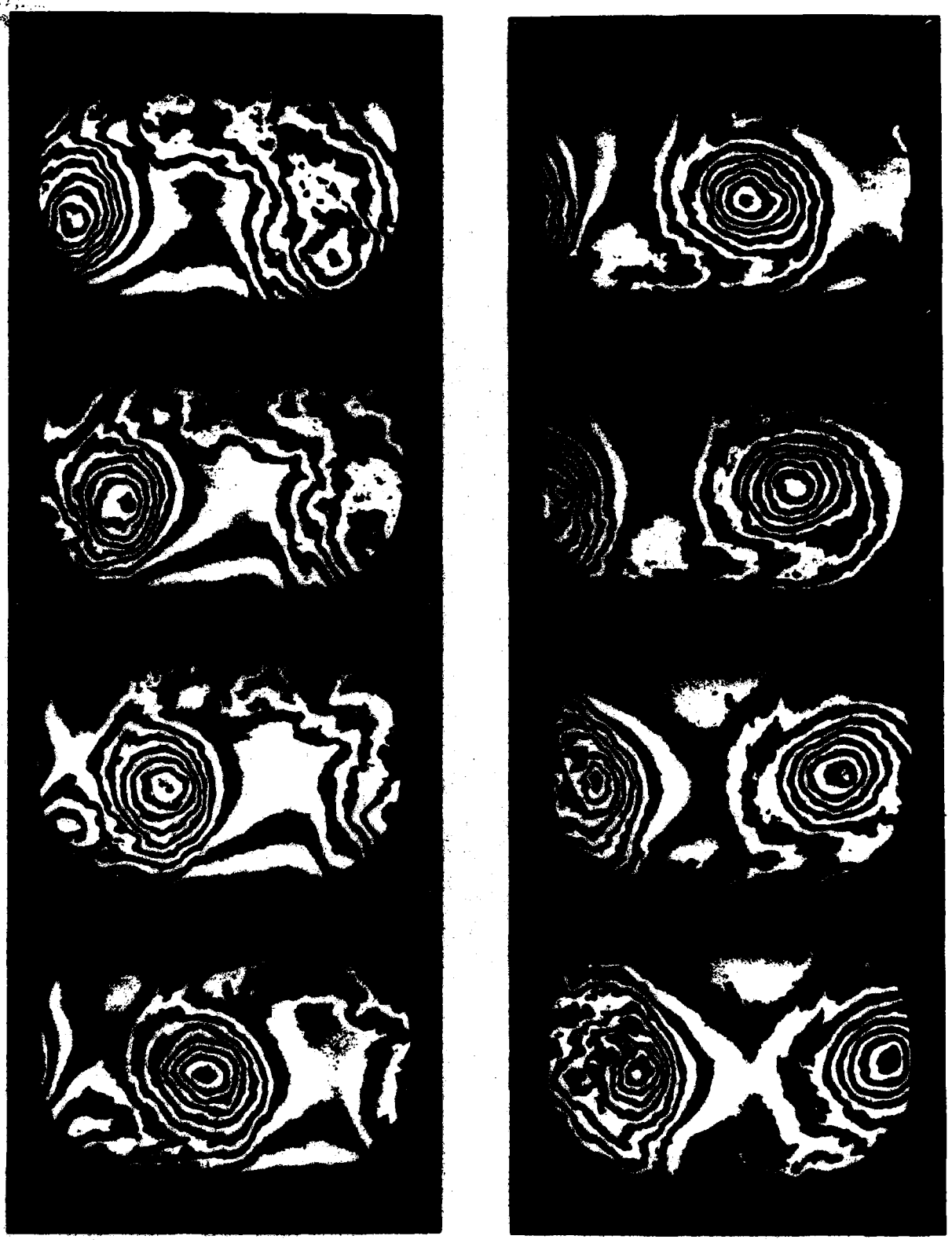

Figure 18a,b: Karman vortex street of a 40 mm square cylinder (see figure 5b).

$v_\infty = 170$ m/s , $v_{tr} = 120$ m/s , $\Gamma = 15$ m^2/s

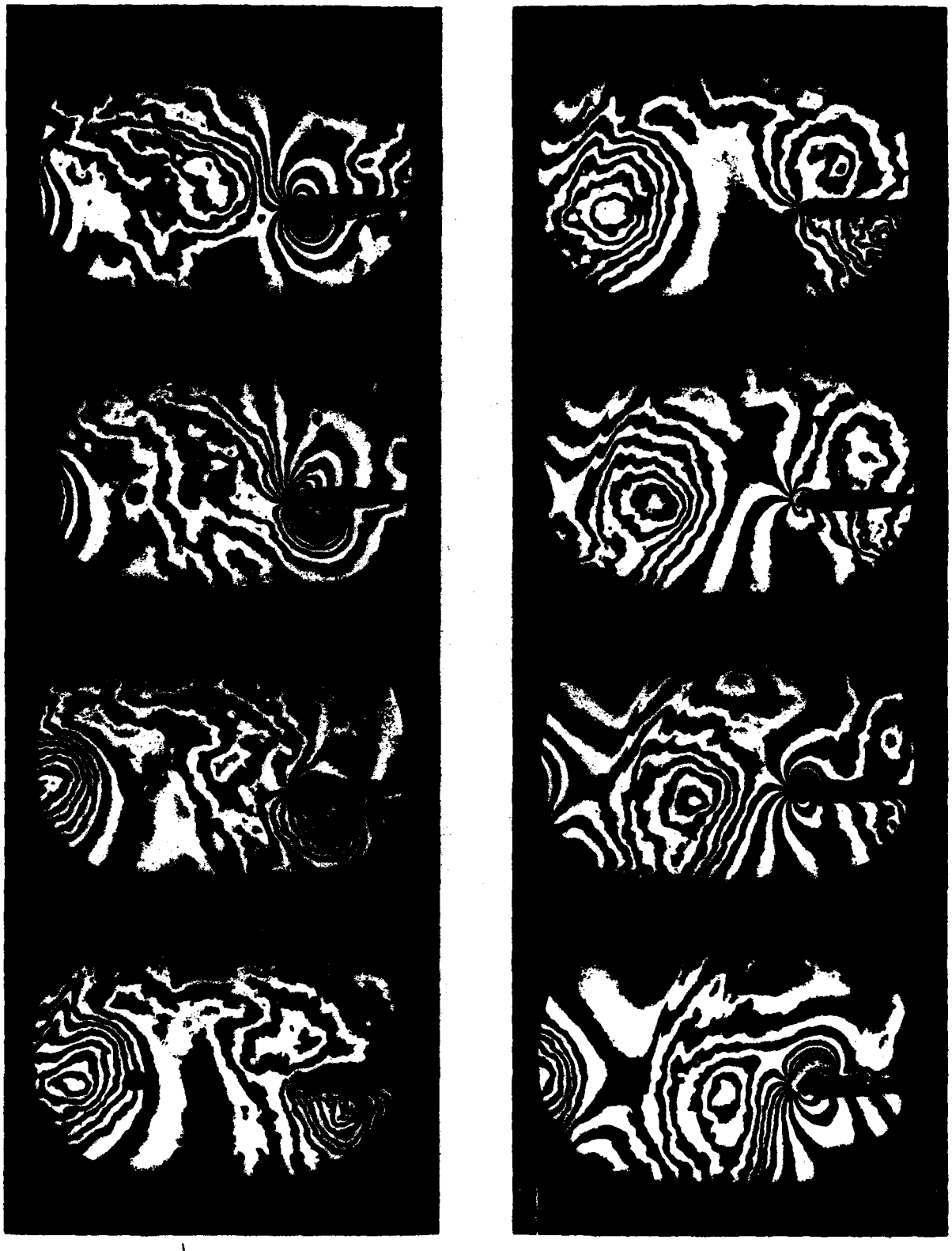

Figure 19a,b: 60 mm profile in the Karman vortex street of a 40 mm square cylinder (see figure 5b).

$v_\infty = 170$ m/s , $v_{tr} = 110$ m/s , $\Gamma_{dl} = 0.7$

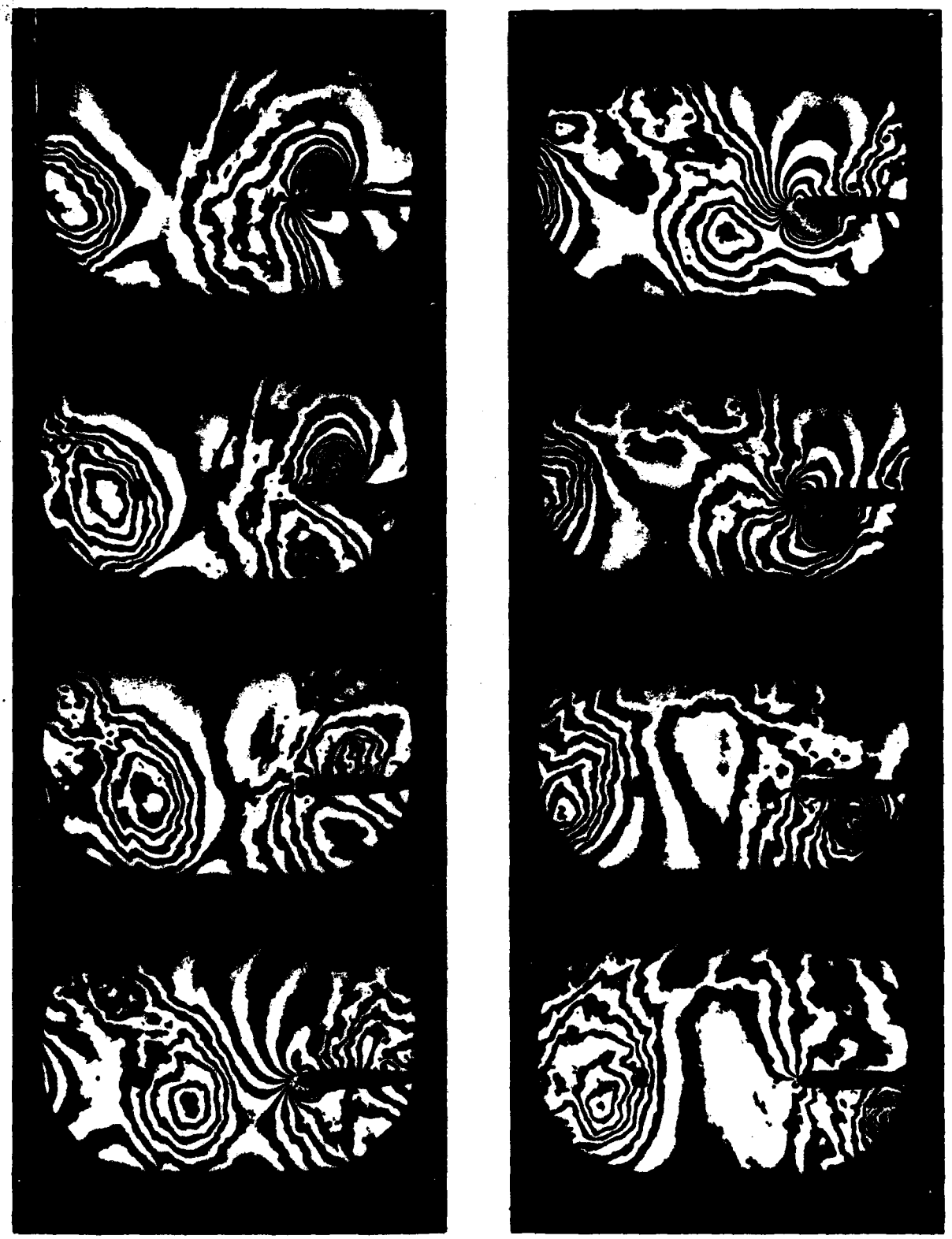

Figure 15a,d: 60 mm profile in the Karman vortex street of a 40 mm square cylinder (see figure 5b).

$V_{\infty} = 170$ m/s , $V_{tr} = 110$ m/s , $\Gamma_{dl} = 0.7$

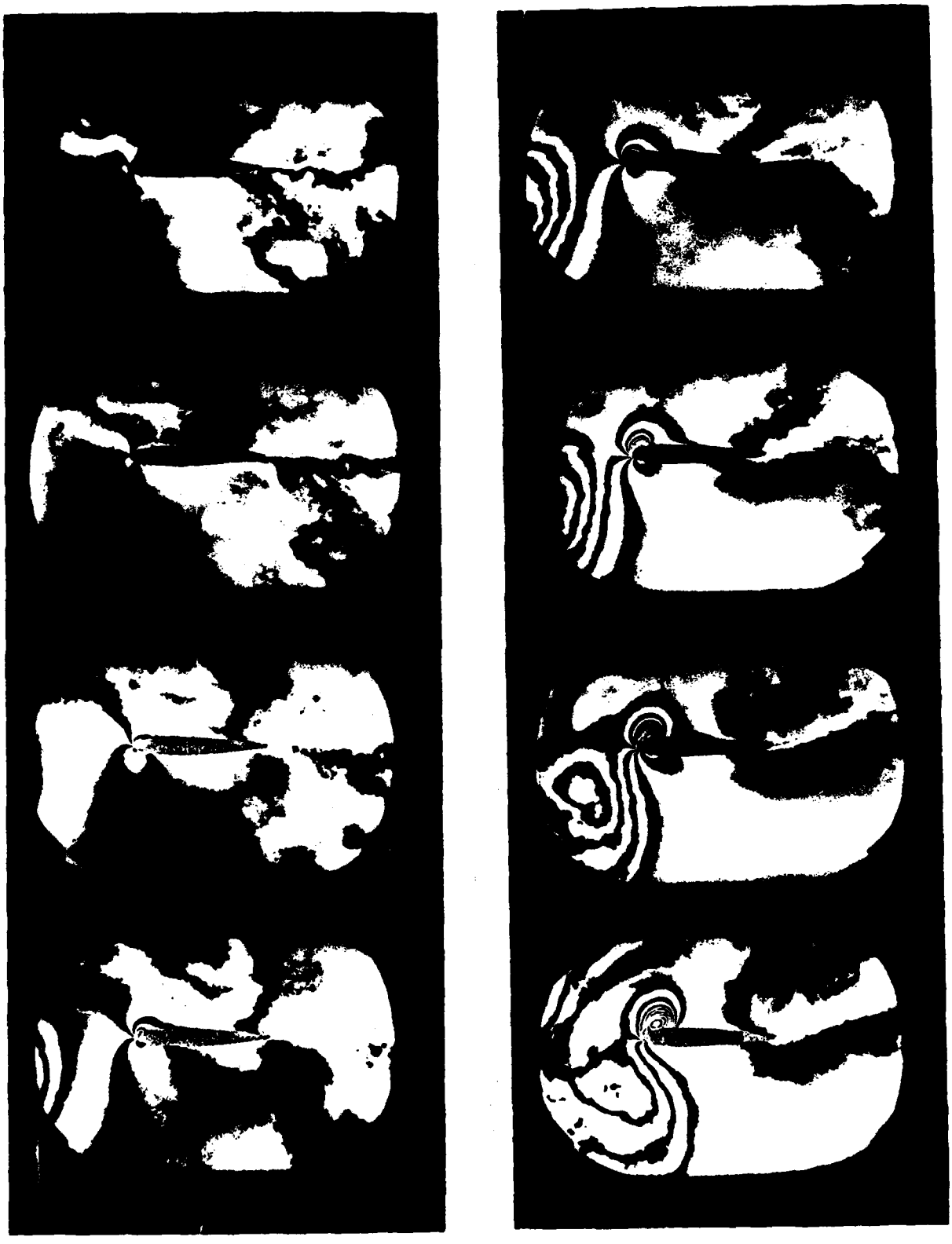

Figure 20a,b: 60 mm profile in the Karman vortex street of a 40 mm square cylinder (see figure 5c).

$v_\infty = 120$ m/s , $v_{tr} = 85$ m/s , $\Gamma_{dl} = 0.7$

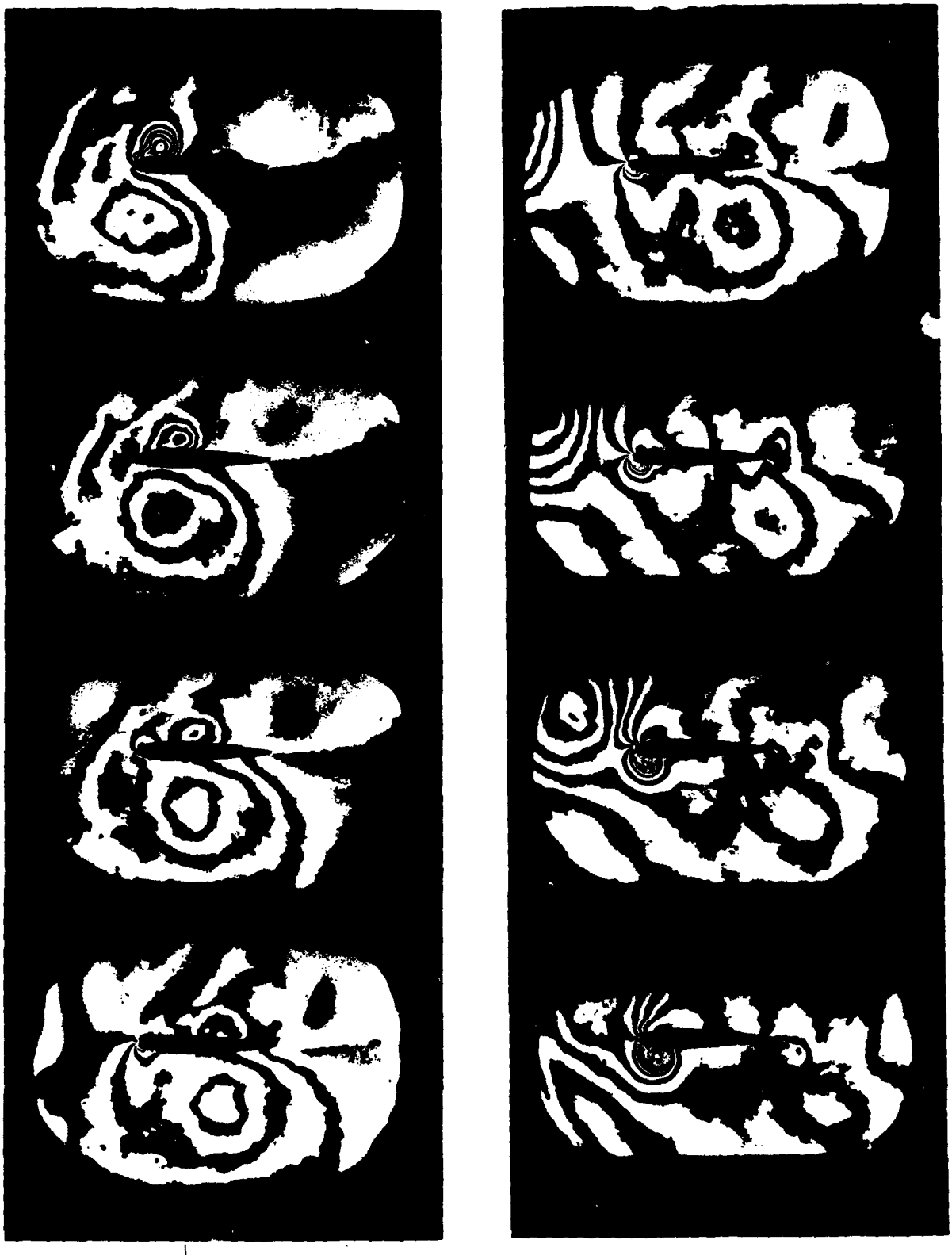

Figure 20c,d: 60 mm profile in the Karman vortex street of a 40 mm square cylinder (see figure5c).

$v_\infty = 120$ m/s , $v_{tr} = 85$ m/s , $\Gamma_{dl} = 0.7$

AD A157 163 TRANSONIC NOISE GENERATION BY DUCT AND PROFILE FLOW(U) 2/2
MAX-PLANCK-INST FUER STROEMUNGSFORSCHUNG GOETTINGEN
(GERMANY F R) G E MEIER OCT 84 DAJA37-81-C-0251

UNCLASSIFIED F/G 20/1 NL

END
DATE FILMED
9 85

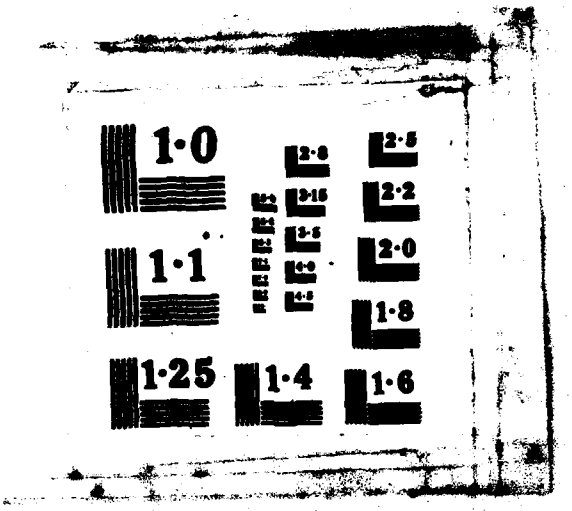
1·0
1·1
1·25
1·4
1·6
1·8
2·0
2·2
2·5

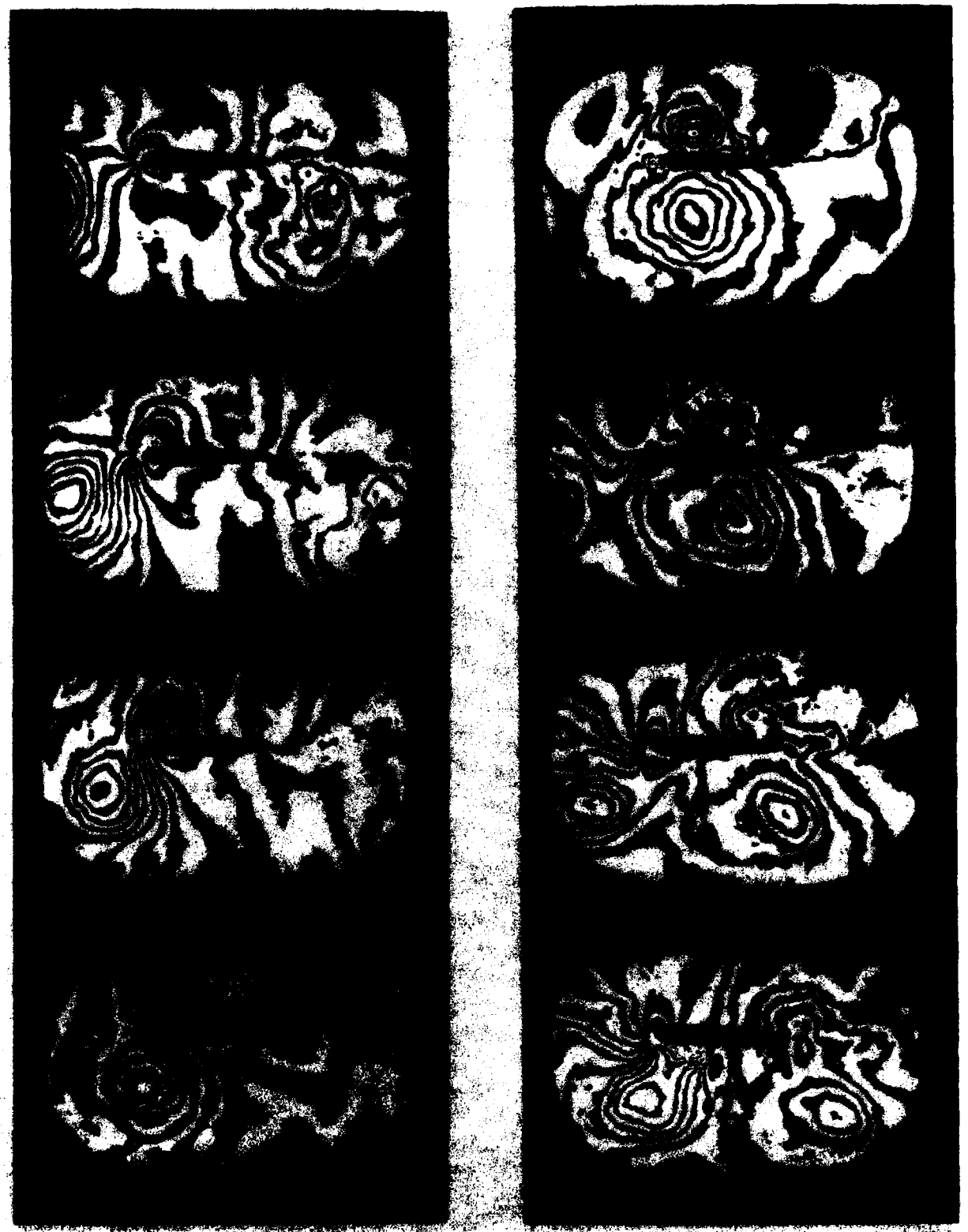

Figure 21a,b: 60 mm profile in the Karman vortex street of a 40 mm square cylinder (see figure 5c).

v_∞ = 170 m/s , v_{tr} = 115 m/s , Γ_{dl} = 0.7

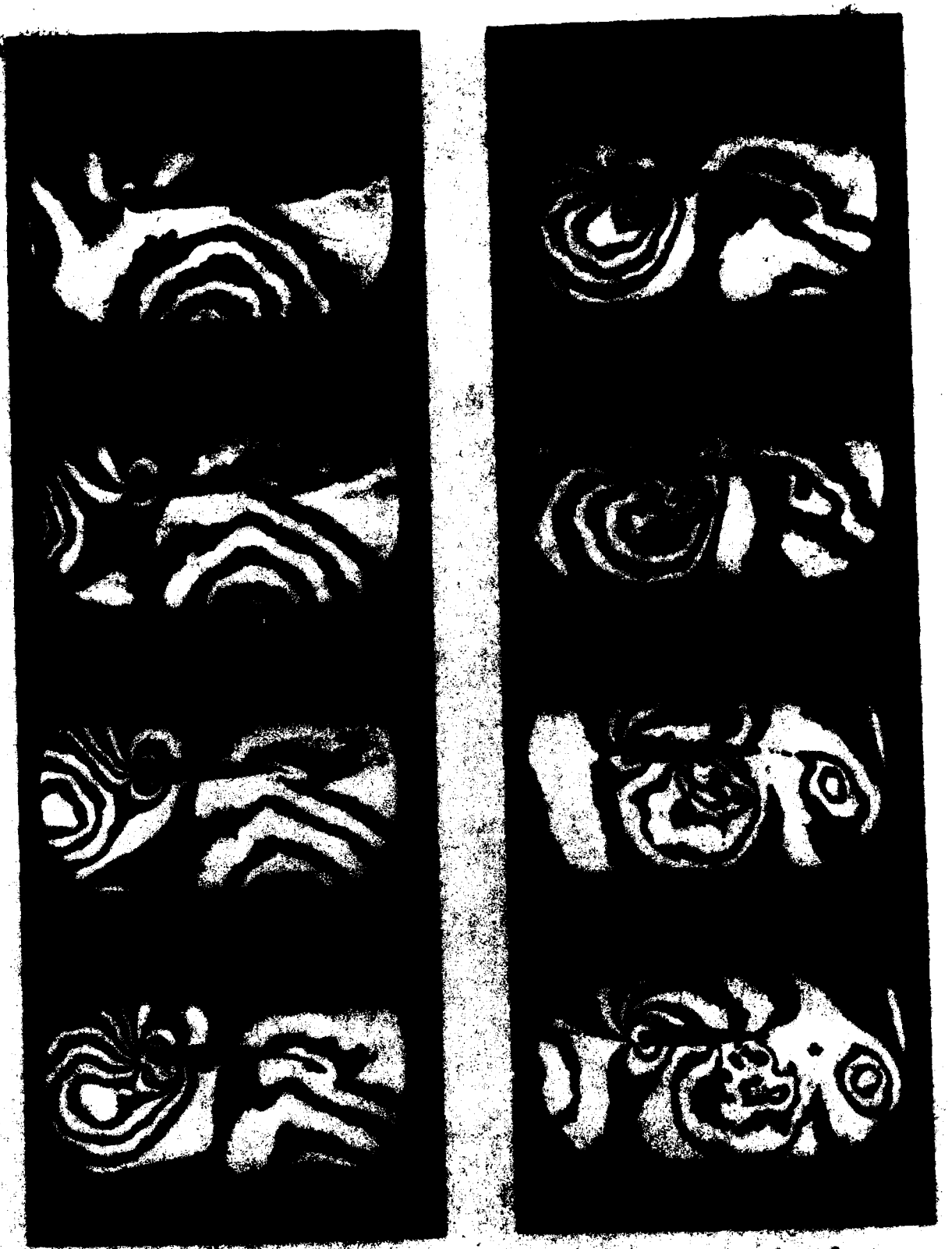

Figure 22a,b: 60 mm profile in the Karman vortex street of a 40 mm square cylinder (see figure 5c).

$v_\infty = 120\,m/s$, $v_w = 8.0\,m/s$, $\Gamma_{dl} = 0.7$

Figure 22a,d| 60 mm profile in the Karman vortex street of a 40 mm square cylinder (see Figure 5c).

$v_\infty = 120$ m/s , $v_{tr} = 60$ m/s , $\Gamma_{dl} = 0.7$

Figure 23a,b/ 60 mm profile in the Karman vortex street of a 20 mm square cylinder (see figure 5d).

V_∞ = 210 m/s , V_{fr} = 110 m/s , Γ_{ct} = 0.4

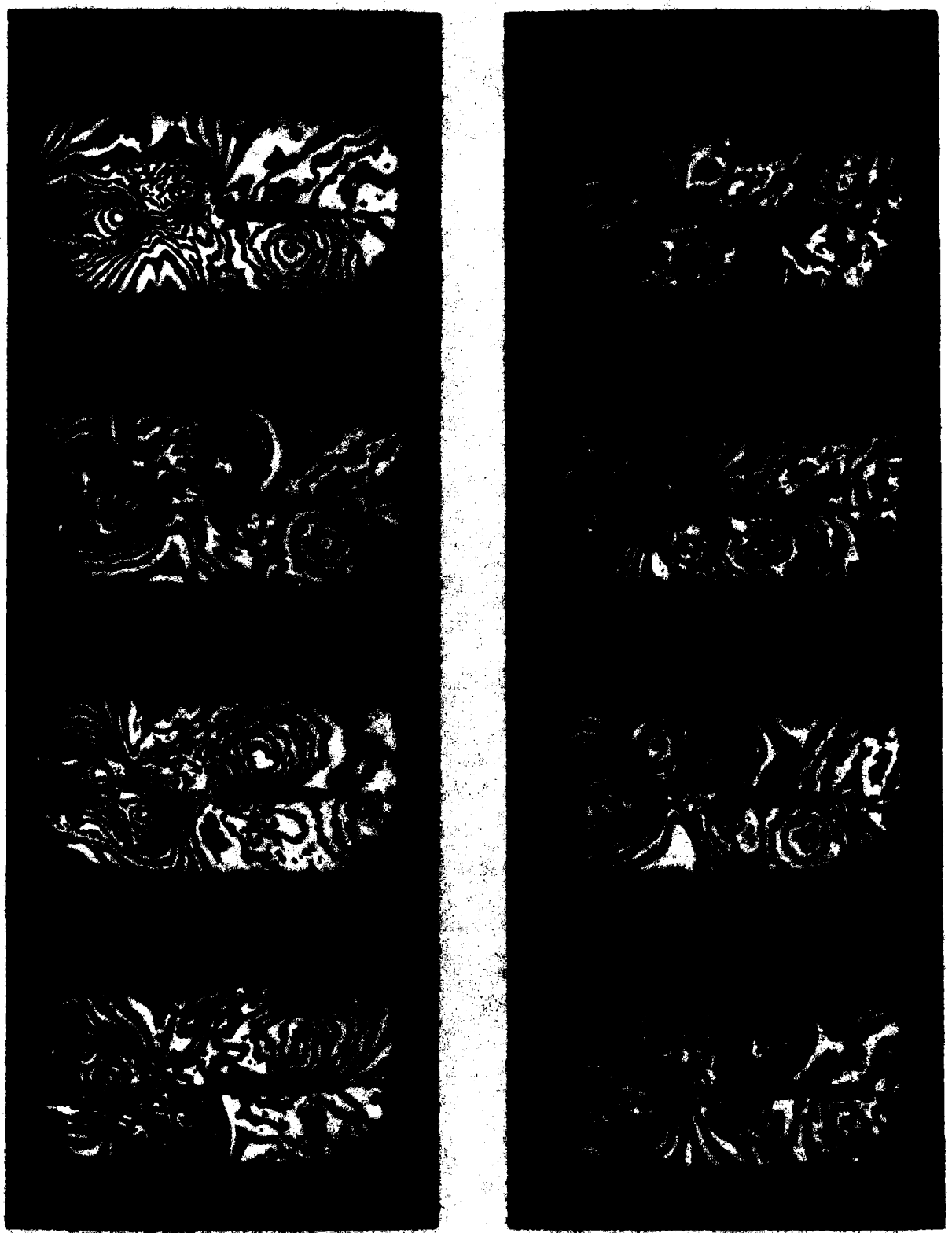

Figure 23a,d: 60 mm profile in the Karman vortex street of a 20 mm square cylinder (see figure 5d).

$v_\infty = 210\,m/s$, $v_{tr} = 110\,m/s$, $\Gamma_{d1} = 0.4$

Figure 24a,b: 120 mm profile in the Kármán vortex street of a 20 mm square cylinder (see figure 5a).

$v_\infty = 170$ m/s , $v_{tr} = 120$ m/s , $\Gamma_{dl} = 0.15$

Figure 24c,d: 120 mm profile in the Karman vortex street of a 20 mm square cylinder (see figure 5a).

$v_\infty = 170$ m/s , $v_{tr} = 120$ m/s , $\Gamma_{dl} = 0.15$

Figure 25a,b: Shock tube starting vortex at Machnumber M= 0.2

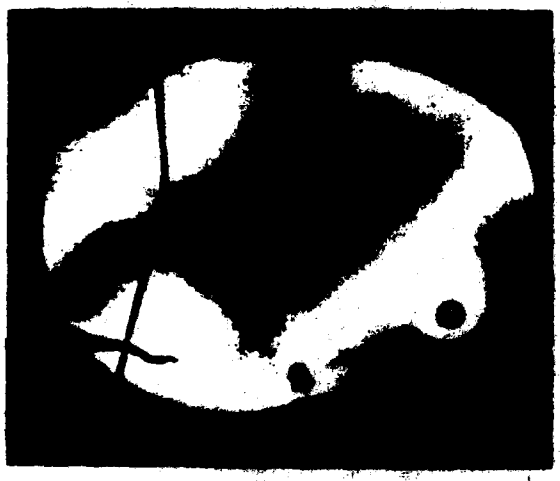

Figure 26: Shock tube starting vortex at Machnumber M= 0.2.

Figure 27a: Vortex-profile interaction at Machnumber M= 0.2: Vortex generation.

$v = 70\ m/s\ ,\ \Gamma_{dl} = 0.12$

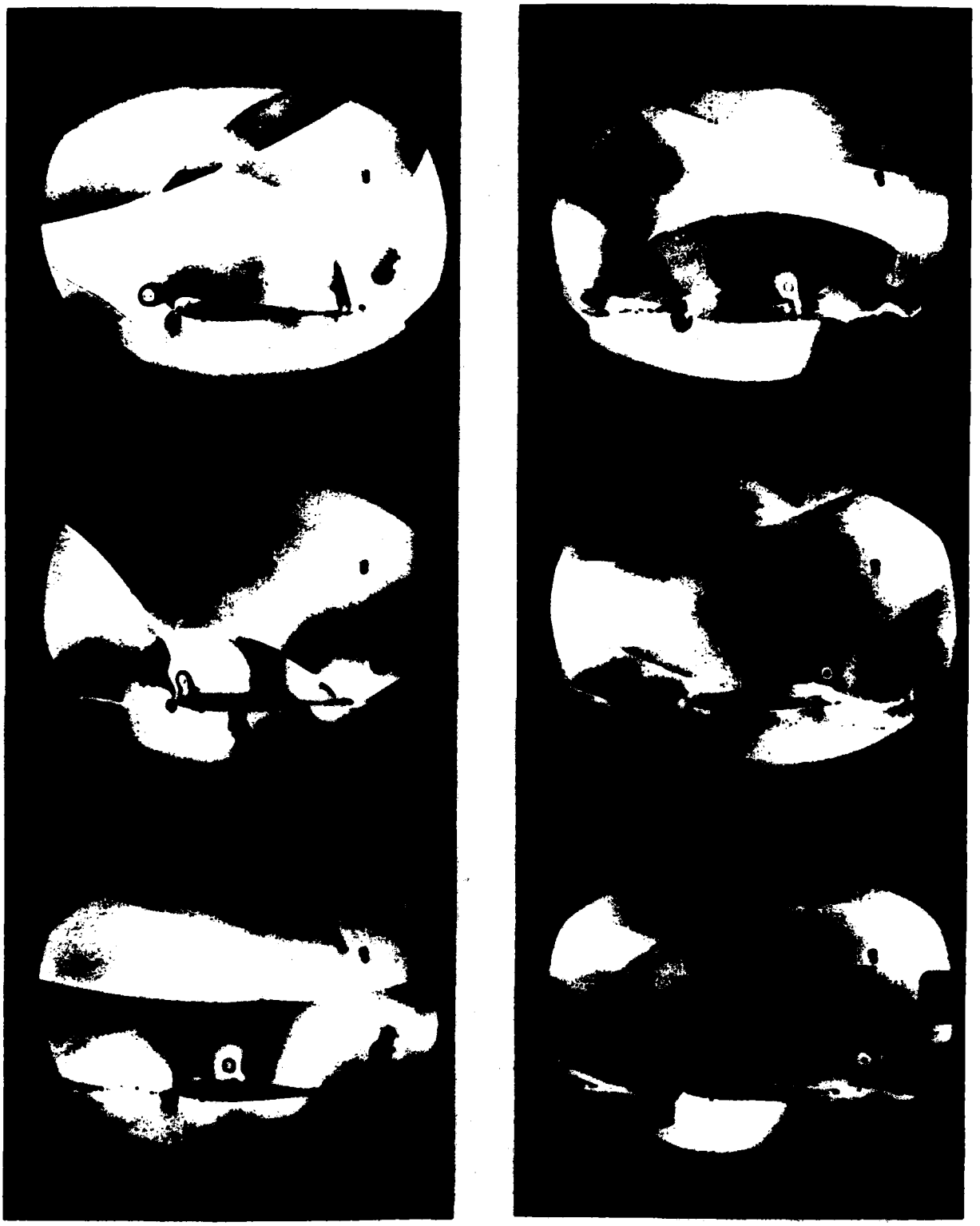

Figure 27b,c: Shock tube vortex-profile interaction at Machnumber M= 0.2.

$v = 70\ m/s\ ,\ \Gamma_{d1} = 0.12$

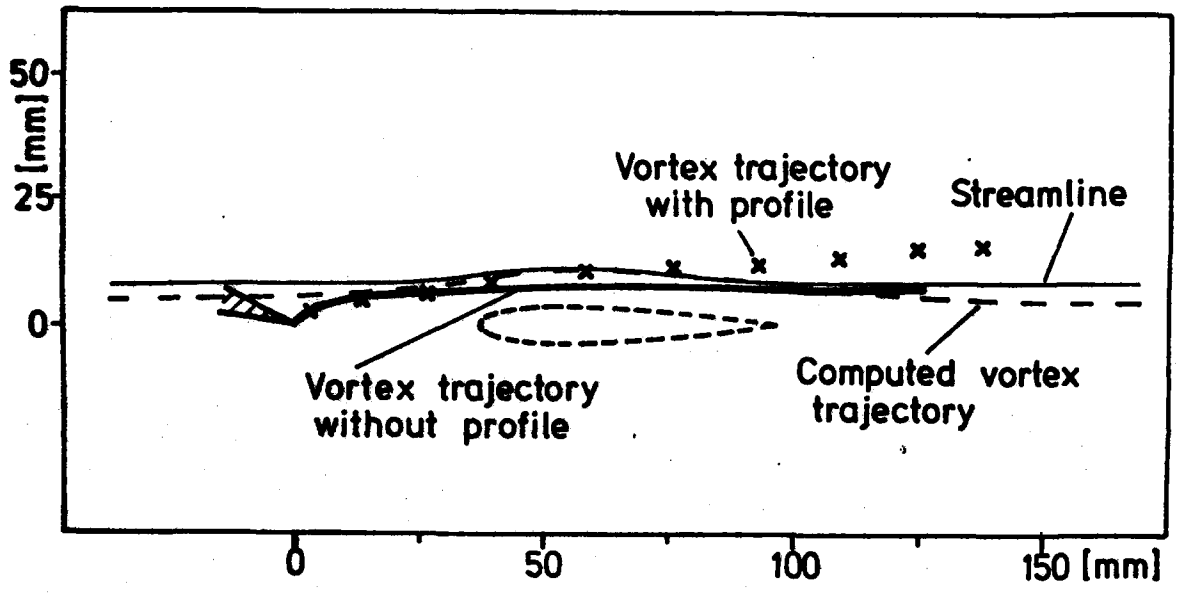

Figure 28: Vortex trajectories

X: Measured vortex trajectory

black line: Free vortex trajectory

dashed line: Computed vortex trajectory

thin line: Computed streamline

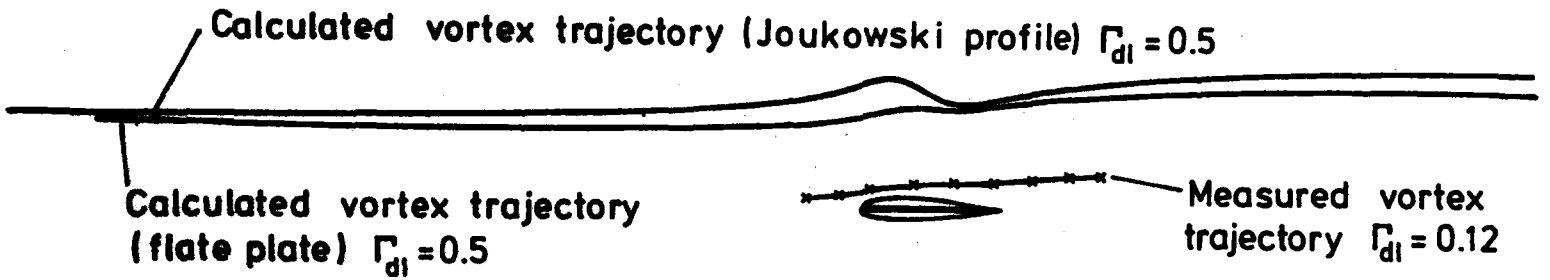

Figure 29: Calculated and measured vortex trajectories.
Calculations by Parthasarathy [14].